UNIVERSITAT DE BARCELONA

# Biomechanics of the progression of colorectal carcinomas

Giulia Fornabaio

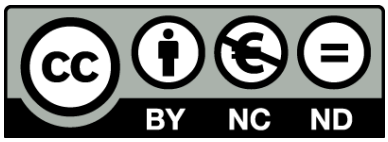

Tesi Doctoral

# Biomechanics of the progression of colorectal carcinomas

Giulia Fornabaio

UNIVERSITAT DE BARCELONA

# Biomechanics of the progression of colorectal carcinomas

Programa de doctorat en Biomedicina

Universitat de Barcelona

Autor: **Giulia Fornabaio**

Directors: **Vito Conte, Jordi Comelles Pujadas**

Tutor: **Josep Samitier Martí**

Institut de Bioenginyeria de Catalunya (IBEC)

UNIVERSITAT DE BARCELONA

## Abbreviations

| | |
|---|---|
| 2D | Two Dimensional |
| 3D | Three Dimensional |
| AFM | Atomic Force Microscope |
| ANOVA | Analysis of Variance |
| APC | Adenomatous Polyposis Coli |
| APS | Ammonium Persulfate |
| BSA | Bovine Serum Albumin |
| Caco-2 | Colon Carcinoma cell line |
| CAF | Cancer Associated Fibroblast |
| CIMP | CpG island methylator phenotype |
| CRC | Colorectal Carcinoma |
| DAPI | 4’,6-diamidino-2-phenylindole |
| DMSO | Dimethyl sulfoxide |
| E-cadherin | Epithelial cadherin |
| ECM | Extracellular Matrix |
| EMT | Epithelial to-Mesenchymal Transition |
| ERK | Extracellular Signal-Regulated Kinase |
| F-Actin | Filamentous Actin |
| FAK | Focal Adhesion Kinase |
| Fbw7 | F-Box/WD Repeat-Containing protein 7 |
| FBS | Fetal Bovine Serum |

| | |
|---|---|
| G12D | Glycine 12 to Aspartate |
| GFP | Green Fluorescence Protein |
| GTP | Guanosine triphosphate |
| HDMEC | Human Dermal Microvascular Endothelial Cells |
| HEK-293T | Human Embryonic Kidney-293-T-antigen |
| HEPES | High Purity 4-(2-Hydroxyethyl)Piperazine-1-Ethanesulfonic Acid |
| HRAS | Harvey Rat Sarcoma virus |
| HUVEC | Human Umbilical Vein Endothelial Cells |
| I.e. | *Id est* (that is) |
| ITBCC | International Tumour Budding Consensus Conference |
| KRAS | Kirsten Rat Sarcoma virus |
| MAPK | Mitogen-Activated Protein Kinase |
| MCF-7 | Michigan Cancer Foundation-7 |
| MCF-10A | Michigan Cancer Foundation-10A |
| MDA-MB231 | M.D.Anderson - Metastatic Breast231 |
| MDCK | Madin-Darby Canine Kidney cell line |
| MSI | Microsatellite Instability |
| MSS | Microsatellite Stability |
| NRAS | Neuroblastoma Rat Sarcoma virus |
| p53 | Transformation-related Protein 53 |
| PAA | Polyacrylamide |
| PBS | Phosphate Buffered Saline |

| | |
|---|---|
| PDMS | Polydimethylsiloxane |
| PEG | Polyethylene Glycol |
| PEN | Polyethylene Naphthalate |
| Pen-Strep | Penicillin-Streptomycin |
| Phallo | Phalloidin |
| PI3K | Phosphatidylinositol 3-Kinase |
| PIV | Particle Image Velocimetry |
| PLL | Poly-L-lysine |
| RAS | Rat Sarcoma virus |
| ROI | Region of Interest |
| RPMI | Roswell Park Memorial Institute (medium) |
| Rpm | Revolutions per minute |
| RT | Room Temperature |
| SCH | SCH772984 |
| SD | Standard Deviation |
| SEM | Standard Error of the Mean |
| Sulfo-Sanpah | Sulfosuccinimidyl 6-(4-azido-2-nitrophenylamino) Hexanoate |
| TEMED | Tetramethylethylenediamine |
| TGFβ | Transforming Growth Factor beta |
| TSIP | Tumour Spheres with Inverted Polarity |
| UV | Ultraviolet light |

## Index of content

# 1. Introduction

## 1.1 The interplay between mechanical cues and the progression of solid cancers

Cancer progression and invasion are highly complex biological phenomena that cannot be defined by a single molecular mechanism or pathway. Instead, they involve both genetic and physical changes occurring in the cancer cells as well as in the tissue microenvironment in which they reside[1]. The clinical relevance of cancer physical properties is underlined by the fact that the diagnosis of solid tumours often involves examination of changes in tissue stiffness and density, that can be detected by palpation or imaging techniques such as mammograms. With the discovery of the interplay between molecular and mechanical mechanisms, interest in the mechanobiology of cancer progression has significantly grown. Indeed, over the past decade, scientists have highlighted the importance of mechanical cues such as matrix stiffness, tissue architecture, topography, mechanical stresses, and cell deformation in influencing over-proliferation, tumour growth and metastasis[1,2,3].

For example, various research groups have demonstrated that higher stiffness and more elevated density of the tumour microenvironment are linked to disease progression and more invasive cellular phenotypes[4,5]. Higher stiffness has also been described to promote malignant phenotype of the mammary epithelium in breast tumour microenvironment, by tuning β1, β4, or α3 integrin signalling and expression[6,7]. Interestingly, cancer cells preferentially show greater proliferation and malignant behaviour when matrix stiffness corresponds to the one of target organs in which the tumour commonly metastasizes. For example, breast cancer cells (MDA-MB-231), that metastasize mainly to bone, show greater proliferation on stiff substrates[8], while ovarian cancer cells (SKOV-3), that metastasize primarily to soft fat pad, proliferate more on softer matrices[9]. Moreover, ovarian cancer cells exert higher traction forces on soft substrates and undergo epithelial to-mesenchymal transition (EMT) on these matrices[9].

Several research groups underlined that the organization and topography of the ECM collagen fibers in the mammary tissue suffer drastic dynamic changes during disease progression and metastasis[10,11]. Chaudhuri and colleagues described that aligned collagen fibers of the primary breast tumour environment can decrease the proliferation of non-transformed epithelial breast cells MCF-10A and induce a temporary ‘dormancy status’[12]. They showed

that, on the other hand, the malignant breast cancer cells MDA-MB-231 and MCF-7 circumvented these growth inhibitory topographic cues and continued their uncontrolled proliferation[12]. Other researchers have recently described that the presence of highly aligned collagen fibers is a negative prognostic factor in pancreatic ductal adenocarcinoma biopsies[13]. The re-organization of collagen fibers is not only typical of pancreatic and breast cancers but is also observed in other tumour microenvironments such as for example in melanomas. Indeed, Kim and colleagues described that highly invasive 1205 Lu melanoma cells are able to modify local collagen organization within a 3D matrix via exertion of considerable traction forces. Moreover, they found out that, when this re-organization was mimicked using aligned nano-fabricated ECM fibers, metastatic cells were in turn induced to align, elongate and migrate, following the local ridge orientations[14].

Cancer onset and progression could be affected not only by ECM organization and topography: indeed, tissue architecture has recently been described as another key factor influencing tumour initiation and invasion[15]. Diverse architectural properties of tissues, including their geometry, confinement, and fluidity, exert different mechanical stimuli on cancer cells within a tumour[16]. For example, the different local forces created by the heterogeneous tumour architecture have diversified consequences on the invasive behaviour of cancer cells[15]. Moreover, tumour growth and shape, conditioned by mechanical tension and spatial restrictions among other factors, affect the differentiation of genetic subclones in cell renal carcinoma, thus demonstrating an interplay between architectural intratumor heterogeneity and cancer evolution[17]. In the pancreas, the heterogeneous geometry of the pancreatic duct determines early morphogenesis of two types of malignant lesions. Transformation in ducts with a diameter of 17 μm or above leads to the formation of lesions that grow into the duct lumen, while the higher curvature of narrower ducts forces early tumours to grow outward with respect to the duct lumen[18].

Apart from stiffness, ECM and tissue topology, other mechanical cues regulating cancer growth, migration and metastasis are compressive stress, shear stress and mechanical stretching[1,2,3]. The latter is caused by tumour interstitial fluid pressure which is usually higher than normal tissues due to the abnormalities in the lymphatic circulation and cancer vasculature[19]. The mechanical stretching induced by interstitial fluid pressure results in increased proliferation of cancer cells[20]. Under *in vivo* condition, cancer cells can be exposed

also to stress generated by the interstitial flow within the tumour microenvironment and stress produced by the blood stream within the circulatory system (shear stress). Shear stress affects tumour cell cycle progression via the activation of integrin receptors, and this mechano-transduction process is dependent on cancer cell types and magnitude of shear stress applied[21,22]. Due to uncontrolled proliferation of cancer cells, tumours exert pressure on the ECM and neighbour tissues, which in turn exert compressive forces or stresses on the malignant mass[2].

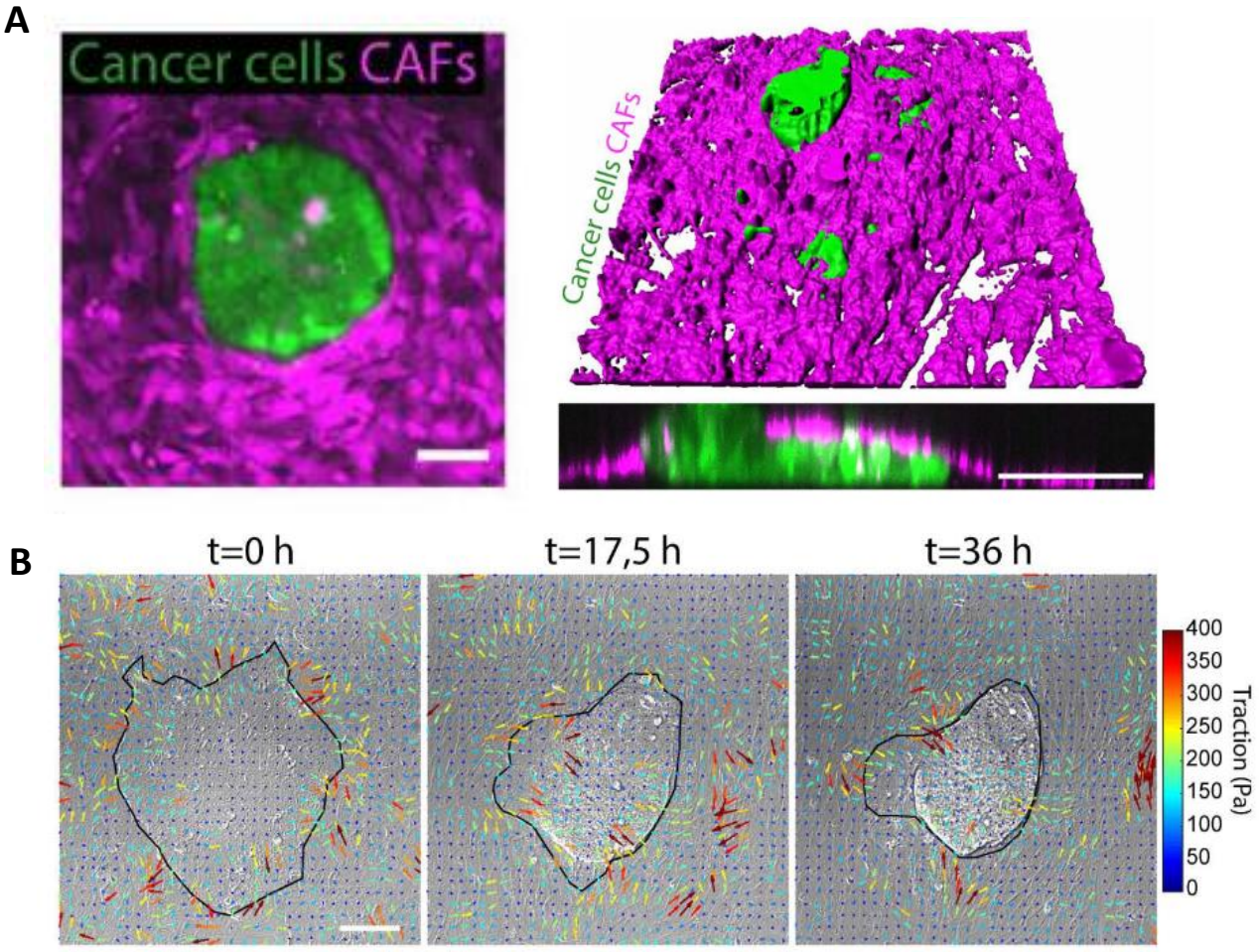


***Figure 1.1.*** *(A) Representative cluster of primary cancer cells (green) surrounded by CAFs (magenta). On the right: 3D rendering of co-culture after 48h in culture. Lower panel, orthogonal Z section. (B) Traction maps of a cancer cell-CAFs co-culture, showing how CAFs compress cancer cells. Black line: contour of cancer cell cluster. Scale bars: 100 µm. Readapted from Barbazan J. et al., (2021).*

Lastly, also compressive stress could play a pivotal role in regulating cancer growth and progression. For example, Barbazan and colleagues have recently discovered that cancer associated fibroblasts (CAFs) form a sort of capsule surrounding the tumour that actively compresses cancer cells using actomyosin contractility and acts as a protection barrier. This study reveals that this contractile capsule compresses cancer cells, modulating their mechanical responses, and reorganizing tumour morphology[23] (figure 1.1).

Taken together, these examples underline that mechanical microenvironmental cues play an essential role in influencing cancer growth, tumour development and metastasis. Understanding and fine-tuning the mechano-responses of cancer cells and tissues to these cues, could ideally lead to the discovery of novel therapeutic targets and to the development of new mechano-medicines or mechano-based therapies. However, redundant cellular functions and tissue complexities might render therapeutic interventions less effective. Therefore, the use of combined therapies that appropriately identify and target the most critical cues for cancer progression may be essential for the success of mechano-medicines[24].

For example, combining treatments against RAS genes, which are the most commonly dysregulated oncogenes in human tumours[25], with mechano-therapeutics, targeting cell adhesion or mechano-sensing machinery, could provide the potential for effective treatments of RAS-driven tumours. Indeed, promising synergistic effects of targeting focal adhesion kinase (FAK) and KRAS oncogene have already been shown in distinct cell lines and patient-derived xenografts[26], with various clinical trials taking place currently[27].

### 1.2 The role of RAS oncogenes in controlling multicellular mechanics

Rat sarcoma virus family genes, namely KRAS, NRAS, and HRAS are the most frequently dysregulated oncogenes in human cancers[25]. RAS proteins are small plasma membrane-associated GTPases that, under physiological conditions, are activated by growth factors that bind to surface transmembrane receptors[28]. Their activation results in the induction of various downstream signalling cascades, including the mitogen-activated protein kinase/extracellular signal-regulated kinase (MAPK/ERK) pathway[29] and the phosphatidylinositol 3-kinase (PI3K) pathway[30], that promote cell growth, cell cycle entry, and cell survival. Oncogenic RAS activation causes the hyperactivation of these pathways in the

absence of a ligand or receptor activation. This hyperactivation results in signal-independent cell over-proliferation and, eventually, cancer.

It has long been known that, unlike most other oncogenes, RAS signalling could also alter cell adhesion[31] and cause changes in cell cytoskeleton[32]. These alterations change both the mechanical properties of cells and how they interact with and sense their mechanical environment[33]. Several recent studies have demonstrated how RAS-dependent alterations in cell mechanics could lead to large-scale deformations of epithelial tissues (figure 1.2), including buckling and folding[18,34]. These deformations are likely to contribute to the loss of tissue architecture occurring during tumorigenesis[33].

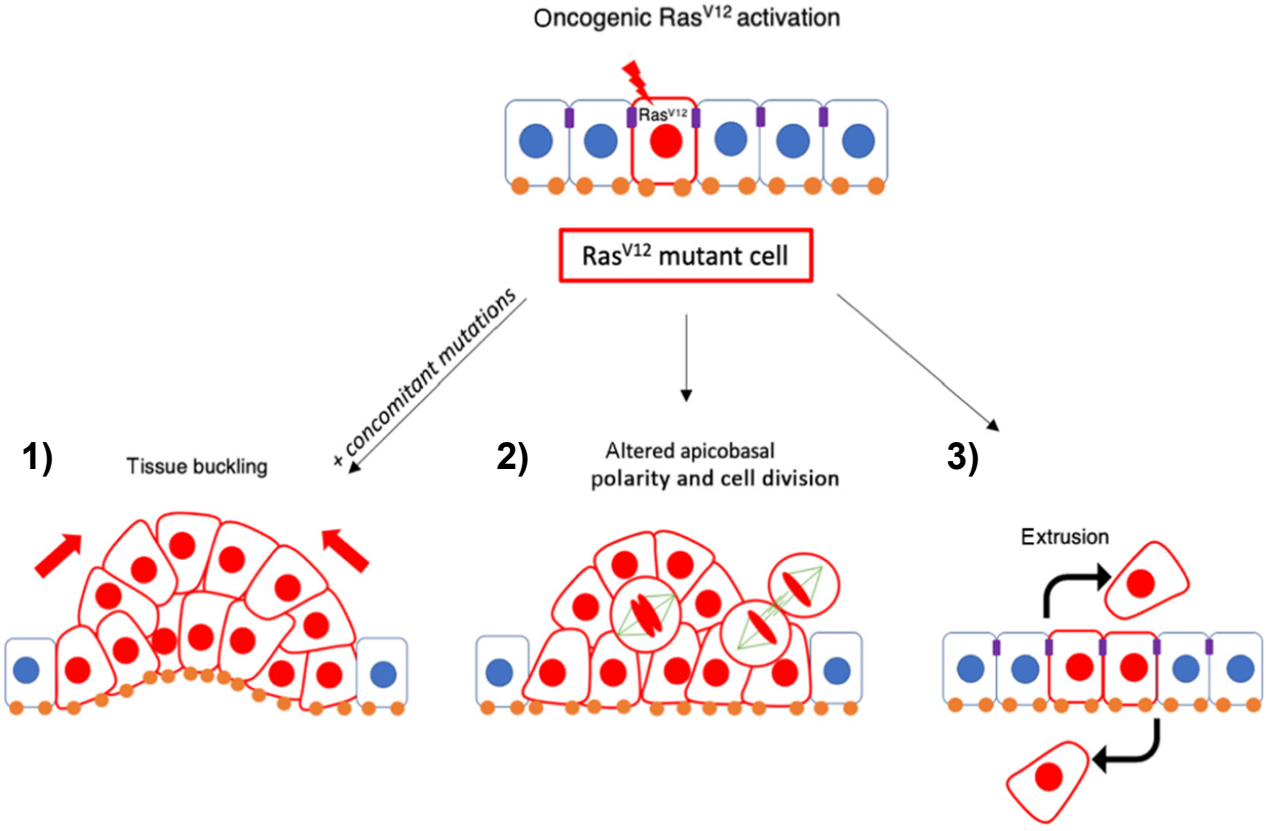


***Figure 1.2.*** *Oncogenic RAS activation can drive the misshaping of transformed epithelia, which can then acquire other common mutations. 1) Oncogenic RAS drives cell proliferation and hyperplastic growth. Consequent changes in substrate and/or cellular stiffness can lead to tissue buckling. 2) RAS-driven changes in cell contractility and adhesion can also impact cell divisions and tissue polarity. 3) RAS mutations can initiate cell competition within tissue, which leads to basal or apical cell extrusions. Cartoon readapted from Nyga* et. al*, (2022).*

The consequences of RAS activation within an entire tissue depend on the number of cells where RAS is activated. Indeed, when initiating oncogenic mutations occur in a small group of cells surrounded by non-transformed epithelium, mutant cells can be eliminated due to a mechanism called cell competition[35]. Cell competition can also lead to different outcomes that involve alterations in cell mechanics. For example, differences in the mechano-sensing machinery between cancer and noncancer cells can lead to cell death[36], and the hyperactivation of RAS can cause the apical or basal extrusion of transformed cells from the monolayer[37]. Although cell extrusion is commonly regarded as a defence mechanism of epithelia, transformed cells can hijack this mechanism to ultimately enable distant organs invasion[15]. Moreover, since epithelia are able to accumulate cells with somatic mutations, extrusion is not an error-free process[38]. The maintenance of conspicuous group of activated RAS cells in an epithelium could result in whole-tissue hyperplasia and morphological transitions[39].

Indeed, activation of RAS within cell clusters can cause large-scale morphological tissue rearrangements. For example, our lab has recently showed that the activation of oncogenic HRAS in confined human breast epithelia causes cell monolayer compacting to a 3D aggregate, a phenomenon caused by changes in the distribution of cellular tension and by mechanical instability at the tissue level[39]. Fiore and colleagues have also shown that, during early morphogenesis of squamous cell carcinoma, HRAS activation causes the formation of abnormal basal folds with an invaginated apical surface[34].

In pancreatic ducts, the mosaic activation of oncogenic KRAS coupled with the deletion of the tumour suppressor Fbw7 or p53, leads to ductal size-dependent formation of two distinct typologies of oncogenic lesions that developed either apically, either basally[18]. Activation of oncogenic KRAS was also shown to disrupt the morphology and the correct apical-basolateral polarity of 3D colonic epithelial cysts[40].

The mechanical impact of RAS oncogenes activation can also affect wild-type surrounding tissues. For example, in the *Xenopus laevis* embryonic epithelium, clusters of KRAS-expressing cells form tumour-like structures characterised by high contractility and tension[41]. This elevated tension originates not at the boundaries between KRAS and wild-type cells, but from

mutant KRAS cell clusters, whose increased contractility is sufficient to alter the orientation of dividing cells in the adjacent wild-type tissue[41].

Overall, these studies reveal how the activation of RAS oncogenes can induce tissue-level alterations. In the future, it will be crucial to assess how these mechanical changes could influence tissue growth and shape in a more complex human tissue or tumour microenvironment[33]. Indeed, a better comprehension of the contribution of RAS to the interplay between oncogenic cells and their microenvironment could potentially lead to the development of new therapeutic strategies in preventing cancer progression.

### 1.3 The role of mechanical cues in Colorectal carcinomas progression

Among the different solid tumours in which RAS oncogenes could be mutated, colorectal carcinoma (CRC) is one with the highest incidence and morbidity. Indeed, KRAS oncogene is mutated in about 40% of patients with CRC[42].

According to the World Health Organization, colorectal carcinomas correspond to the third-leading cause of tumour related-death. Colorectal carcinomas are not a homogeneous group of tumours, but they rather evolve through distinct genetic and epigenetic pathways. Most of these carcinomas arise through the chromosomal instability pathway, which is originated by the loss of function of adenomatous polyposis coli (APC) gene[43,44]. However, colorectal carcinomas with poor prognosis mainly derive from the CpG island methylator phenotype (CIMP) sub-group[45,46,47], characterized by initiating mutations of BRAF or KRAS oncogenes, that constitutively activate the mitogen-activated protein kinase (MAPK) pathway[47,48].

Approximately 10% of these hypermethylated tumours progress toward microsatellite instability (MSI-high), while most of them remain microsatellite stable (MSS) or display an intermediate phenotype, defined as MSI-low[48,49]. CIMP carcinomas originate from serrated polyps and evolve toward specific histological subtypes of colorectal carcinomas with negative outcome, namely mucinous, micropapillary and cribriform[50,51]. The high rate of mortality of these CRCs subtypes is principally attributed to the metastasis of neoplastic cells from the primary tumour to secondary organs such as the liver, the lung and the peritoneum, which is a serous membrane surrounding the abdominal organs[52,53]. Cancer cells could reach the peritoneal cavity via systemic circulation or by full-thickness invasion of the digestive wall.

They then adhere to the peritoneum and invade through the connective tissue, producing various metastatic nodules, which drastically worsen patient prognosis[53,54]. Understanding how non-invasive tumours become metastatic is the most prominent goal in current colorectal cancer research. Indeed, metastasis represents the main current medical challenge in the therapeutic care of CRC patients. Even though new treatments have roughly doubled the average survival time for advanced CRCs, patients usually die within three years[55].

The multi-step genetic alterations leading to CRC metastasis are accompanied by profound mechanical changes occurring at the cellular and the tissue level. A growing consensus is emerging that these mechanical modifications are not merely a by-product of the malignant progression, but they could play a relevant role in cancer initiation and even accelerate its spread[24,56]. Several studies have highlighted that physical stimuli may play a fundamental role in the differentiation of non-invasive cells into metastatic variants and in triggering morphological transformations of solid tumours. Researchers also showed that colorectal cancer cells are able to modify their metastatic and mechanical properties, such as stiffness and adhesion, to adapt to substrates with different elasticity and to survive the mechanical stress associated with intravasation, circulation and extravasation[57,58,59]. For example, Tang and colleagues demonstrated that the metastatic potential of colorectal cancer cells HCT-8 cells, measured via cell deformability, *in vitro* and *in vivo* invasion assays, could be drastically increased by culturing these cells on fibronectin-coated substrates with stiffness ranging from 21 to 47 kPa[57]. Such stiffness range mimics the rigidity of the colorectal tumour microenvironment, thus being suitable to reproduce the mechanical stimuli sensed by cancer cells during pathological conditions[57]. Moreover, Shen and colleagues recently showed that in metastatic colorectal carcinomas, highly activated fibroblasts increase tissue stiffness, which enhances angiogenesis and anti-angiogenic therapy resistance[58]. They then demonstrated that targeting tissue stiffness in these metastatic settings using mechano-drugs such as Losartan and Captopril could improve the therapeutic outcome of anti-angiogenic treatments[58] (figure 1.3).

Indeed, with the recognition of tissue stiffening in the progression of cancer and other diseases such as fibrosis and cardiovascular disease, novel mechano-based therapies and mechano-medicines targeting increased tissue stiffness and/or associated cellular responses are emerging as clinically relevant strategies[59]. However, a deeper comprehension of the

mechanical alterations arising during colorectal carcinomas progression and metastasis is needed to help defining new potential targets for the cure of these tumours. These mechanical alterations are linked to morphological changes via physical mechanisms occurring at the supracellular scale, that could be described through macroscale variables such as tractions, stresses, or velocities. Such morphological changes or transitions occur in colon epithelia during malignant transformation and mark the different steps of colorectal cancer progression.

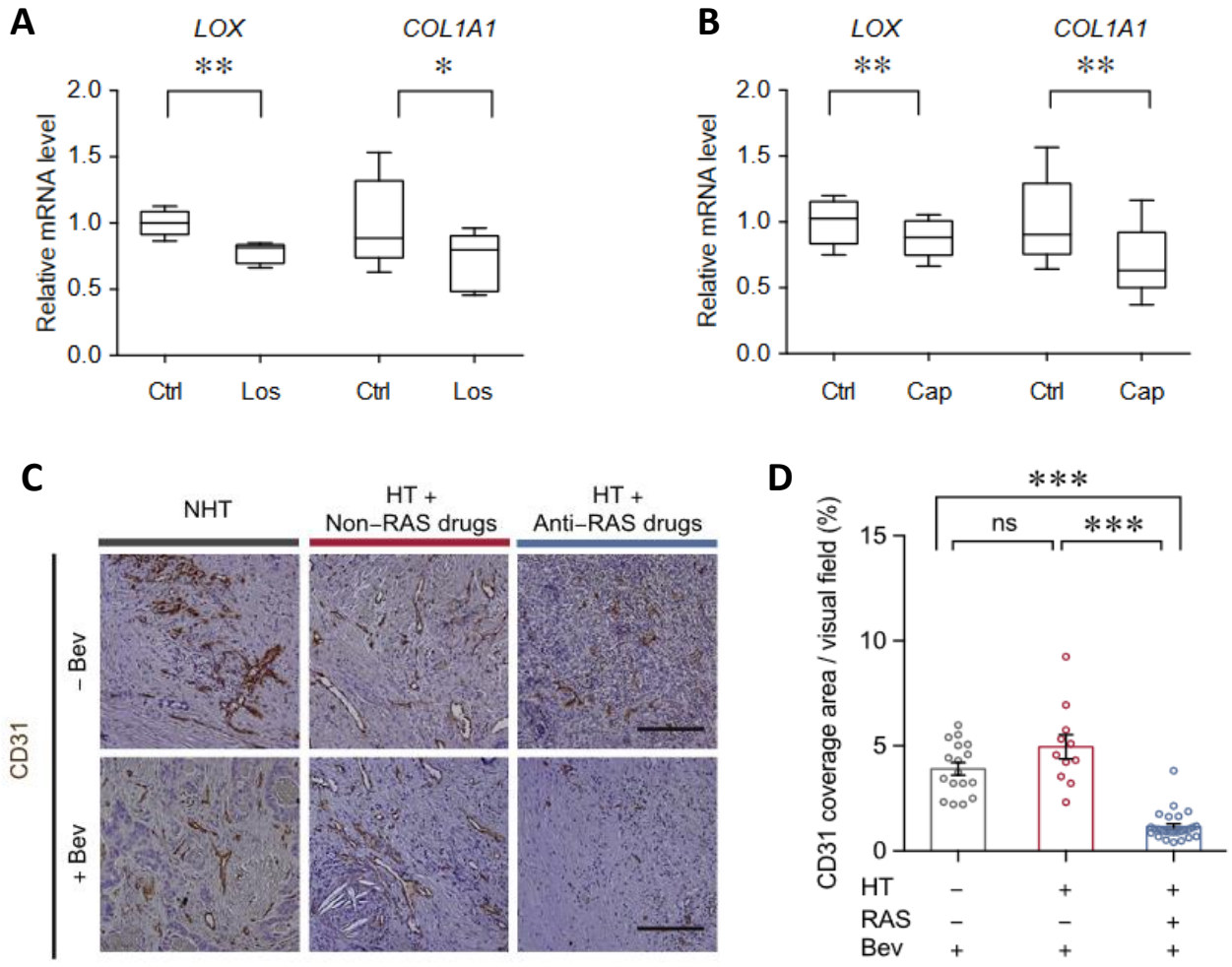


***Figure 1.3.*** *(A and B) qPCR for Lysyl Oxidase (LOX) and COL1A1 after 24 h treatment with anti-RAS drugs losartan (A) or captopril (B). (C) CD31 staining on liver metastasis sections of CRC patients, showing that anti-RAS drugs potentiate the effect of anti-angiogenic Bevacizumab. Scale bars: 150 µm. (D) Quantification of CD31 coverage area in the different conditions. Bev, bevacizumab; NHT, no hypertension patients; HT, hypertension patients. Readapted from Shen Y. et al, (2020).*

## 1.4 Multicellular morphological transitions in epithelial monolayers

Living tissues are active materials with the ability to undergo drastic shape and dimension transitions[60]. Such morphological changes are fundamental in various physiological phenomena such as for example embryonic development, regeneration, and wound healing. Shape transitions in living tissues are genetically choreographed by various molecular processes, but their execution is essentially a series of mechanical events, occurring at a supracellular scale[61]. Therefore, tissue or organ shape results from the interplay between genetics and tissue mechanics[61,62]. Understanding how this interaction between multicellular mechanics and genetics controls tissue shape is of key relevance. Indeed, if this interplay is not properly regulated, the subsequent aberrant morphological transitions could cause developmental defects and tumour formation[61,63].

Among others, some examples of malignant morphological transformations occurring at a supracellular level are monolayer dewetting[39,64] and cancer budding[18,65].

### *1.4.1 Budding phenomena in biology*

Budding occurs when cells within an epithelium start protruding through apical constriction and subsequently extend in a direction that is orthogonal to the plane of the original epithelium. In budding, cells extend out from the original epithelium forming a dome or a compact cell cluster as the bud grows[66]. Orthogonal extension of the bud can occur through different mechanisms: additional cell recruitment, cell division and/or cell elongation. Budding is the phenomenon through which many organs develop during morphogenesis, including mammalian lungs and the major branches of the Drosophila tracheal (respiratory) system[67,68]. Other examples of organs in mammals that correctly develop via budding include the kidneys, blood vessels, pancreas, the heart and central nervous system at early developmental stages and the mammary, as well as salivary and lacrimal glands[69]. These organs can vary significantly in size and shape but, whether they are highly intricate networks of branched tubes or simple cylinders, they all comprise a polarized epithelium that surrounds a shared central lumen[69]. The apical (or free) surface of each epithelial cell faces the lumen, whereas the basal surface faces surrounding tissues.

Budding could happen in mono-stratified as well as in pluri-stratified epithelia. Branching morphogenesis in a single-layered epithelium requires buckling of the monolayer sheet[70]. For example, the branching of single-layered lung epithelium is guided by buckling induced by external shaping forces exerted from smooth muscle cells[71,72], among other cell types[73]. In stratified epithelia, however, the concept of buckling cannot be easily applied due to the apparent lack of a sheet-like structure and the absence of a lumen.

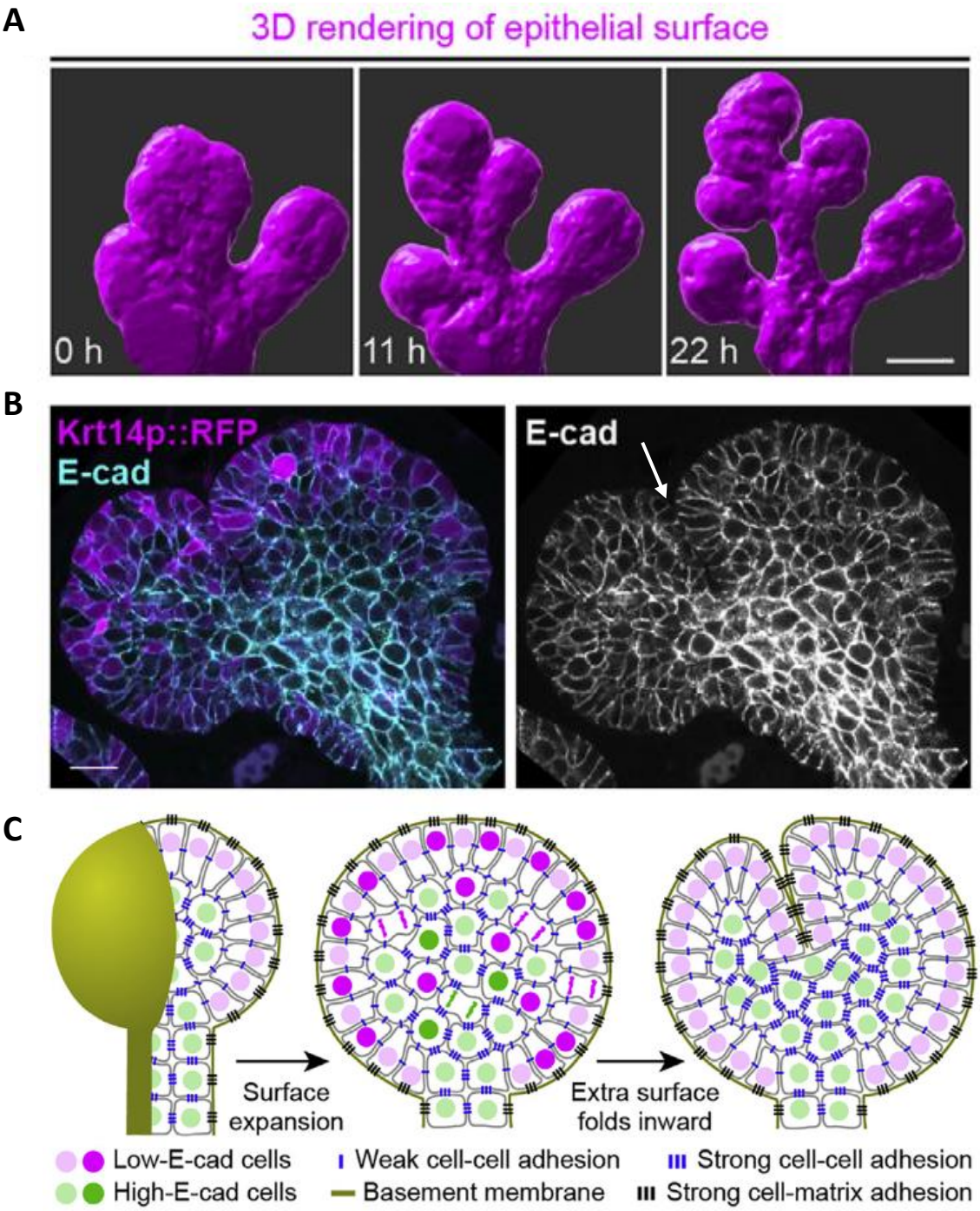

***Figure 1.4.*** *(A) 3D rendering showing the development of mouse salivary gland. (B) Confocal images showing an epithelial bud at 23 h. White arrow indicates the point in which the external epithelial sheet is folding. (C) Schematic model of clefting in a stratified epithelium. Brighter colour indicates dividing and newly divided cells. The two steps happen simultaneously but are shown separately for clarity. Readapted from Wang et al., (2021).*

In 2021, Wang and colleagues extensively elucidated the phenomenon of budding morphogenesis in stratified monolayers. Employing live-organ imaging of mouse embryonic salivary glands, they discovered that stratified epithelia budding is governed by expansion and folding of a distinct epithelial cell sheet characterized by strong cell-matrix adhesions and weak cell-cell adhesions. Single-cell transcriptomes of this epithelium revealed peculiar spatial patterns of transcription causing these cell adhesion differences. They then mimicked synthetically budding morphogenesis by experimentally suppressing E-cadherin expression and inducing basement membrane formation in 3D spheroid cultures of engineered cells. In this engineered model, cells required β1-integrin-mediated cell-matrix adhesion for successful budding. Therefore, they revealed that, in stratified epithelia, the first fundamental step of branching morphogenesis is governed by the combination of strong cell-matrix adhesion with weak cell-cell adhesion by epithelial cells (figure 1.4).

These results uncover a self-organizing mechanism based on preferential cell matrix adhesion rather than cell-cell adhesion that could clarify how stratified epithelia undergo budding morphogenesis[74]. Apart in morphogenesis and development, budding phenomena could arise also in pathological conditions such as for example in cancer.

#### 1.4.1.1 Budding in tumour progression

Interest in tumour budding and its clinical implications has risen over the past few years. In oncology, tumour budding is canonically defined by the presence of single cancer cells or small clusters of cells within the tumour centre (‘intratumoural’ budding) or at the tumour-invasion front (‘peritumoural’ budding)[75]. Tumour budding occurs in a large variety of cancers from different organs[76]. The frequency of tumour budding is difficult to estimate, due to the use of different scoring and classification systems, but it might be found in approximately 40% of colorectal cancers[77], oesophageal cancers and gastric cancers[78,79], as well as in more than 50% of pancreatic ductal adenocarcinomas[80]. Tumour budding was also reported to occur in many other tumour types, such as lung adenocarcinomas and squamous cell carcinomas[81,82],

as well as cervical[83], ovarian[84] and breast[85,86]cancers. Recent data suggest that the presence of tumour budding is an unfavourable prognostic factor across all tumour types in which it is found, as it is highly associated with lymph node metastasis, local recurrence and distant metastatic disease[87].

In 2019, Messal and colleagues described a peculiar typology of tumour budding in pancreatic cancer. They showed that the morphology of pancreatic epithelial tumours is determined by the interplay between the existing tubular geometry of the monolayer and cytoskeletal changes happening in malignant cells[18]. They found out that oncogenic transformation of pancreatic ducts led to two distinct typologies of neoplastic growth: endophytic lesions that expand inwards to the ductal lumen and exophytic lesions that grow outwards from the duct (figure 1.5).

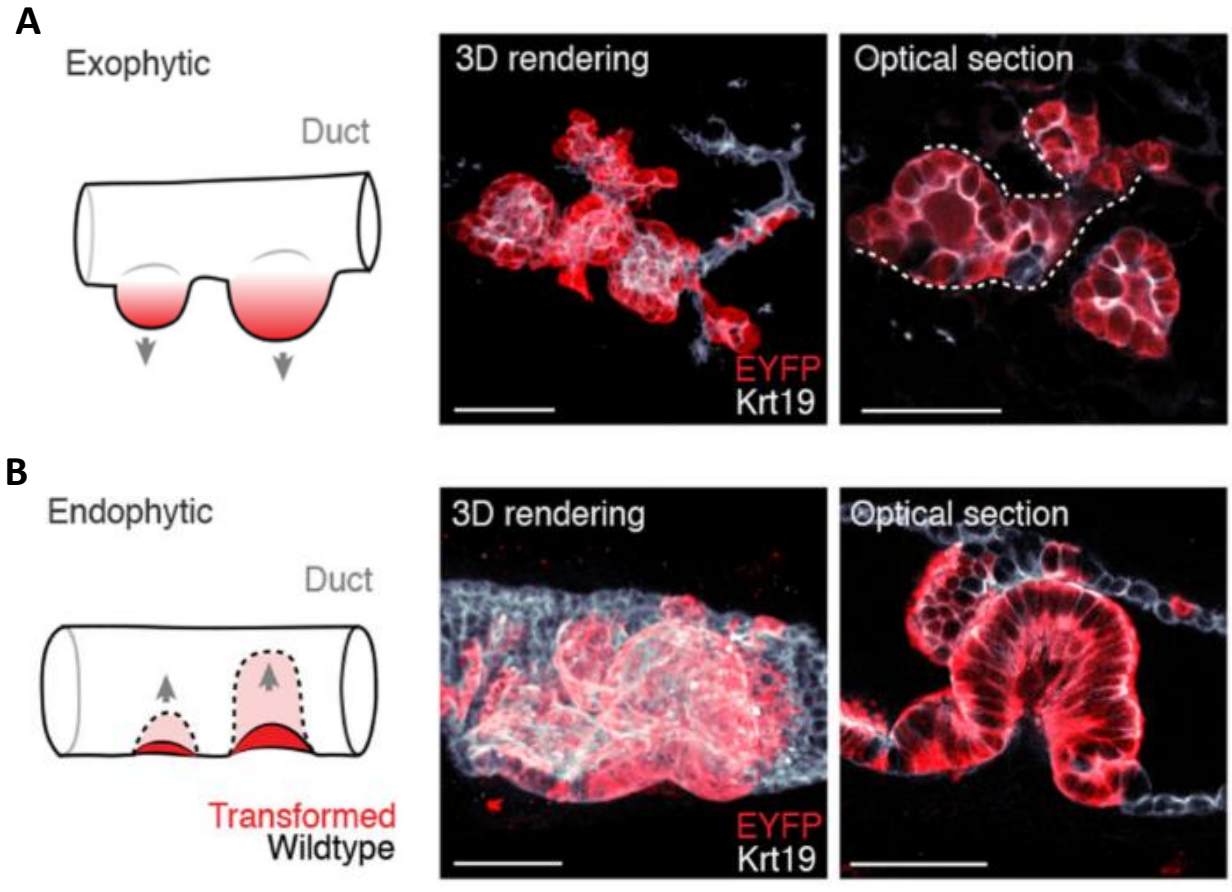


***Figure 1.5.*** *(A) Cartoon, 3D rendering and optical section of an exophytic lesion in pancreatic ducts. (B) Cartoon, 3D view and optical section of an endophytic deformation in pancreatic ducts. Transformed cells are showed in red. Readapted from Messal et al. (2019).*

Interestingly, their three-dimensional (3D) whole organ imaging revealed that large ducts deformed endophytically, while small pancreatic ducts produced exophytic lesions. Similar patterns of lesion growth were also observed in tubular epithelia of lungs and liver, identifying tissue curvature and tension imbalance as fundamental determinants of epithelial tumorigenesis[18]. They demonstrated that the local curvature of the source epithelium, together with mechanical changes occurring in the transformed cells, govern the direction of epithelial deformation and ultimately dictate tumour morphology[18]. Overall, Messal and colleagues, described a novel multicellular morphological process in which cohesive clusters of cells collectively adopt a malignant bud-like phenotype.

The idea that tumour cell clusters could contribute to metastasis can be traced back to the 1950s, when it was stated that blood samples from cancer patients contain both single and clustered tumour cells[88] and that tumour cell clusters could rapidly traverse the lungs in rabbit and rat models[89]. Later, it was shown that cancer cell clusters were more efficient than single cells at producing metastases, if injected intravenously into mice[88,90]. Several studies focusing both on patient samples and on preclinical models, have agreed on the thesis that cancer cells can metastasize collectively as cohesive clusters[89,65]. These tumour cell clusters can preserve epithelial gene expression and might switch between distinct epithelial differentiation states to achieve both the proliferative and the migratory components of metastasis[91].

Despite the growing interest in the field, various are the questions still far to be addressed: which are the biological foundations of metastatic seeding by budding and tumour cell clusters? Which are the morphological events leading to the emergence of mature buds? Which are the biophysical mechanisms involved in the onset of budding? Are there any cellular and molecular properties of budding which are common across different tumour types and metastatic sites? What are the therapeutic implications of budding and tumour cell clusters? The answers to these questions will ideally lead to the identification of novel therapeutic strategies that will target the morphological changes occurring in epithelia before the emergence of mature buds and/or the multicellular organization of tumour cell clusters.

#### 1.4.1.2 Budding in colorectal cancer

In pathology and oncology, tumour budding in colorectal cancer has recently become an important prognostic factor. The first guidelines for colorectal carcinomas to report tumour

budding were published in 2017, following the 2016 International Tumour Budding Consensus Conference (ITBCC)[75]. Tumour budding in CRCs is indicative of tumour progression and adverse prognosis[92], as it is associated with local recurrence, lymph node metastasis, and distant metastatic spread[87].

In 2018, Zajac *et al*. described the budding as a morphological phenomenon leading to the formation of cohesive tumour spheres in hypermethylated colorectal carcinomas. This study revealed a novel cellular modality of peritoneal metastatic spread. Zajac and colleagues started from examination of cells recovered from the peritoneal effusion of around 50 patients with CpG island methylator phenotype (CIMP) colorectal cancer, a subtype known to associate with a high rate of metastatic recurrence. This fluid contained large clusters of cancer epithelial cells that displayed an outward apical polarity and were therefore termed tumour spheres with inverted polarity (TSIPs) (figure 1.6.A). The authors then quantified cluster frequency across colorectal cancer subtypes and in relation to the presence of peritoneal metastases. They discovered that these cancer clusters were most frequent in subtypes associated with poor patient prognosis, such as cribriform, micropapillary and mucinous (figures 1.6.B and 1.6.D). Interestingly, they also noticed a striking correlation between the absence of peritoneal metastases and the absence of TSIPs in peritoneal effusions[65] (figure 1.6.B). The authors conclude that these cell clusters are 'in the right places at the right times' to seed metastases[93].

During the process of spreading, these cohesive groups of cells maintained their apical-out topology and employed acto-myosin contractility to collectively invade three-dimensional extracellular matrices. They also demonstrated that TSIP-like structures could be identified across multiple stages of invasion and metastatic spread in patient tissue samples, further corroborating the thesis that they could play a fundamental role in cancer dissemination (figure 1.6.C). These clusters of cells originate and propagate down-stream of both canonical and non-canonical TGFβ signalling, through a series of morphological changes[65]. The detailed morphological steps of this phenomenon are still far from been clarified. In order to shed light on this multi-step malignant process, one of the goals of this PhD project is to decipher the collective physical mechanisms leading to the formation of buds in KRAS-mutated colorectal carcinomas epithelia.

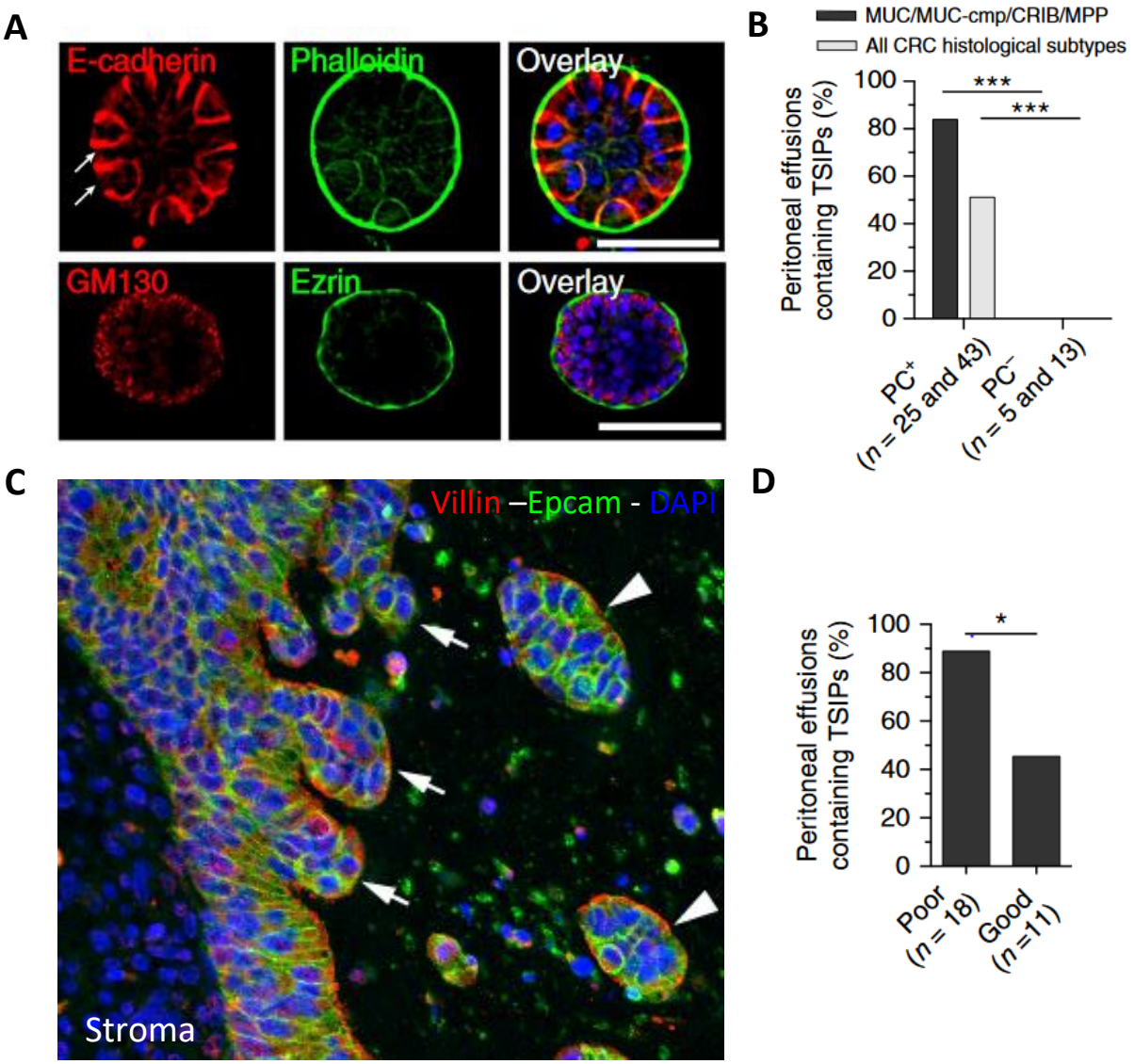


***Figure 1.6.*** *(A) TSIPs collected from patients' peritoneal effusions and stained for E-cadherin, Phalloidin, Ezrin and GM130 (cis-Golgi matrix protein). Arrows point to the lack of basolateral markers at the apical membrane. (B) Correlation between TSIPs and patient metastatic status (PC+, patient with peritoneal metastasis; PC–, patient without peritoneal metastasis) (C) Section of a primary tumour showing budding structures (arrows) and TSIPs (arrowheads). (D) Correlation between the frequency of TSIP positive peritoneal effusions and patient outcome. Readapted from Zajac et al. (2018).*

### *1.4.2 Dewetting of epithelial tissues*

Apart from tumour budding, another example of morphological transitions occurring on a supracellular scale is the dewetting of epithelial tissues.

Wetting models have classically been used to elucidate the dynamics of liquid-solid interfaces. In general, the spreading of a liquid drop on a substrate it is forced to cover is described

as wetting, while dewetting is defined as the process of retraction of a fluid from a non-wettable surface[94] (figure 1.7).

When a liquid drop is forced to contact a solid surface, its spreading dynamics depend on the balance between the liquid-surface adhesive forces and the drop cohesive forces. This could lead to various wetting typologies: the liquid drop might totally spread creating a thin film (complete wetting), or it could remain as a drop in a partial wetting state, creating a certain contact angle with the surface. Conversely, a liquid thin film forced to cover a substrate could continue to wet the surface or might retract in a dewetting process[94].

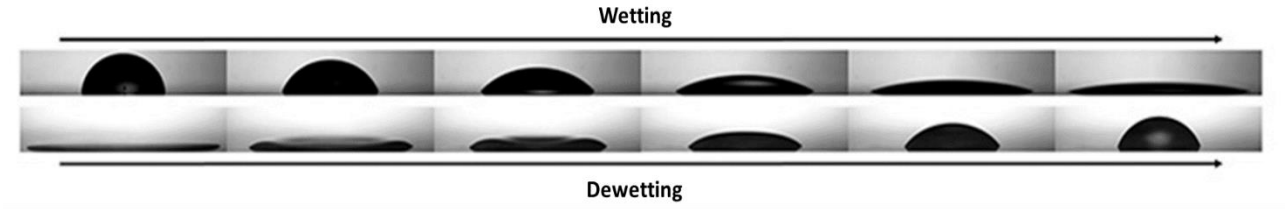


***Figure 1.7.*** *Schematics representing wetting and dewetting of a liquid drop. Readapted from Edwards et al. (2016)*

Dewetting phenomena could cause the formation of holes in the liquid film, which can subsequently merge to form networks and break into liquid droplets. Examples of dewetting have been described in systems such as soap foams, polymeric films or protein films on different substrates[95,96]. These networks of dewetted polymers are spontaneously established in nature and have been extensively studied; one example are the vascular networks formed by endothelial cell lines such as human umbilical vein endothelial cells (HUVEC) or human dermal microvascular endothelial cells (HDMEC)[97,98].

Given the fluid behaviour of cell aggregates, their spreading on a certain substrate could be considered as a wetting state[60]. On the other hand, the retraction of an epithelium, leading to the formation of three-dimensional cellular structures could be seen as a dewetting process[99,100]. In cellular monolayers, the spreading dynamics rely on the competition between cell-substrate and cell-cell interactions[60]. In these systems, cell-substrate interactions depend on stiffness and on substrate chemical properties, while intercellular adhesion depends on the expression of molecules such as E-cadherins[60]. For example, culturing mouse sarcoma cells on soft substrates or on non-adhesive PEG-coated substrates was enough to trigger

spontaneous cellular retraction (dewetting) from the surface to form aggregates[99]. Monolayer dewetting has also been described in a human breast adenocarcinoma cell line, MDA-MB-231, where the overexpression of E-cadherin caused a morphological transition from flat epithelia to 3D spheroid-like structures[64] (figure 1.8.A). Another example of monolayer dewetting was recently described by our group in MCF10A human epithelial monolayers. Indeed, we showed that the inducible expression of HRAS oncogene in confined MCF10A epithelia, drives a morphological transformation of a 2D monolayer into a compact 3D cell aggregate (figure 1.8.B). This alteration is initiated by the loss of monolayer integrity and the formation of two distinct cell layers having differential tensional states, cell-cell junctions and cell-substrate adhesion[39] (figure 1.8.C). These findings reveal the interplay between genetic alterations, such as HRAS oncogene induction, and mechanical instability to drive morphological tissue transformation.

However, it is complicated to anticipate where these mechanical instability-caused morphological transitions are going to occur within an epithelium.

### 1. 5 The impact of topological defects on morphological transitions

Recent studies have highlighted the pivotal role of topological defects in the emergence of morphological transitions in bacteria films as well as in cell epithelia[101,102]. Topological defects can be described as abrupt changes in the orientation field of molecules or cells. These singularities illustrate the emergence of mesoscopic structures which are smaller than the whole system, but larger than its microscopic components. Strikingly, the presence of these singularities has been found to correlate with the location where 2D to 3D transitions will later occur, therefore becoming a predictor of such morphological changes[101,102].

Topological defects can be found in any system that behaves as a liquid crystal. In such systems, the elements or particles composing them lack a crystalline structure, but they self-align with their long axis parallel to their neighbour's long axis. Such local alignment gives rise to a long-range directional order. When two domains of different long-range directional order meet, a sort of discontinuity is created, named topological defect. Such topological peculiarities are nowadays commonly described in terms of 'charges' associated with different defect typologies. Topological charge is a numerical indicator describing the change in the orientation of the molecules or cells around a given point.

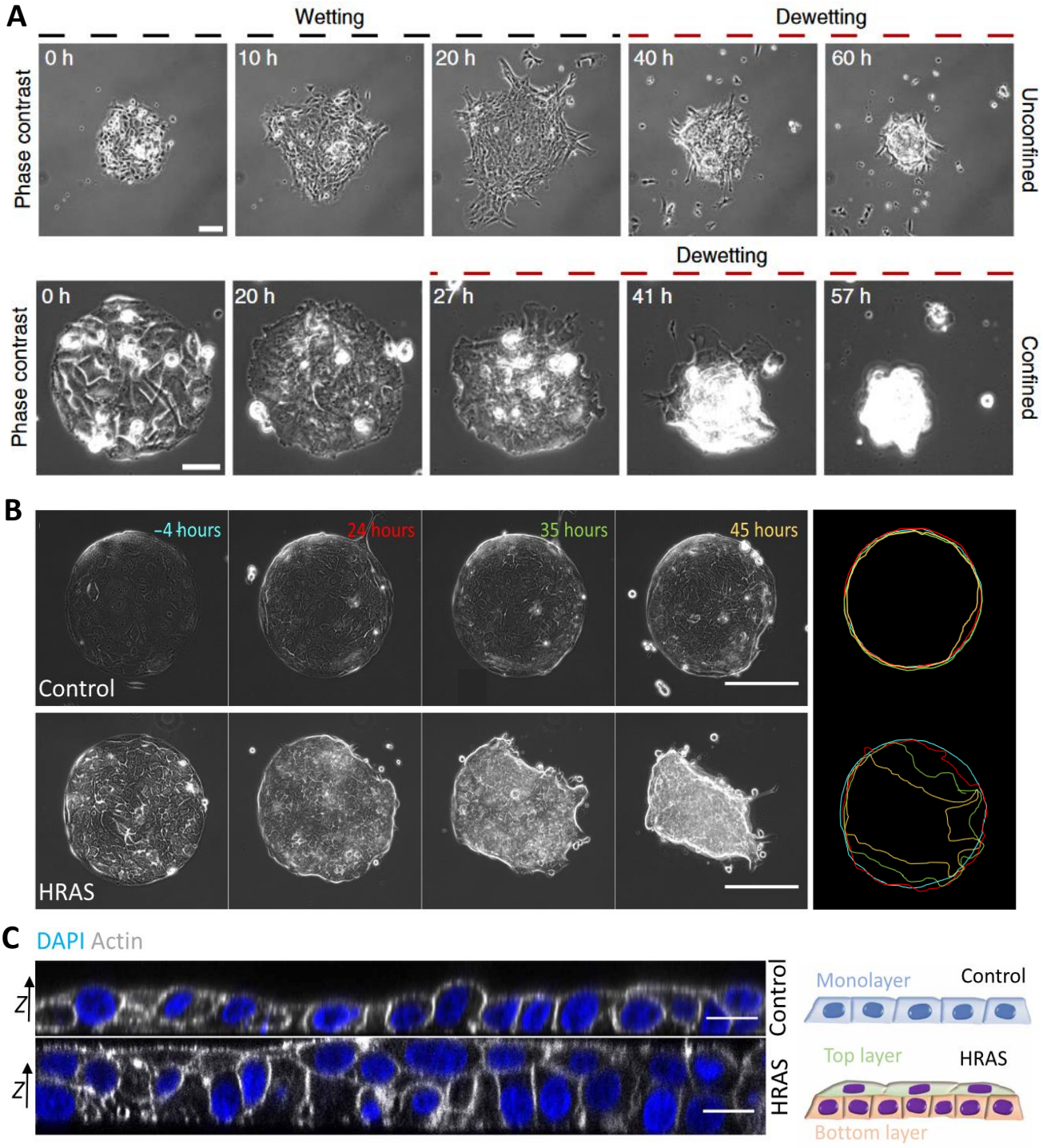


***Figure 1.8.*** *(A) Phase contrast images showing dewetting of unconfined or confined MDA-MB-231. Readapted from Pérez et al., (2019). (B) Left, time-lapses showing dewetting of a MCF10A epithelium with HRAS induction. Right, contours of epithelia shown on the left (time progresses with blue, red, green, and yellow colours). (C) Confocal images and cartoon showing non-transformed monolayer and HRAS-transformed bilayer at 24 hours from oncogene induction. Readapted from Nyga et al., (2021).*

In a two-dimensional system, comet-like and trefoil-like defects are associated with charges of +1/2 and −1/2, respectively. Vortices, spirals or asters-like defects can also be observed and are associated with integer (±1) charges (figure 1.9.A). For +1, +1/2, −1/2 and −1 defects, the molecules turn through +360°, +180°, −180° and −360°, respectively[103]. Topological defects can move and interact with each other based on their charge. They could be virtually found everywhere in nature; for instance, a macroscopic example of an active system with topological defects are the prints observed at the tips of our fingers or on our palm[103] (figure 1.9.B). In 1965, Lionel Penrose classified the topological patterns on fingerprints and palms as comet-like or trefoil-like and showed that the number of these defects was connected to the number of fingers[104]. In active systems, topological defects can arise spontaneously, organized in oppositely charged pairs[105]. The term active system describes any natural or artificial entity that is out of thermodynamic equilibrium because of energy input derived from its individual molecules or cells[106].

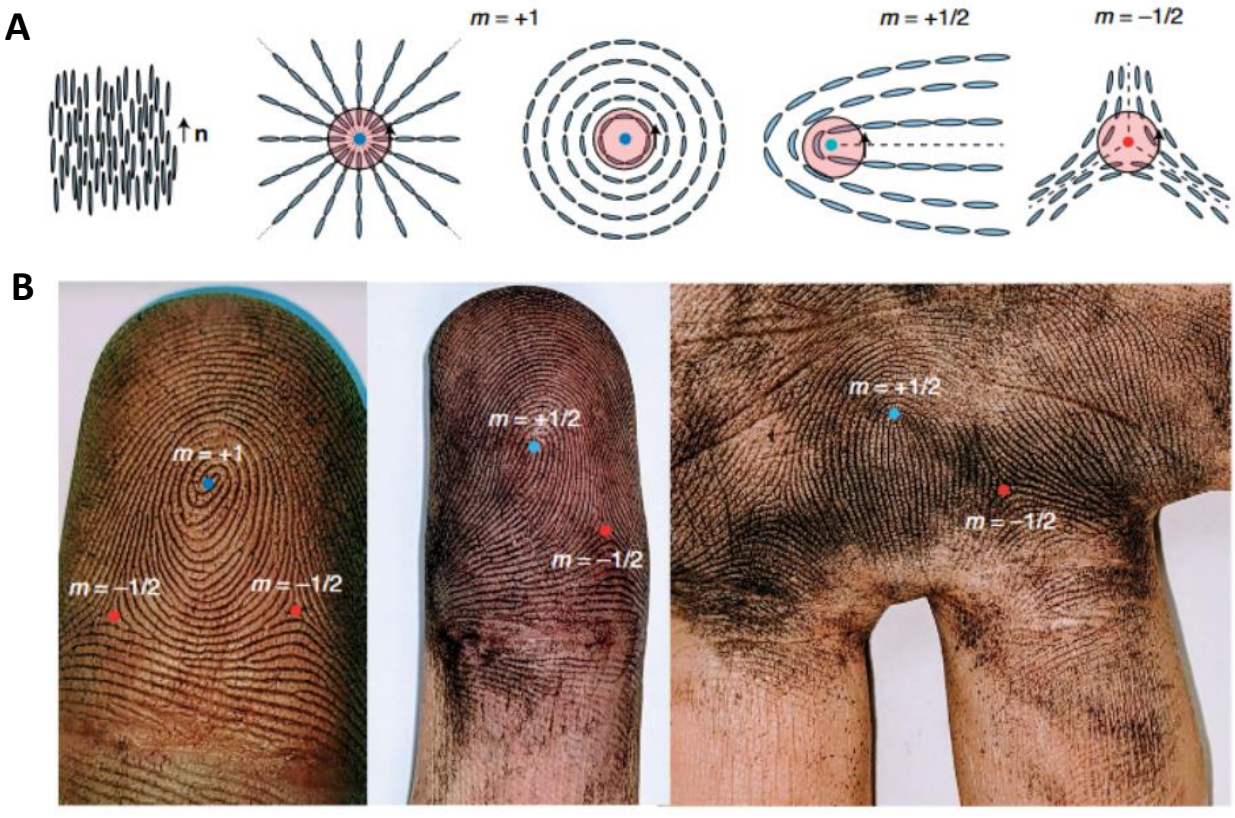


***Figure 1.9.*** *(A) Orientation of an aligned nematic field (**n**) and typical topological defects found in a two-dimensional nematic field. (B) Representative topological defects that can be seen at the tips of the fingers or on the palm. Readapted from Fardin & Ladoux, (2021).*

Various research groups have recently focused on studying topological defects linked to peculiar biological processes such as regeneration or morphogenesis. For example, Maroudas-Sacks and colleagues studied morphogenetic processes in Hydra, a freshwater animal known for its regenerative capacities, and discovered that during regeneration from tissue pieces, the system folded into spheroids that induced the formation of topological defects in the nematic order of the actin fibres, with a total charge of +2. They observed that the emergence of two +1 topological defects coincided with the tip of the head and the base of the foot, therefore defining the animal's body axis. They also described that the formation of Hydra tentacles was associated with topological defects of charge +1 at the tip and two −1/2 at the base. By following actin remodelling in these regenerating animals, the authors noticed characteristic patterns in the coupling between defect dynamics and morphological processes. Indeed, they described that comet-like defects (+1/2), which were predominant at early stages, were mobile and remained unstable, while +1 defects remained mainly stable, and appeared at later stages with the head and the foot of the animal. Interestingly, this asymmetry identified the two poles of the body axis long before the formation of any morphological features[107].

The impact of topological defects on multicellular architecture was also investigated by Katherine Copenhagen and colleagues, who studied colonies of rod-shaped bacteria that, under starvation, could transit from a monolayer to a three-dimensional dome-like structure. The authors described that the initiation of cellular multilayering was localized at comet-like defects (+1/2), whereas holes inside the bacterial monolayer were arising at trefoil defects (−1/2). Moreover, they showed that the +1/2 defects displayed a net movement towards the head of the defect, with cells at the front aligning perpendicularly and the ones at the tail aligning parallel to the flow. The topological orientation of rod-shaped bacteria induced an increased friction from the front to the back of the defect, leading to cell accumulation at the front and eventually cell extrusion. By contrast, −1/2 defects were more static and average local flows around the defect were directed outward, thus leading to the opening of gaps within the bacteria film[101].

Other groups focused their research on the effect of topological defects on mammal cellular epithelia[108,109,110,111]. For example, Saw and colleagues studied apoptotic cell extrusion in MDCK (Madin Darby canine kidney) epithelia and showed that this phenomenon is caused by

aberrations in cell alignments in the form of comet-shaped topological defects (+1/2) (figure 1.10). Interestingly, they also found a universal correlation between nematic defects locations in cell orientation field and extrusion sites in various monolayer types[112].

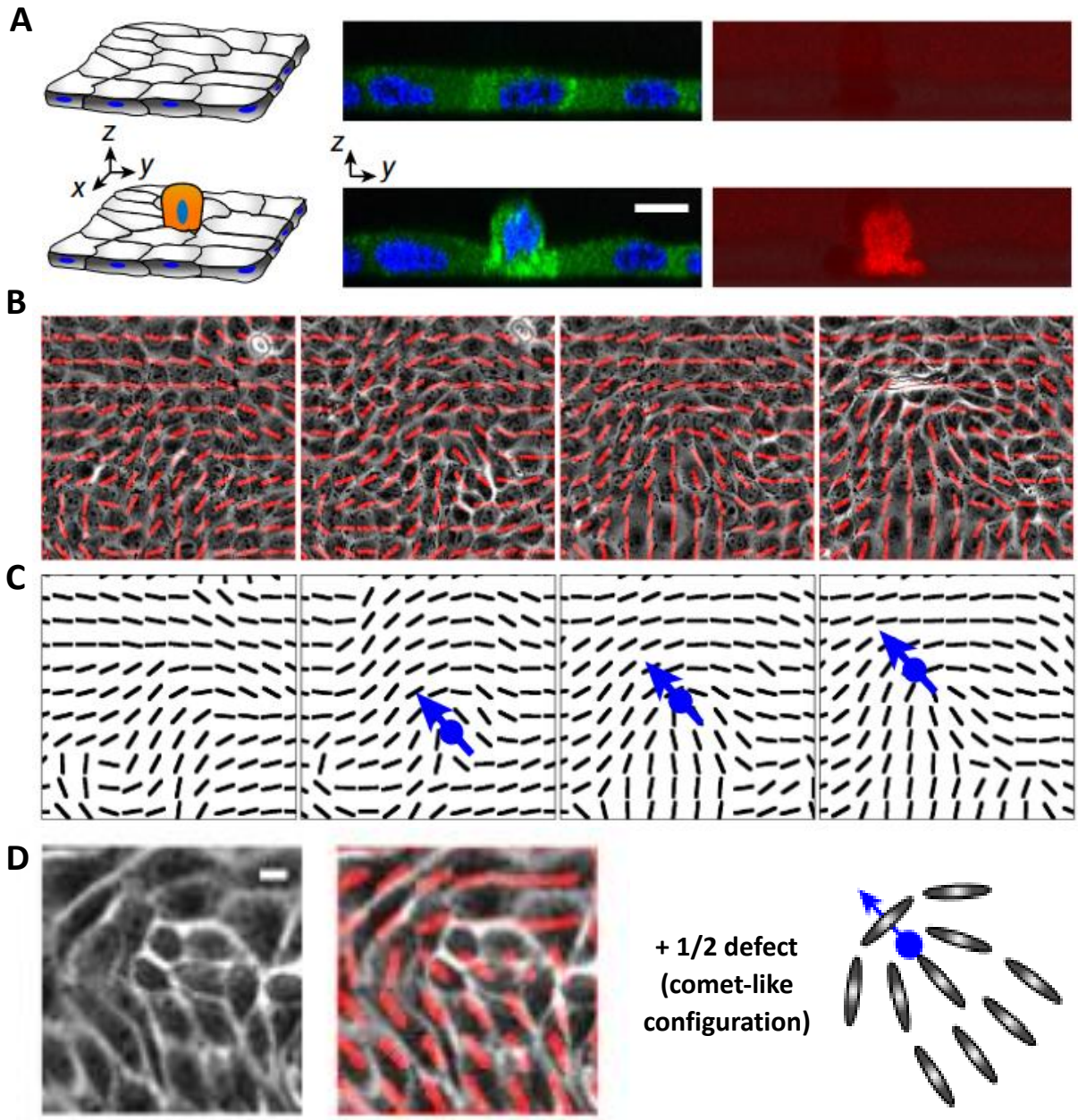


***Figure 1.10.*** *(A) Left, diagrams of confluent monolayer and extruding cell. Middle, side view of confluent MDCK monolayer and extruding cell. Green, actin; blue, nuclei. Right, corresponding images of caspase-3 signal. (B) and (C) Corresponding images overlaid with red lines and represented as black lines (in C) showing average local orientation of cells. The cells moving towards the extrusion forms a comet-like configuration. (D) Left: zoomed-in image and orientations of cells forming a +1/2 defect, right: schema showing a +1/2 defect. Readapted from Saw et al, (2017).*

Zhang *et al.* showed that aberrations in the alignment of LP-9 cells, a human mesothelial ovarian cancer line, which occur at topological defects, are associated with altered cell density, motility and forces. They indeed identified several topological abnormalities in the mesothelial layer and showed how they affected local cell density by generating a net flow of cells directed inward or outward, depending on the defect type[113].

Moreover, Guillamat and colleagues have recently showed that self-organization of C2C12 murine myoblasts around integer topological defects, namely spirals and asters (figure 1.11.A), is enough to determine the emergence of complex multicellular architectures (figures 1.11.B and 1.11C). They have also described that these architectures could trigger localized cell differentiation or, alternatively, when differentiation is hindered, they could drive the development of swirling protrusions[102] (figure 1.11.D).

Altogether, these studies show the importance of topological defects in determining the emergence of different multiscale biological phenomena and highlight the potential of active nematic approaches to explain morphological events. Such approaches, experimental or theoretical, assume that bacteria films and cell epithelia could be seen as active nematic systems - a typology of active system characterised by self-driven units with elongated shape.

In this PhD project, we investigated the role played by topological defects in the multicellular phenomenon of budding in colorectal carcinoma epithelia. Indeed, we demonstrated that the formation of budding structures in these monolayers is associated to the presence of singularities in cell orientation and topological defects. To our knowledge, this is the first study linking this malignant multicellular phenomenon to the emergence of topological defects.

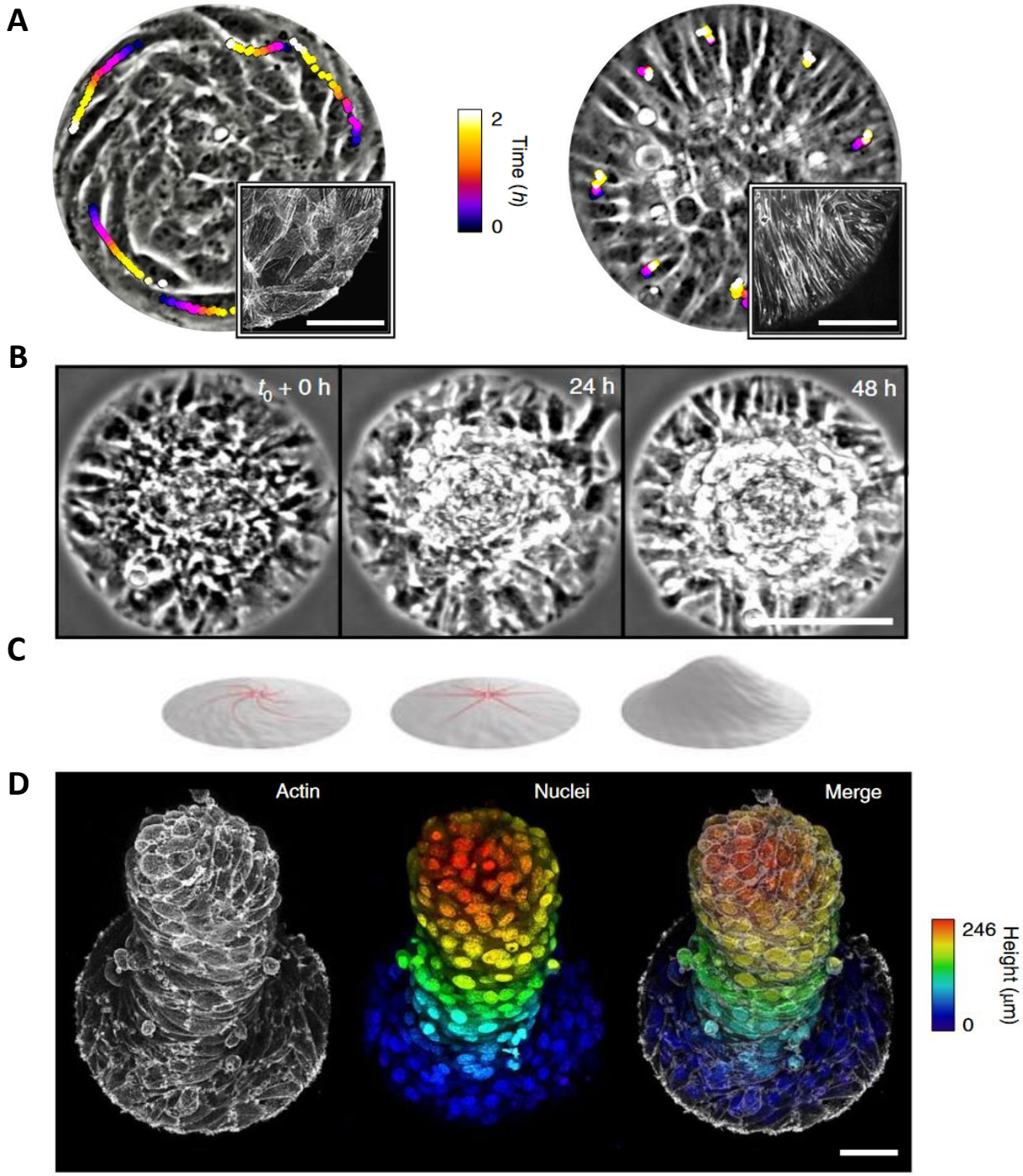


***Figure 1.11.*** *(A) Phase-contrast images of spiral (left) and aster (right) arrangements. Trajectories of cells are shown with colour gradients. Colour map represents time. Squares: confocal images of actin fibres at the base of a spiral and an aster. (B) Time series of myoblast asters forming cellular mounds. t0: confluence. (C) Schema depicting mounds at 1, 3 and 6 days after confluence. (D) Z projection of a 12-day cellular protrusion. Colour map indicates height. Readapted from Guillamat el. al, (2022).*

## 2. Objectives

In pathology and oncology, tumour budding in colorectal carcinomas is indicative of cancer progression and adverse prognosis[92], as it is associated with local recurrence, lymph node metastasis, and distant metastatic spread[87]. Therefore, understanding the biogenesis and the mechanisms leading to colorectal carcinomas budding, it is particularly relevant to make clinical advances against the metastatic spread of this typology of solid tumour. Indeed, shedding light on the metastatic cascade resulting in colorectal cancer epithelia budding, would eventually lead to the identification of new or novel therapeutic targets, aiming at tackling one or multiple steps of this process.

Budding of colorectal carcinoma epithelia was recently described as a cellular phenomenon leading to the formation of cohesive tumour spheres[65]. Such three-dimensional structures resemble the malignant lesions described by Messal and colleagues in pancreatic cancer, for their compact and roundish morphology as well as for their nature as tumour intermediate[18,65].

Messal and the other co-authors demonstrated that the process leading to the formation of these pancreatic malignant lesions is a collective morphological process in which cohesive clusters of cells collectively adopt a bulge-like phenotype[18]. We therefore formulated the working hypothesis that also budding of colorectal cancer epithelia relies on cell and tissue mechanics, occurring at supracellular level.

Dewetting of confined epithelia was described to cause the formation of a 3D spheroid-like structure in a human breast adenocarcinoma cell line, MDA-MB-231[64], and in HRAS-mutated MCF10A cells[39]. Therefore, we hypothesized that malignant dewetting of confined colorectal cancer epithelia could be considered as a budding event occurring in the whole monolayer, thus leading to the formation of just one big three-dimensional tumour sphere.

The general aim of this PhD project is to understand how supracellular cell and tissue mechanics contribute to colorectal cancer epithelia dewetting and budding. These are both malignant morphological transformations occurring on flat cancer epithelia and leading to the emergence of three-dimensional cohesive structures. The detailed research objectives are listed below:

1) Evaluation of the role of mechanical cues in neoplastic budding of colorectal cancer epithelia

We assessed the role of substrate stiffening on budding of colorectal cancer epithelia. We also evaluated the biomechanical properties of this 2D-to-3D transition in the colorectal cancer model of choice. These properties include macroscale variables such as traction forces at the cellular interface with the extracellular matrix and cellular velocities of the malignant epithelia during budding.

2) Assessment of the role of topology on colorectal carcinomas budding

Using an active nematic approach, we evaluated the role of topological defects in the emergence of budding structures in colorectal cancer epithelia. Moreover, via fabrication of micro-structured gels with grooves, we assessed the effect of forced cellular alignment on the budding process.

3) Mechanical characterization of 2D/3D malignant dewetting in colorectal cancer epithelia

We studied the biomechanical properties of malignant epithelial retraction in confined colorectal carcinoma monolayers. These properties include traction forces exerted by the cancer cells on the elastic substrates and morphological features of the malignant dewetting epithelia. We also assessed the impact of ECM density on this morphological transition.

In order to evaluate how collective cell and tissue mechanics regulate these malignant morphological transitions, we employed a multidisciplinary approach combining cellular biology techniques, such as immunofluorescence, with biophysical methods, such as traction force microscopy, micropatterning and nematic analysis.
The techniques employed are listed and detailed below in the “Materials and Methods” section.

# 3. Materials and Methods

## 3.1 Cell culture

As colorectal carcinoma models, we employed two mucus-secreting cell lines, the LS174T and the LS513 cell lines. LS174T cells were initially chosen for their ability to form spheres with inverted polarity *in vitro*, as described by Zajac *et al*[65]. However, during this PhD, we realised that LS513 cells were a better model to study the budding of small portion of epithelia, due to the higher number of buds produced. Moreover, as described later in the Results section, LS174T epithelia could form buds through the retraction of a portion of the monolayer. For these reasons, LS513 cells were used for characterising the budding phenomenon, while LS174T line was mainly employed as a model of malignant epithelial retraction.

### *3.1.1 LS513 cells*

This mucus-secreting cell line was isolated in 1985 from a 63-year-old Caucasian male patient diagnosed with a Dukes' C primary colorectal carcinoma[114]. LS513 cells were a gift from Dr. Jaulin's laboratory (Institute Gustave Roussy, Villejuif). They were grown in RPMI-1640 medium (ThermoFisher, 118750930), supplemented with 10% fetal calf serum (ThermoFisher, 10270-106) and 1% Pen-Strep (Gibco, 15140-122), at 37°C in a humidified incubator with 5% $CO_2$. Confluent cells were passaged twice a week at 1:2 or 1:3 dilution.

### *3.1.2 LS174T cells*

LS174T cell line was established in 1976 from a 58-year-old woman, having a Dukes type B adenocarcinoma of the colon[115]. This cell line was a gift from Dr. Jaulin's laboratory (Institute Gustave Roussy, Villejuif). LS174T cells were cultured in Eagle's minimum essential medium (ATCC, 30-2003), supplemented with 10% fetal calf serum and 1% Pen-Strep, at 37°C in a humidified incubator with 5% $CO_2$. Confluent cells were passaged twice a week at 1:2 or 1:3 dilution.

### *3.1.3 Infection with lentiviral particles*

In order to facilitate the visualization of TSIPs and buds, via epifluorescence or confocal microscopy, LS174T and LS513 cells were infected with lentiviral particles expressing a Puromycin-resistance cassette and LifeAct-GFP, a peptide which stains in green the filamentous actin (F-actin). The particles were obtained previously at Institute Curie in Paris,

via triple transfection of HEK-293T cells with lentiviral plasmid pLVX-EF1α-AcGFP1-N1 (Clontech, 631983), packaging plasmid psPAX2 (Addgene, 12260) and VSV-G envelope expressing plasmid pMD2.G (Addgene, 12259)[98]. The day before the lentiviral infection, 500.000 cells were plate in a plastic p6 dish and let grow for 18-20 hours. The day after, the infection mix was prepared diluting the lentiviral particles 1:20 in pre-warmed complete medium and adding Polybrene (Merck Millipore, TR-1003-G), at a final concentration of 8 µg/mL. Polybrene is a cationic polymer that increases retroviral and lentiviral gene transfer efficiency by enhancing receptor-independent virus adsorption on target cell membranes. After removal of old media, the infection mix was poured drop by drop on the cells, until completely covering the well surface. Cells were incubated at 37°C for 1 hour and subsequently centrifuged at 1000 rpm for 1 hour. The dish was then placed back at 37°C and cells were incubated 24 hours. The day after, the infection medium was removed, cells were washed with PBS, split 1:3 and let grow for at least 24 hours. LS174T and LS513 cells were then selected for 3 days in complete growth medium containing respectively 4 µg/mL or 5 µg/mL Puromycin (Quimigen, SC-108071). Indeed, the lentiviral vector contains a Puromycin-resistance cassette, so the positive infected cells should be resistant to this antibiotic, while the not infected should die. The fluorescence of the selected cells was then checked using epifluorescence or confocal microscope.

*3.1.4 TSIPs counting*

The release of tumour spheres with inverted polarity from confluent LS174T or LS513 epithelia is often hindered by the presence of mucin secreted by these cell lines. Therefore, for facilitating the detachment of the spheres from the monolayer and to be able to count them, culture dishes or flasks were vigorously shaken manually 3 times. This simple method is named "mitotic shake-off" and it is commonly employed to synchronize cells. Indeed, it is used to select mitotic cells which are rounder and less firmly attached than the rest of the monolayer, so they could be released by shaking the dish or hitting it gently on the working bench. In our case, we did the same to enhance the release of TSIPs from the cell monolayer. After the mitotic shaking, the medium was transferred to a falcon and centrifuge it 1 minute at 1500 rpm, in order to precipitate the TSIPs. The pellet was then resuspended in 200 µl of fresh medium and the resulting solution was placed on a glass coverslip or in a plastic well. TISPs were then counted at a 10X magnification, using an inverted microscope.

*3.1.5 Drug treatments*

LS513 cells were treated with SCH772984 (MCE, HY-50846) or Trametinib (MCE, HY-10999), in order to inhibit the MAPK pathway and to evaluate if this inhibition could have any effect on bud production. SCH772984 is a highly selective inhibitor of ERK1 and ERK2 phosphorylation, with antitumor activity in cells containing BRAF or RAS mutations[116]. Trametinib is an inhibitor of MEK1 and MEK2, the kinases that phosphorylate and activate ERK1 and ERK2[117]. Cells were allowed to reach at least 80-90% confluency, before being treated with MAPK pathway inhibitors. SCH772984 and Trametinib were diluted in cell media at a final concentration of 5 µM and 0.1 µM, respectively. As vehicle control, DMSO was added to control wells at a final concentration of 1:2000. Cells were treated for up to 3 days and medium was changed daily to prevent accumulation of dead cells aggregates.

**3.2. Fabrication of Polyacrylamide substrates with tuneable stiffness**

Polyacrylamide gels (PAA) having different Young's moduli were used as elastic substrates to culture LS174T or LS513 cells. PAA gels were prepared through chemical polymerization, initiated by TEMED and APS (figure 3.1 A). To tune hydrogel stiffness, the concentrations of reagents used were varied (see Table 3.1). In this thesis project, two typologies of PAA substrates were fabricated: flat thin hydrogels and micro-structured hydrogels, employed to force LS513 cells alignment (figure 3.1 B).

*3.2.1 Glass-bottom dishes silanization*

Silane coupling agents are used to form a durable bond between organic and inorganic materials. In my case, silanization was employed to covalently attach polyacrylamide gels to p6 (IBL, 220.200.0200) or p12 multi-wells glass dishes (IBL, 220.210.042). For flat hydrogels, the silane solution was obtained by mixing 85.7% of absolute ethanol (VWR 1.00983.1011) with 7.15 % of PlusOne Bind-Silane (GE Healthcare, Silane A-174, 17-1330-01) and 7.15 % acetic acid (Sigma, 131008-1612). This silane solution was then poured on top of the wells (200 µL per 20 mm glass diameter) and incubated for 1 hour at room temperature under the fume hood. The solution was then aspirated, dishes were washed three times with ethanol and dried with $N_2$.

For micro-structured gels, silanization was obtained incubating glass-bottom dishes for 10 minutes with a 50%(v/v) solution of 3-(aminopropyl) trimethoxysilane (Sigma-Aldrich,

281778) in Milli-Q water. Glass well then washed with Milli-Q water for 30 minutes on an orbital shaker and subsequently incubated with a 0.5%(v/v) solution of glutaraldehyde (Sigma-Aldrich, G5882) in Milli-Q water for 30 minutes on an orbital shaker. Finally, dishes were washed three times with water and completely dried with N2.

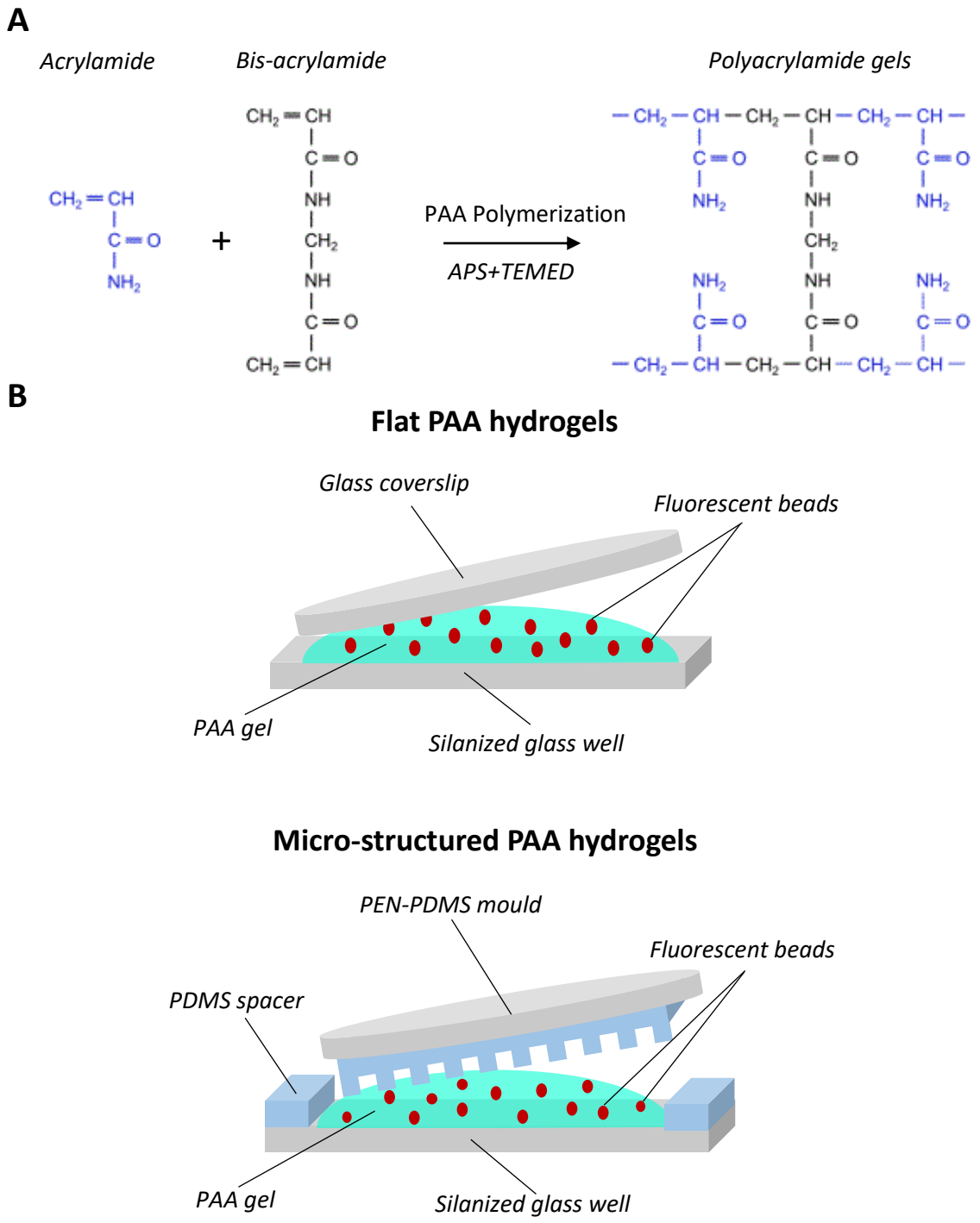


***Figure 3.1. Fabrication of Polyacrylamide substrates.*** *A) Scheme of the PAA chemical polymerization initiated by APS and TEMED. TEMED accelerates the formation of APS free radicals, converting acrylamide monomers into radicals. The radicals react with bis-acrylamide and inactivated monomers, forming the polyacrylamide hydrogel. B) Scheme of fabrication of flat and micro-structured PAA hydrogels.*

*3.2.2 Preparation of hydrogel mix*

Gels were prepared by mixing 1M HEPES (Thermo Fisher Scientific, 15630056), 40% acrylamide (Bio-Rad, 1610140), 2% bis-acrylamide (Bio-Rad, 1610142), 10% ammonium persulfate (APS, Bio-Rad, 161-0700), 1% tetramethylethylenediamine (TEMED, Sigma-Aldrich, T9281) and 200-nm-diameter dark red fluorescent carboxylate-modified beads (Thermo Fisher Scientific, F8807). The concentrations of acrylamide, bis-acrylamide and HEPES, were different depending on the desired gel stiffness. Hydrogels used in this PhD project had stiffness of 3, 12, 30 or 60 kPa in Young Modulus and were prepared as previously described[118,119,120]. The adjusted percentages are reported in the table below.

| **Stiffness (kPa)** | **3** | **12** | **30** | **60** |
|---|---|---|---|---|
| 1M HEPES | 80.55% | 71.95% | 61.25% | 60.75% |
| 40% acrylamide | 13.7% | 18.8% | 30% | 30% |
| 2% bis-acrylamide | 4.5% | 8% | 7.5% | 8% |
| Beads | 0.7% | 0.7% | 0.7% | 0.7% |
| APS | 0.5% | 0.5% | 0.5% | 0.5% |
| TEMED | 0.05% | 0.05% | 0.05% | 0.05% |

*Table 3.1. Reagents concentrations for 3, 12, 30 and 60 kpa gels*

1M HEPES, 40% acrylamide and 2% bis-acrylamide were gently mixed, avoiding the formation of air bubbles. The fluorescent beads were vortexed for approximately 10 seconds to remove any clogs or aggregates and were then added to the mix. The tube was then spun for 4-5 seconds.

*3.2.3 Fabrication of flat hydrogels*

The APS and TEMED were then added to start the polymerization; at this point, it is crucial to work quickly to avoid early polymerization of hydrogels. The solution was then vortexed for 2-3 seconds, a drop of 22 µL was added to the center of each glass-bottom well and an 18 mm coverslip (VWR, 631-0669) was added on top of it to homogenously flatten the hydrogel

(figure 3.1.B). Before use, dust and debris were removed from coverslips using $N_2$. The hydrogel solution was let polymerize for 1 hour at RT. After that, PBS was added on top of the coverslips and incubated for 20-30 minutes. Coverslips were subsequently carefully removed with the help of flat forceps, and gels were washed twice with PBS on a shaker, for at least 5 minutes. Gels were stored in PBS at 4°C until functionalization.

*3.2.4 Fabrication of micro-structured hydrogels*

Polyacrylamide (PAA) micro-structured hydrogels were prepared to force LS513 cells alignment. The experimental set-up to obtain these gels was extensively described and optimized by E. Martinez's laboratory[121] and is briefly described below.

For fabricating thin PDMS membranes of 50 µm in thickness, PDMS prepolymer, prepared at a ratio of 10:1 w/w, was spun-coated onto silicon moulds containing squared lines of 2 µm in width and 1 µm in height (figure 3.2.1). Silicon moulds were previously obtained by conventional microfabrication processes involving UV-photolithography and reactive ion etching, using silicon wafers as substrate. PDMS was then cured overnight at 65°C. After curing, PDMS membranes were cut into pieces including micro-structured as well as flat regions, which served as internal controls. The membranes were then bound to 125 µm thick polyethylene naphthalate (PEN) sheets (Goodfellow) to form flexible hybrid PEN–PDMS moulds. In parallel, custom-made reservoirs were created by using PDMS pieces with 100–150 µm thickness as spacers and binding them to silanized glass-bottom dishes (figure 3.2.2).

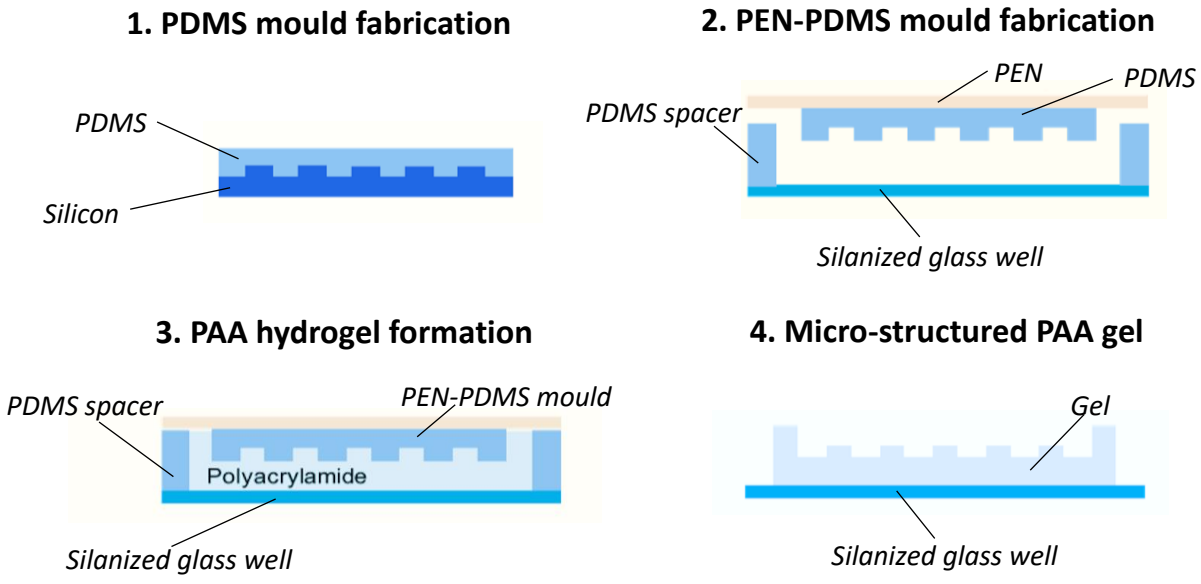


***Figure 3.2. Schematic summarising the steps of micro-structured hydrogels fabrication***

To produce micro-structured hydrogels, APS and TEMED were added to the hydrogel mix and 80 µl of this prepolymer solution were poured on each silanized well. The hybrid PEN–PDMS mould was immediately placed on top of the gel solution to let the microstructures be filled in by capillary force (figure 3.2.3). PAA hydrogels were then let polymerize for 2 hours at room temperature. The polymerized gels were de-moulded by carefully removing the flexible PEN–PDMS mould (figure 3.2.4) and then stored in PBS one day at 4°C, to achieve equilibrium swelling.

*3.2.5 Gels functionalization*

Since polyacrylamide alone does not permit cell attachment, hydrogels need to be functionalized with extracellular matrix (ECM) components. In my case, the ECM component used for the functionalization was Collagen type I, the most abundant collagen of the human body.

3.2.5.1 Hydrogels activation

To covalently bind ECM proteins to the hydrogels, sulfosuccinimidyl 6-(4-azido-2-nitrophenylamino) hexanoate (Sulfo-SANPAH) was used. This reagent acts as a bifunctional crosslinker, with a phenyl-azide group at one end attaching to PAA hydrogels after photoactivation, and an ester group at the other end covalently bonding the primary amines of proteins. Hydrogels were functionalized with a solution obtained diluting 25 mg $ml^{-1}$ Sulfo-SANPAH, (Thermo Fisher Scientific, 22589) in MilliQ water, at a final concentration of 1 mg $ml^{-1}$. PBS was removed from hydrogels and 150 µL of 1 mg $ml^{-1}$ Sulfo-SANPAH were added to each gel. The glass-bottom dishes were then exposed under UV light using a lamp (XX-15, UVP) for 5 minutes at 365 nm wavelength, at 5 cm of distance. Hydrogels were subsequently washed twice with PBS for at least 5 minutes, in order to remove any residue of Sulfo-SANPAH. Two typologies of ECM coating were performed: a homogeneous Collagen I coating, used to obtain confluent epithelia, and a discontinuous one, employed to obtain selective cell attachment (figure 3.3).

3.2.5.2 Homogeneous Collagen I coating

In a cell culture hood, PBS was removed and gels were washed twice with sterile PBS. The hydrogels were then dried at room temperature, under the hood for at least 20 minutes. In

the meanwhile, collagen type I (First Link, 60-30-810) solution was prepared on ice; for all the experiments with LS513 cells, Collagen I was diluted in sterile PBS at a final concentration of 100 µg/mL, while for LS174T cells various concentration were used: 100 µg/mL, 10 µg/mL and 1 µg/mL. Once the wells were completely dry, 100 µL of collagen solution were added on top of each gel. The solution was incubated at 4ºC overnight.

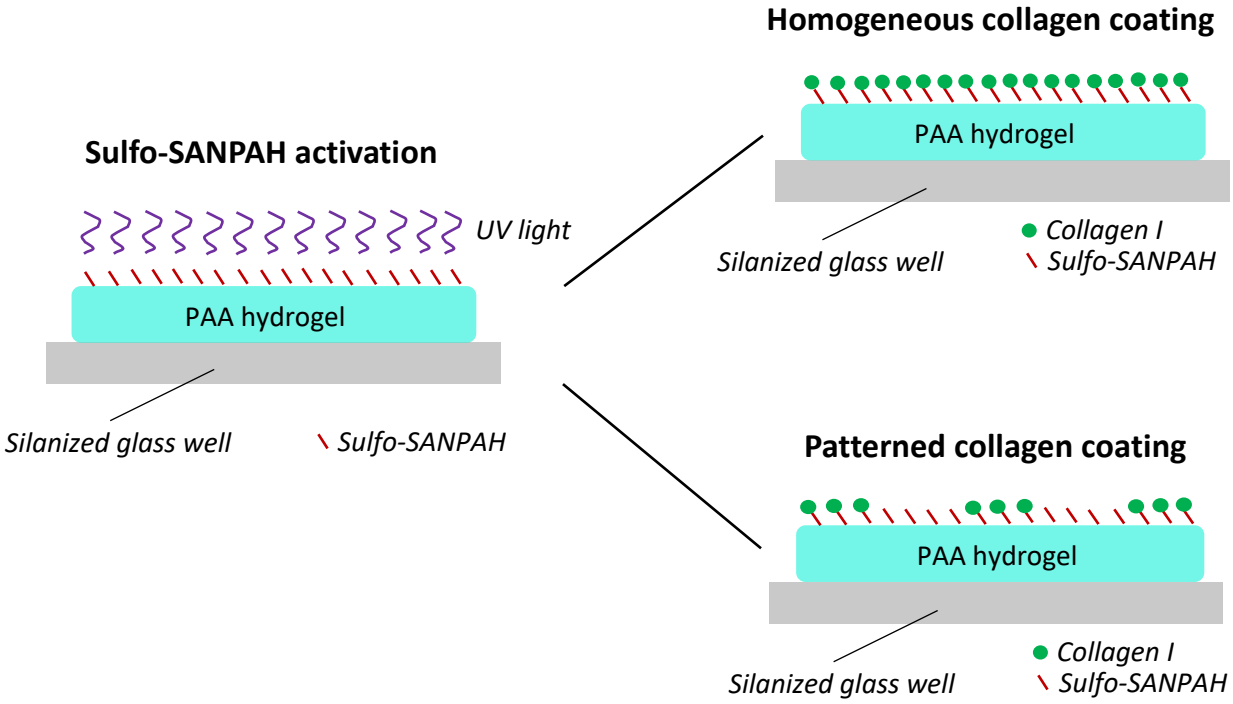


***Figure 3.3. Scheme summarising the steps of PAA hydrogels functionalization.*** *Gels were activated with Sulfo-SANPAH under UV light exposure and coated with Collagen I. Two typologies of coating were done: homogeneous collagen coating and discontinuous (patterned) collagen coating.*

3.2.5.2 Patterned Collagen I coating

This typology of discontinuous collagen I coating is employed to form cell patterns of distinct shape and dimensions and it is commonly obtained using thin PDMS stencils. The detailed steps of this procedure are described below.

a) Design of the PDMS stencils

The stencils were designed using CleWin Layout Editor software (PhoeniX Technologies, Netherlands) and were used to confine LS174T cells or LS174T_LifeAct_GFP and to normalize the shape of the cell clusters. These membranes were utilised to coat collagen on hydrogels only in correspondence of the micropatterned shapes; this results in selective cell attachment. Two distinct typologies of stencils were designed: one with circles of 400 µm

fixed diameter (figure 3.4.A, design 1) and one with circles having diameters ranging from 100 to 400 µm (figure 3.4.A, design 2). Different diameters were included in the same stencil to have different conditions in one gel, therefore decreasing experimental variability.

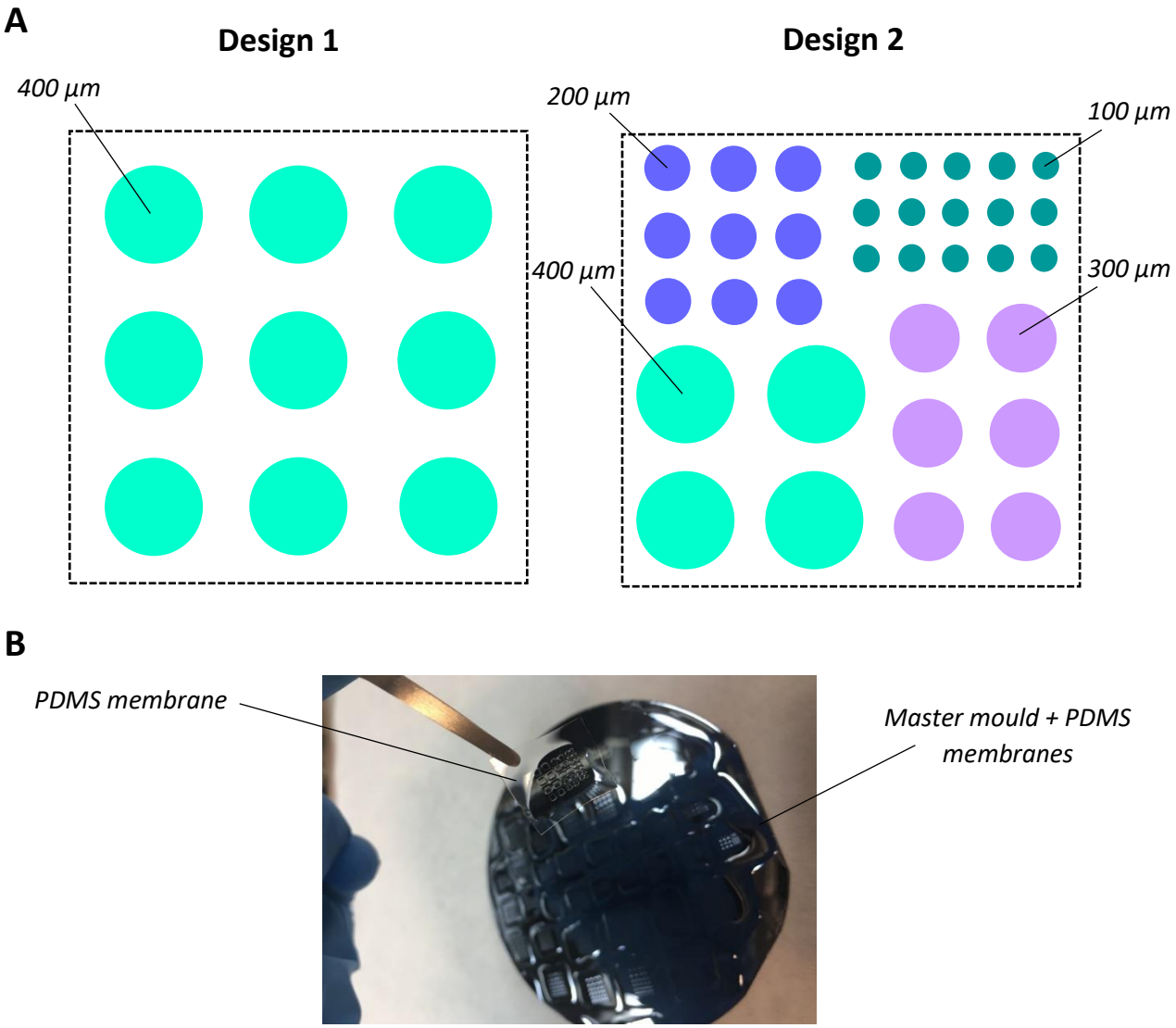


***Figure 3.4. Fabrication of PDMS stencils**. A) Schema of the two different stencils designed: the first one with 400 µm diameter circles and the second one with circles having 100, 200, 300 and 400 µm diameter. B) PDMS membrane manually peeled-off from the silicon master mould.*

b) Fabrication of master moulds

The silicon wafer was plasma-cleaned employing a HARRICK plasma cleaner (model PCD-002-CE) and desiccated for 5 minutes at >100°C on a hot plate. SU8-50 resin (MICROCHEM, Y131269) was then spun on top of the wafer using a spinner for resin (LAURELL TECH., model

WS-650MZ-23NPP/Lite). To obtain a 50 µm height, a two-steps programme was used; the parameters were the following:

1) Spin at 500 rpm for 10 seconds with acceleration of 100 rpm/second
2) Spin at 3000 rpm for 30 seconds with acceleration of 300 rpm/second

The wafer was then placed on a hot plate at 95°C for 20 min for a soft bake. Using conventional UV-photolithography (SUSS Microtec, model MJB4), SU-8 moulds were fabricated using the resin coated wafers as substrate. The wafer was then placed on a hot plate with resin side up for 1 minute at 65°C and then for 3 minutes at 95°C and let cool down on a bench. The wafer was then developed by placing it in a SU8 developer for 7 minutes and its surface was subsequently activated with the plasma cleaner. The wafer was then silanized for one hour with SILANOS desiccator, using PlusOne Bind-Silane (GE Healthcare, Silane A-174, 17-1330-01).

c) Membranes fabrication and passivation

After silanization, uncured Polydimethylsiloxane (PDMS), (Sylgard 184 Silicon Elastomer, Dow Corning) a silicon-based organic polymer, was spin- coated on top of the master moulds to a thickness lower than the SU8 features (15-20 µm) and cured at 85 °C overnight. Liquid PDMS was then poured in the spaces between the patterns for creating thicker membranes borders. Finally, PDMS stencils were manually peeled off, washed in 96% ethanol and stored at 4 °C until use (figure 3.4.B). The PDMS stencils were passivated employing a solution of 2% Pluronic acid F127 (Sigma-Aldrich, P2443) in PBS, overnight at room temperature. After that, they were washed twice in ethanol and allowed to dry for 20 minutes.

d) Collagen patterning

To obtain collagen patterns, the membranes were carefully placed on top of PAA gels, previously activated with Sulfo-SANPAH (figure 3.6.B). A solution of rat tail type I collagen was then poured on top of the PDMS openings and left at 4 °C overnight. Collagen I was diluted in sterile PBS at a final concentration of 100 µg/mL, 10 µg/mL or 1 µg/mL. The day after, the collagen solution was washed twice with sterile PBS and the PDMS stencils were carefully removed with the help of metal forceps.

### 3.3 Cell seeding on polyacrylamide substrates

#### *3.3.1 Homogeneous cell seeding on PAA hydrogels*

Collagen solution was removed from the gels and wells were washed twice with sterile PBS. The hydrogels were then completely dried on the edge of the cell culture cabinet; the absence of any remaining liquid is fundamental to avoid the spreading of the cell suspension outside the gel area. Once the gels were completely dry, 50 µL of pre-warmed cell culture media were added on top of each gel and incubated for at least 20 minutes inside the cell culture cabinet. In the meanwhile, LS174 or LS513 cells were washed once with PBS, trypsinized, centrifuged at 1000 rpm and counted. Cells were then resuspended in fresh medium at a final concentration of $2x10^6$ cells/mL and 50 µL of this solution were placed on top of the media droplet. Cells were then incubated for 1 hour at 37 °C for attachment; the non-attached cells were then gently washed away with sterile PBS or cell culture medium. Culture medium was then added to each well and cells were stored at 37°C in a humidified incubator with 5% $CO_2$ until imaging. Before imaging, cells were washed with sterile PBS and the old medium replaced with fresh one supplemented with 10% fetal calf serum and 1% Pen-Strep.

#### *3.3.2 Cell patterning on PAA hydrogels*

After removal of the PDMS stencils, gels were passivated with PLL-g-PEG (PLL(20)-g[3.5]-PEG(2), SUSOS AG), to avoid unspecific cell attachment in the space between neighbour circular patterns. PBS was removed from the wells and 200 µl of PLL-g-PEG solution (0.1 mg/ml in PBS) were added on top of each gel for 30 minutes at RT. After that, PAA gels were washed twice with sterile PBS to remove any residual PLL-g-PEG solution. For cell seeding, the PBS was removed, and the gels were left to dry for 30-40 minutes. 50 µL of pre-warmed cell culture media were then added on top of the hydrogels and incubated for approximately 20 minutes under the cell culture cabinet. In the meantime, LS174 cells were washed with sterile PBS, trypsinized, centrifuged at 1000 rpm and counted. Cells were then resuspended in fresh medium at a final concentration of $2x10^6$ cells/mL and 50 µL of this solution were placed on top of the medium droplet. After one hour, the unattached cells were washed away, and fresh medium was added. Cells were allowed to spread for at least 24 hours before starting the imaging on the patterns (figure 3.5.A).

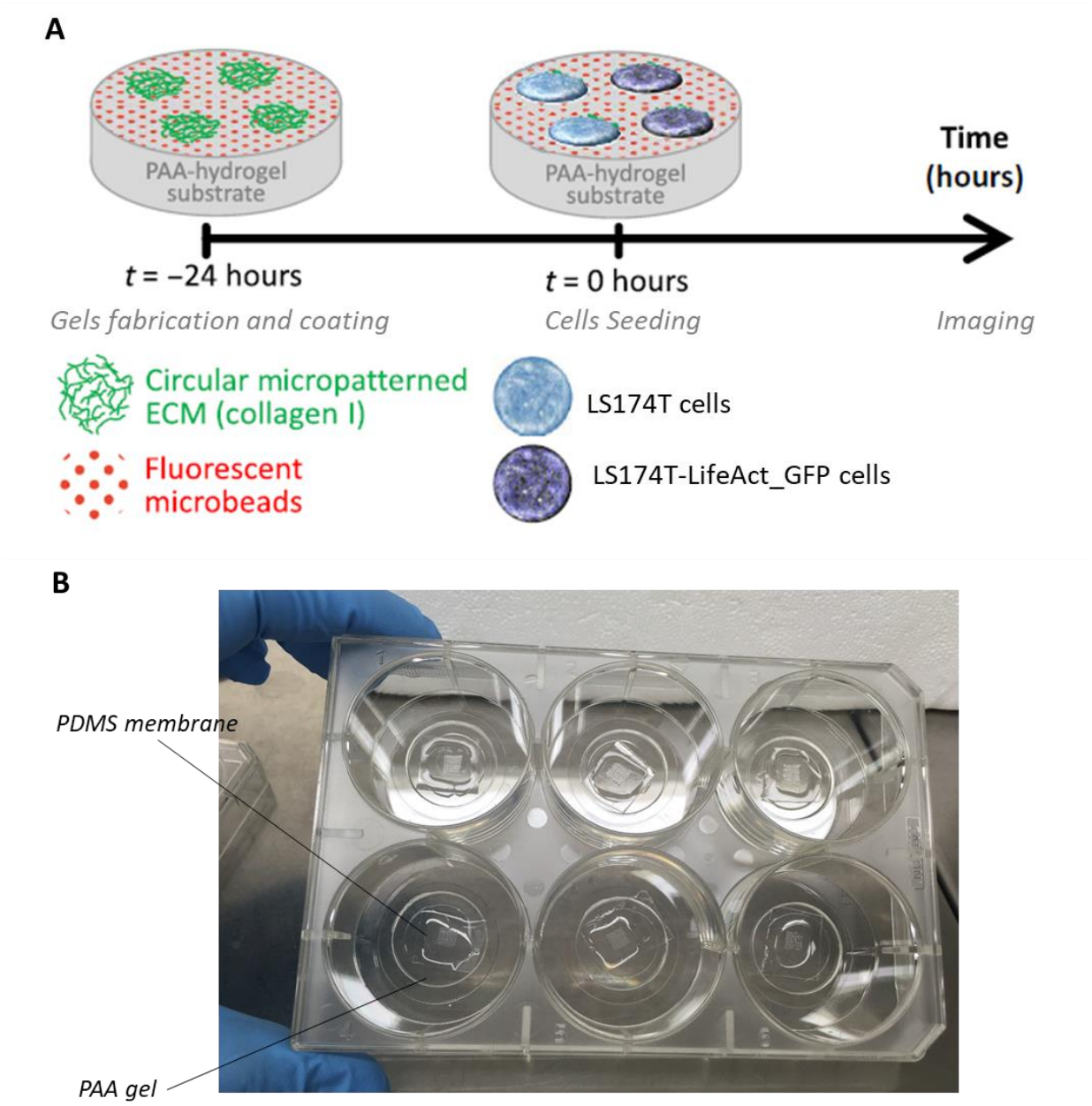


***Figure 3.5. Cell patterning on PAA hydrogels****. A) Schema depicting the different steps of cell patterning experiment: flat gels fabrication and Collagen coating, LS174 or LS174T_LifeAct_GFP cells seeding and imaging. Readapted from Nyga et al., (2021). B) PDMS membranes placed on top of pre-functionalised PAA gels.*

### 3.4 Time-lapse microscopy

Multidimensional acquisitions were performed on an automatic inverted microscope (Nikon Eclipse Ti) using a 20x objective (Nikon CFI Plan Apo 20X/0.75 Ph DM) and a virtual zoom of 1x or 1.5x. The microscope is equipped with perfect focus system and active control of temperature, $CO_2$ and humidity, to permit long live time-lapse imaging. Phase contrast and beads images were obtained every 15 minutes, for approximately 3 days. Up to 40 regions of

interest could be imaged in parallel using a motorized *XY* stage. ImageJ and NIS software were then employed to reconstitute the multidimensional acquisitions.

### 3.5 Immunofluorescence

Cells were washed with PBS, fixed with 4% paraformaldehyde (PFA) for 10 minutes at room temperature and washed twice with PBS. After washing, samples were blocked and permeabilized in PBS supplemented with 1% bovine serum albumin (BSA, Sigma, A7906) and 0.3% Triton-X-100 (Sigma, T8787) for 1 hour at room temperature. Samples were then incubated with primary antibodies diluted in blocking buffer, 4°C overnight. The primary antibodies used were mouse anti-E-cadherin monoclonal antibody (BD Biosciences, 610181), mouse anti-ezrin monoclonal antibody (BD Biosciences, 610602), rabbit anti-K-Ras polyclonal antibody (Abcam, ab180772) and anti-Phospho-ERK1/ERK2 rabbit monoclonal antibody (ThermoFisher, 700012). They were used at a dilution of 1:1500, 1:500, 1:100 and 1:100 respectively. For focal adhesion staining, an anti-Vinculin antibody was used (Merck, MAB3574), at a final concentration of 1:100. Samples were then washed 3 times with washing buffer [PBS supplemented with 0.05% Tween-20 (Sigma, P9416)] and incubated with the appropriate secondary antibody for 2 hours at room temperature. The secondary antibodies were Alexa Fluor 488 anti-mouse (Jackson Immuno Research, 715-165-151), Cy3 anti-mouse (Jackson Immuno Research, 715-165-151) and Alexa Fluor 488 anti-rabbit (ThermoFisher, A21206). They were all diluted in PBS at a final concentration of 1:1000. Samples were subsequently rinsed 3 times with washing buffer and F-actin was labelled by incubating for 30 minutes at room temperature with Phalloidin-iFluor594 cytoPainter (Abcam, ab176757), diluted 1:3000 in PBS. After other 3 rounds of rinsing with washing buffer, samples were mounted with 1-2 droplets of Fluoroshield mounting medium with 4’,6-diamidino-2-phenylindole (DAPI) (Sigma-Aldrich, F6057) and stored at 4°C until imaging.
Confocal images were taken on inverted confocal microscope Axio Observer 7 (Spectral Detection Zeiss LSM 800), using 20×/0.8 M27, 40×/1.3 Oil DIC M27 or 63×/1.4 Oil DIC M27 objectives with ZEN 2.3 imaging software.

### 3.6 KRAS and pERK quantification

To assess if KRAS was more expressed in budding areas with respect to flat non-budding areas, LS513 cells were stained with anti-KRAS antibody and imaged at the Confocal microscopy, as

described previously. Later, using the ImageJ selection option, the borders of budding regions were manually drawn to exclude the regions outside this border. For assessing KRAS expression in non-budding areas, flat regions with roughly the same surface of the budding ones were manually selected. ImageJ software was then employed to compare the mean fluorescence intensity of budding and non-budding regions.

The expression of phosphorylated forms of endogenous ERK1 and ERK2 proteins (pERK1/ERK2) was assessed via staining with anti-Phospho-ERK1/ERK2 antibody, as described before. Since the active forms of pERK are known to translocate in the cell nucleus, we measured the ratio between nuclear pERK with respect to the total, in budding and non-budding areas. As for the quantification of KRAS, budding regions and non-budding regions were manually selected on ImageJ. Later, the nuclei were selected manually, employing the DAPI signal for identification. The mean intensity of pERK1/2 was then measured for cell nuclei and for the total, in both budding and non-budding areas.

### 3.7 Focal adhesions quantification

The focal adhesions were quantified via Vinculin staining in budding and non-budding portions of the monolayer. Confocal images were treated to obtain a binary mask where the area occupied by Vinculin appears in white, while the focal adhesions-free regions appeared in black. Examples of the resulting treated images are shown in figure 3.6.

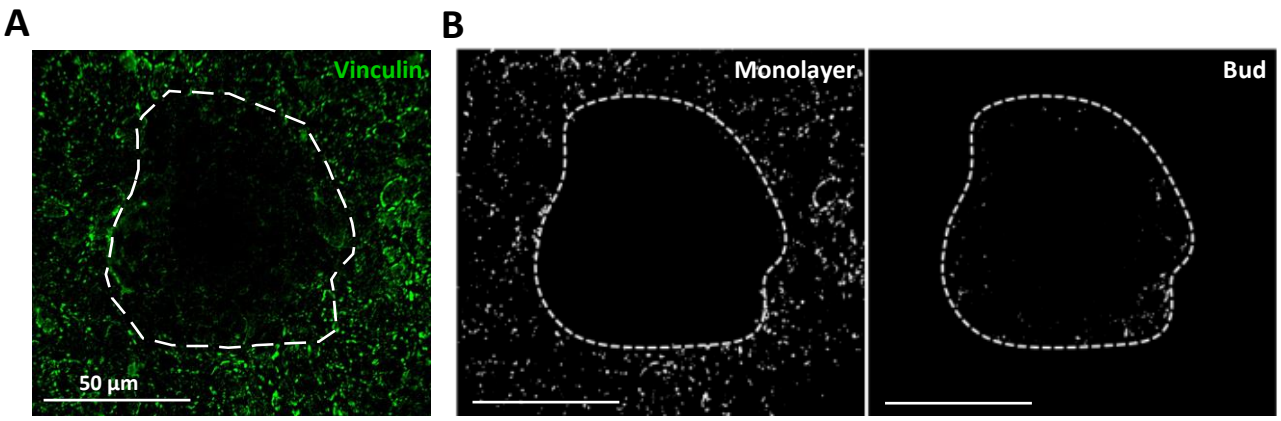


***Figure 3.6. Focal adhesion quantification.*** *(A) Confocal microscopy image of representative max-projection of basal z-stacks, showing LS513 cells stained for Vinculin. The white dotted area frames a budding region. (B) Binary masks resulting from the pipeline explained in section 3.7. and displaying focal adhesions in budding vs surrounding normal monolayer. The dotted lines delimit the budding area. Scale bars: 50 µm.*

The pipeline used was the following:

- Maximum intensity projection of the basal z-stacks to be analysed
- Subtract background with rolling ball radius of 20 µm
- Gaussian blur filter with radius of 0.3 µm
- Classic Watershed with minimum grayscale value at 0.5 and maximum at 255 pixels
- Analyse particles having circularity between 0.1 and 1 and surface between 0.25 and 10 $\mu m^2$

We then quantified the density of focal adhesions (/$\mu m^2$) for budding and non-budding areas.

**3.8 Buds Counting**

In order to study the effect of substrate stiffness and cell alignment on buds' formation, I quantified the number of buds produced by LS513 cells cultured on PAA gels with different elasticity and topology. To do so, I imaged the whole monolayer, using a function of Nikon Eclipse Ti microscope called 'Wide field image', where a single central region of interest (1608x1608 pixels), imaged in my case with 20x objective, is repeated in vertical and in horizontal N times. To obtain pictures of the full epithelia, the 1608x1608 pixels ROI was repeated on average 13x13 times and the resulting tiles were automatically stitched together, to form a single seamless picture of around 21000x21000 pixels. Employing the NIS software, the exact area of the epithelia was calculated, manually drawing the contour of the monolayer, and excluding the regions outside this border. To be able to distinguish buds from cell aggregates, counts were done using phase contrast images as well as DAPI, Phalloidin and Ezrin stainings of the same region. In this way, only the 3D structures presenting the typical buds' morphology (Nuclei juxtaposition, absence of lumen and actin-ezrin crown) were counted, while cell aggregates were excluded. Due to the high variability of epithelia surface in the different conditions analysed, the number of buds was normalized for an area of 100 $mm^2$.

**3.9 Image processing for traction force microscopy, nematic and velocity analysis.**

Time-lapses images of beads and cells were aligned with a custom-made Matlab code (Appendix, code 8.2.1), in order to remove any microscope vibrations or stage movements

that could affect further quantification steps. Image borders were subsequently removed by employing an image cropping custom-code.

Confocal or phase contrast images used for nematic analysis, were processed on ImageJ with a combination of filters chosen to properly visualize cells boundaries. Phase contrast images, previously aligned and trimmed, were processed employing a custom-made Macro in ImageJ (Appendix, 8.2.2). The pipeline used was the following:

- Images were sharpened using Sharpen filter
- Images were processed with Bandpass filter (upper limit= 22 µm, lower limit= 1.6 µm)
- Images were sharpened using Sharpen filter twice

For Confocal images, E-cadherin or Phalloidin pictures were processed as following:

- Images were processed with Bandpass filter (upper limit= 22 µm, lower limit= 2.7 µm)
- Images were sharpened using Sharpen filter

**3.10 Nematic analysis**

*3.10.1 Obtaining topological defects from the cell elongation nematic field*

Processed images were analysed with the OrientationJ plugin of ImageJ (GitHub - Biomedical-Imaging-Group/OrientationJ) to quantify local spatial orientation that reflects the underlying cell elongation. Cell orientations of phase contrast images were calculated for two different scopes: for visualization, namely for creating images or videos with cell orientation plotted on pre-processed pictures, and for further analysis about topological defects. OrientationJ parameters were chosen in order to roughly obtain a vector/cell and to ensure that the most robust defects were observed (figure 3.7). Images were processed employing a custom-made Macro (Appendix, code 8.2.2) with the following parameters:

- Tensor of the vector field: 6.6 µm
- Vector grid: 8.8 µm
- Vector scale: 80%

The tensor of the vector field corresponds to the interrogation window used for the analysis. For confocal microscopy pictures, local spatial orientations were plotted on pre-processed Phalloidin or E-cadherin images of LS513 cells. The parameters used were the followings:

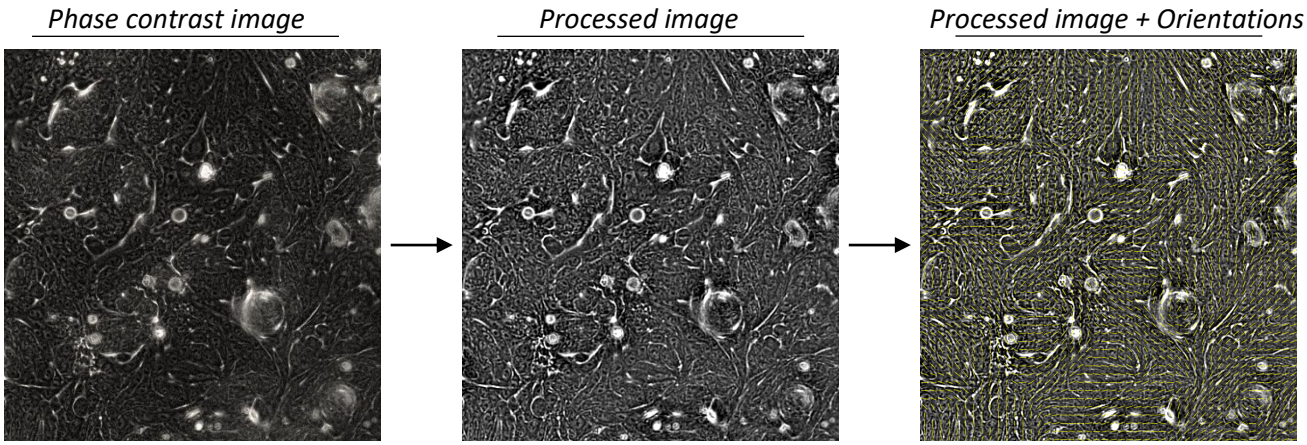


***Figure 3.7. Image processing and nematic analysis.*** *Representative phase contrast image processed to visualize cells boundaries and analysed with Orientation J plugin, to quantify local spatial orientation. Orientations (yellow vectors) are plotted on the pre-processed image.*

- Tensor of the vector field (interrogation window): 4 µm
- Vector grid: 4 µm
- Vector scale: 80%

Starting from cell orientations calculated with OrientationJ plugin and using a customized code in Matlab, we plotted +1/2 and -1/2 defects on phase contrast or confocal images. The code was written by Dr. Gontran and Dr. Imandar, with contributions from Dr. Conte and G.Fornabaio (Compute-TopoDefects/ComputeTopologicalDefects_220829.Emilie103-G/Compute-TopoDefects (github.com)).

The OrientationJ plugin provided the dominant direction of the structure tensor at each point, which represents the local orientation field for cell elongation. The orientation field measured was used to quantify the spatiotemporal evolution of ±1/2 topological defects, that were obtained by calculating the winding number for each unit of the underlying grid[109]. The winding number of a closed curve around a given point is an index representing the total number of times that the curve travels counter-clockwise around the point. This number depends on the orientation of the curve, and it is negative if the curve travels around the point clockwise, positive otherwise.

The ImageJ plugin also provided the coherence (C) of the structure tensor that is employed to measure the strength of cell orientation. C can have a value between 0 and 1, where 1 corresponds to the highest cellular elongation possible. The local smoothing window used to

obtain the structure tensor, which roughly corresponded to a cell, ensured that the most robust defects were observed.

*3.10.2 Heat-maps of Topological defect charge with respect to bud locations*

Due to fact that both the -1/2 and +1/2 defects found on LS513 epithelia with this analysis were highly motile and highly fluctuating in time, defects were not plotted individually, but they were overlapped in time. In this way it was possible to exclude the most fluctuating defects and to identify the presence of peculiar patterns that were persistent throughout the experiment.

For every time frame $t$, we obtained the location of the -1/2 and +1/2 defects over the tissue grid. Simultaneously, we also back-tracked in time the future buds to obtain the size and location $(x_t, y_t)$ of the bulging structures for all times $t$ until the bud clearly emerges at $t = t_{em}$. The centroid coordinates of buds were obtained for each time-point by manual tracking in ImageJ or Matlab. The mean position of the bud over the entire duration was calculated as reported in [1]:

$$\overline{x} = \frac{1}{t_{em}} \sum_{t=0}^{t_{em}} x_t \text{ and } \overline{y} = \frac{1}{t_{em}} \sum_{t=0}^{t_{em}} y_t. \quad [1]$$

To quantify the defect charge of the nematic field with respect to the bud location, we first plotted a heat map of the location of the -1/2 and +1/2 defects that is combined over time. To do that, we extracted a rectangular window of width $w$ and height $h$ with the mean bud location $(\overline{x}, \overline{y})$ at the centre. This rectangular region was then divided into smaller square bins with spatial index $(i, j)$ of size $\Delta x = \Delta y = 32px$. The total number of -1/2 and +1/2 defects within each of the bins $(i, j)$ over the entire duration $t_{em}$ was initially obtained individually for negative or positive defects. Finally, a spatial heat-map of the total charge, normalized over time, of the -1/2 and +1/2 was generated. This combined plot eliminates any defect pairs that are very close to each other (within the size of grid over which the nematic field is reported), potentially due to the underlying noise in the nematic field.

*3.10.3 Space-time kymograph of topological defect charge*

The heat-maps only provide a visual depiction of the defect charge near the bud. To systematically quantify the spatiotemporal evolution of the topological defects in monolayer areas where a bud would emerge and to get rid to any spatial fluctuations observed in heatmaps, we proceeded as following. We first found the mean location of the bud $(\overline{x}, \overline{y})$, tracking the bud once fully emerged from the monolayer (red × in figure 3.8). We then drew concentric rings of thickness $\delta r$ with the mean bud location as the center. We later plotted all the defects appearing in each of these regions in the 24 hours before the emergence of a mature bud. As can be seen in the scheme in 3.8, in each of the circular/annular regions around the bud, there were several -1/2 and +1/2 defects. We finally calculated the total defect charge per unit area, for each time-points (1h). This variable, also called total strength or charge density of the region with inner radius $r$, was measured as described in [2]:

$$p(r,t) = \frac{0.5\{n^{[+1/2]}(r,t) - n^{[-1/2]}(r,t)\}}{A_r} \qquad [2]$$

where $n^{[+1/2]}(r,t)$ and $n^{[-1/2]}(r,t)$ were the total -1/2 and +1/2 defects found in the region with area $A_r$ at each hour $(t)$.

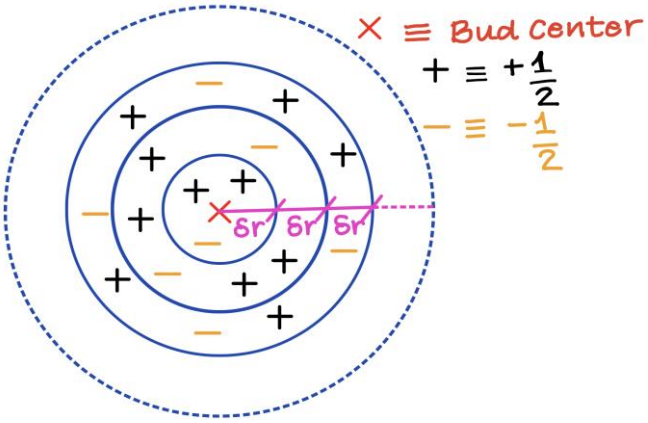


***Figure 3.8.*** *Schematic representing how the space-time kymographs of topological defect charge were done.*

The defect charge quantity $p(r,t)$ that is associated with a particular bud was then represented as a kymograph with respect to $r$ and $t$. After time averaging, spatial profiles of total charge density depict the radial evolution of topological defects arising near the bud.

### 3.11 Traction Force Microscopy

I employed this technique to measure forces exerted by the cells at the interface with the extracellular matrix, during buds' formation or monolayer retraction. The forces were quantified by measuring displacements of fluorescent beads contained within the hydrogels. Indeed, when cells exert forces on the matrix they are seeded on, they are able to displace beads from one location to another. Beads displacements between each experimental time point and a reference image obtained after cell trypsinization were computed by using a custom-made particle imaging velocimetry (PIV) code, which was developed in and provided by the laboratory of Dr.Trepat at IBEC[122]. The PIV code was used with a 32-image pixel resolution window and an overlap of 0.5. Traction forces were computed from beads displacements via a custom-made code kindly provided by Dr.Trepat, which is based on a Fourier transform algorithm for elastic hydrogel substrates having finite thickness[123]. Images for analysis were manually selected based on the quality of bead images, that had to remain in focus throughout the imaging, to avoid the detection of erroneous traction forces.

For LS174T pattern analysis, the traction field was decomposed along the normal and tangential directions to the epithelial domain's edge and the net radial and net tangential traction force components were computed as a function of time in the whole epithelial domain. To understand if different locations of the pattern could contribute in a distinct way to the overall traction forces, three subregions were defined: an internal, a middle and a peripheral (outer) domain (figure 3.9). These sub-regions were identified by using binary masks of epithelia, manually drawn for each time point following the contour of the patterns (Appendix, code 8.2.3). Each mask was divided into concentric rings one image pixel in thickness. Rings were then named through integers 1 to n moving from the rim of the pattern toward its centre. The external, middle, and internal subregions were defined by grouping adjacent rings together; the first m rings from the edge (labelled 1 to m) were merged to form the external subdomain, whereas the remaining n-m rings were combined to form the middle subregion and the inner one (the core of the disk). The m location was determined in such a

way that the three domains contained the same number of image pixels for unbiased statistical analyses over the different subdomains. The algorithm was implemented by Dr. Conte and Dr. Nyga in MATLAB for automatic execution on the individual masks of epithelia at each time point[39].

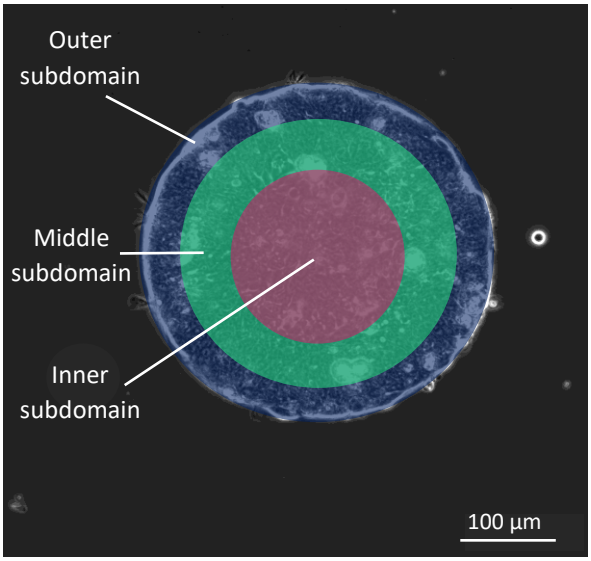


***Figure 3.9.*** *(A) Schematics representing a whole LS174T pattern divided in outer, middle and inner subdomains.*

### 3.12 Velocities analysis

To evaluate the velocities of LS513 cells grown on flat or micro-structured gels, phase contrast videos were analysed with the particle image velocimetry (PIV) software in Matlab[124] (PIVlab 2.53, PIVlab - particle image velocimetry (PIV) tool with GUI-MATLAB Central) and resulting vectors were plotted on original images. As in the case of traction force microscopy, before analysing the velocities, time-lapses images were aligned with a custom-made Matlab code (Appendix, 8.2.1), to remove any microscope vibrations or movements that could affect the detection of velocity vectors. Videos taken on flat and on micro-structured gels were analysed with the following PIV parameters:

- Algorithm used: Fast Fourier transform
- Interrogation area: 13.2 µm
- Interrogation step: 6.6 µm

Resulting velocity vectors were then post-processed using standard deviation filter with a threshold of 4.4 μm and local median filter with a threshold of 1.6 μm, to exclude noisy data from the analysis. Velocity magnitude and vorticity, a variable that measures the rotation of a fluid and is defined as the curl of the velocity, were then plotted over time for flat and grooved gels.

For the vorticity analysis of budding vs non-budding regions on flat gels, we selected as budding regions just monolayer areas in which only a single bud was arising and that were completely flat at the beginning of the imaging. To avoid interference from neighbouring buds, non-budding regions were selected among monolayer areas located at a distance ≥ 2d, where d is the average diameter of a fully formed bud.

### 3.13 Statistical analysis

Statistical analysis was performed using GraphPad Prism software (GraphPad Versions 5.01 and 9). Results are presented as mean ± standard deviation (SD) or as mean ± standard error of the mean (SEM). Statistical differences were analysed by unpaired t-test, ANOVA test (for Gaussian distribution) and Mann-Whitney or Kruskal-Wallis tests (for non-Gaussian distribution). A p-value smaller than 0.05 was considered as statistically significant: $p < 0.05$ = (*), $p < 0.01$ = (**), $p < 0.001$ = (***) and $p < 0.0001$ = (****). The number of experiments performed is specified in the text or in figure legends.

# 4. Results

## 4.1 LS513 and LS174T cell lines as *in vitro* models of colorectal carcinoma budding and epithelial retraction

First, we wanted to evaluate if the cellular models chosen could represent an *in vitro* model that retrieves the main features of CRC budding *in vivo*. As described in the introduction section, *ex vivo* samples of human primary colorectal carcinomas presented bulging structures protruding from the colon epithelium (Introduction, Figure 1.6D), and several tumour spheres completely cleaved and released into the stroma (Appendix, Figure 8.1.1A). Haematoxylin/Eosin and Ezrin staining showed that both the budding structure and the spheres were enriched in the apical marker Ezrin at their external layer (Appendix, Figures 8.1.1A-B). So, to determine the suitability of LS513 and LS174T cells as *in vitro* CRC models we assessed their ability to form bulging structures and release tumor spheres with inverted polarity (TSIPs) in suspension.

### *4.1.1 LS513 and LS174T release TISPs in vitro*

To check if LS513 and LS174T were able to produce TISPs, cells were grown for up to 2 weeks in conventional cell culture dishes and vigorously shaken to facilitate the detachment of the spheres from the monolayer (mitotic shake-off). As described in the Methodology section, this technique is commonly used to select mitotic cells which are rounder and less firmly attached than the rest of the monolayer. In this case, we did the same to enhance the release of TSIPs from cell monolayers. Upon mitotic shake-off, we collected the supernatant, counted the spheres, and assessed their polarity by ezrin immune-fluorescence staining.

Both cell lines released spheres when cultured *in vitro* (Figure 4.1.1). However, the number of spheres found in LS513 supernatants ($75.2 \pm 7.5/cm^2$) was significantly higher than the one found in LS174T ($43.4 \pm 4.3 /cm^2$). We then wanted to determine if this released spheres had indeed inverted polarity as TISPs *ex vivo*. Both LS174T and LS513 cell lines released spheres of sizes similar to the ones obtained from patients (Figure 4.1.1B-C– right – and Appendix Figure 8.1.1A). Those spheres expressed Ezrin, which was enriched in the outer part (Figure 4.1.1B-C – left). Moreover, nuclei staining showed that spheres were solid with no internal lumen (Figure 4.1.1B-C – middle). Altogether, LS174T and LS513 cells are capable of releasing spheres of apical-out polarity *in vitro* that share similarities with the ones found in peritoneal

effusions of colorectal cancer patients (Appendix, Figure 8.1.1A), namely: size, polarity and absence of internal lumen.

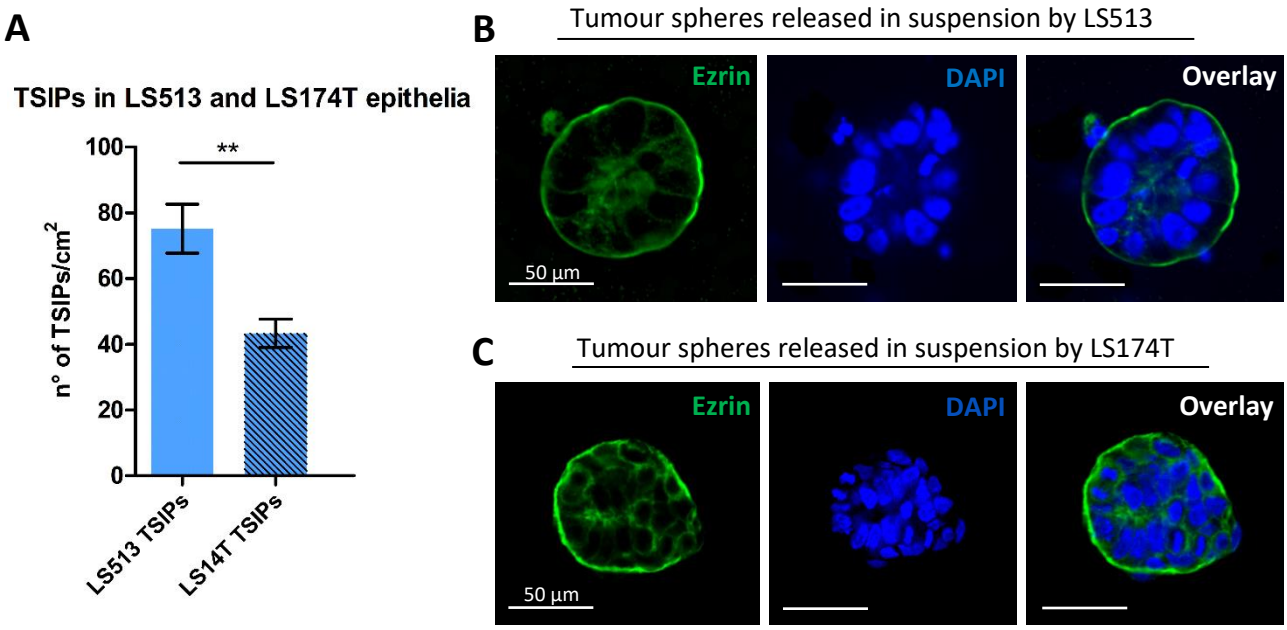


***Figure 4.1.1.*** *(A) Quantification of spheres produced by LS513 and LS174T epithelia grown on plastic. Counts were normalized for a surface of 1 cm$^2$. Results are presented as mean ± standard error of the mean (SEM). p<0.01 = (**),* t-tests. *N= 2 experiments. (B) Immunofluorescence staining of representative TSIPs released in suspension by LS513 cells grown on plastic. Nuclei are labelled in blue and Ezrin in green. Scale bars: 50 µm. (C) Immunofluorescence staining of representative TSIPs released in suspension by LS174T cells grown on plastic. Nuclei are labelled in blue and Ezrin in green. Scale bars: 50 µm.*

### *4.1.2. Budding of LS513 and LS174T epithelial cells in vitro*

After having evaluated the release of tumour spheres by these cells, we sought examples of bulging structures, termed buds, in LS513 and LS174T epithelia grown on cell culture dishes for up to two weeks. After this time, LS513 formed a monolayer where multiple bulging structures could be observed (Figure 4.1.2A). Such structures were rounded protruding cell clusters with about 50 µm of diameter (Figure 4.1.2A inset). On the contrary, LS174T cells only covered the cell culture surface partially and fewer bulging structures could be observed after two weeks of culture (Figure 4.1.2B). Despite being less numerous, buds showed a similar morphology to the ones produced by LS513 cells (Figure 4.1.2A-B, inset). Further quantification of the number of buds/cm$^2$ confirmed that indeed LS513 cells were able to bud

at least 4-times more (761.5 ± 40,2 buds/cm$^2$) than LS174T cells (180,9 ± 12,9 buds/cm$^2$) on stiff cell culture plates.

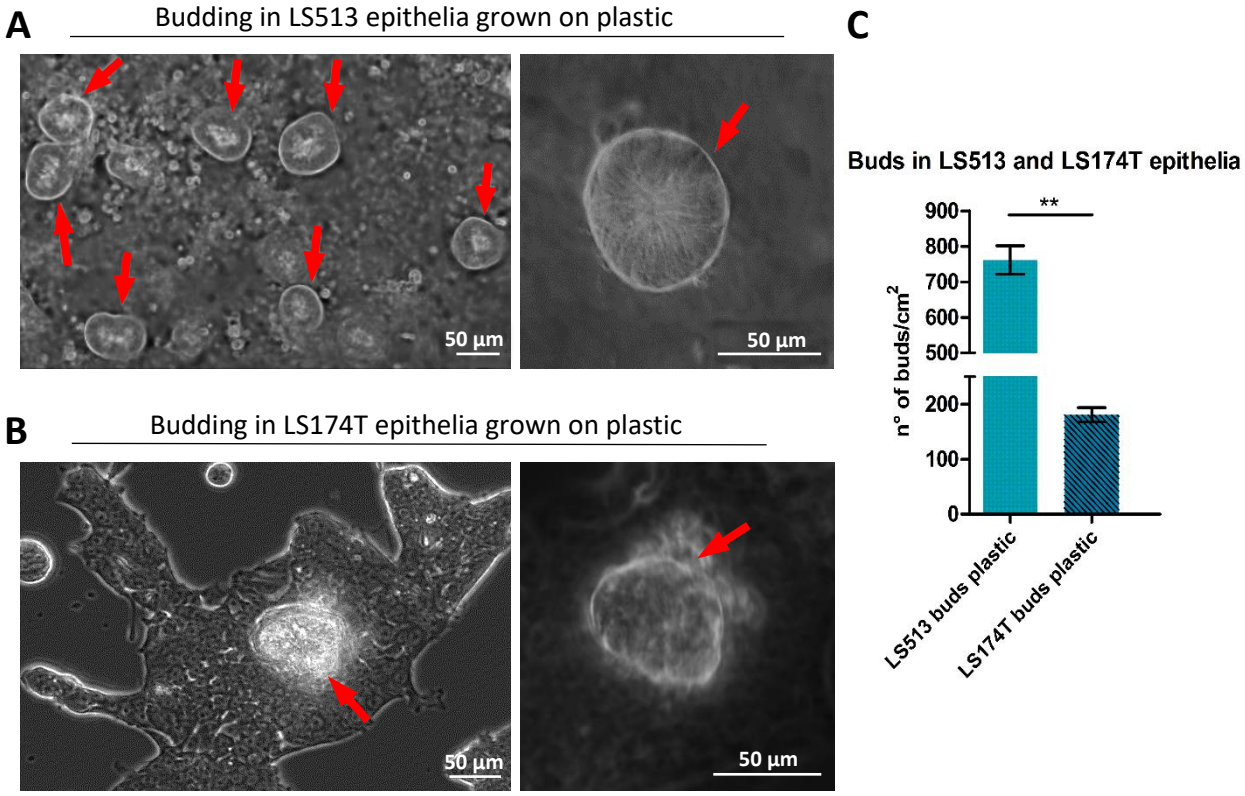


***Figure 4.1.2.*** *(A) Budding structures in LS513 epithelia grown on plastic. Upper panels: representative phase contrast image and close-up showing budding structures in a LS513 epithelium grown on plastic. Red arrows point at the buds. Scale bars: 50 µm. (B) Budding structures in LS174T epithelia grown on plastic. Upper panels: representative phase contrast image and close-up image showing budding structures on LS174T epithelium. Red arrows point at the buds. Scale bars: 50 µm. (C) Quantification of buds produced by LS513 and LS174T epithelia grown on plastic. Counts were normalized for a surface of 1 cm$^2$. Results are presented as mean ± standard error of the mean (SEM). p<0.01 = (**),* t-tests. *N= 2 experiments.*

We next assessed if the buds observed in LS513 and LS174T cells *in vitro* were similar to the ones observed *ex vivo*. To do so, we looked for the localization of polarity markers. Fluorescence immuno-staining of DAPI, actin and ezrin showed that both LS513 and LS174T buds were polarized with accumulation of ezrin and actin on the apical side (Figure 4.1.3A-B). Moreover, buds were solid cellular structures without the presence of lumen, similar to the released spheres described above (section 4.1.1).

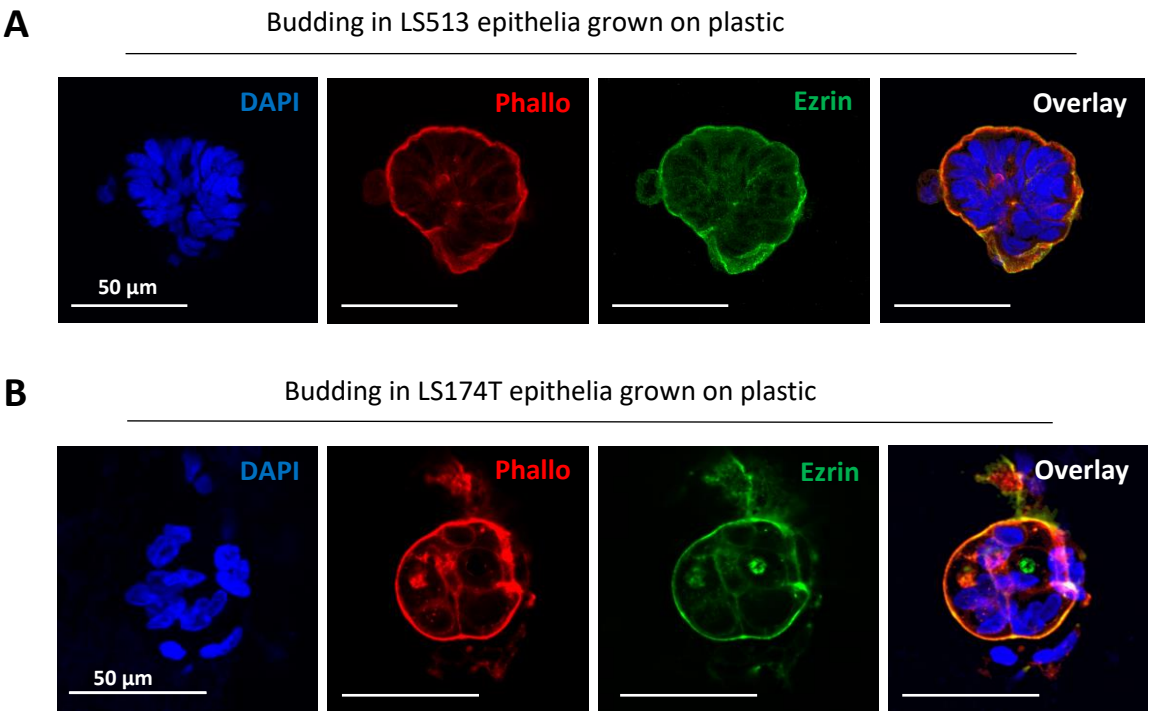


***Figure 4.1.3.*** *(A) Immuno-fluorescence staining of representative middle z-stacks showing a budding structure in LS513 monolayer grown on plastic. Nuclei are labelled in blue, Actin in red, Ezrin in green. Scale bars: 50 µm. (B) Immuno-fluorescence staining of representative middle z-stacks showing a bud in LS174T epithelium grown on plastic. Nuclei are labelled in blue, Actin in red, Ezrin in green. Scale bars: 50 µm.*

Despite both LS513 and LS174T cells were able to bud on stiff substrates, the number of buds was dramatically lower in LS174T cells than in LS513 cells. So, we wondered whether they could spontaneously produce more bulging structures if grown on soft polyacrylamide (PAA) hydrogels. These substrates better mimic the physiological properties of human tissues, with respect to stiff surfaces such as plastic or glass. The stiffness chosen for our hydrogels was 30 kPa, because such stiffness mimics the average rigidity of the colorectal tumour microenvironment, therefore being appropriate to reproduce the mechanical stimuli sensed by tumour cells[57]. Thus, we seeded LS513 and LS174T cells on collagen-coated polyacrylamide (PAA) hydrogels of 30 kPa for up to two weeks. Upon quantification of the number of buds/cm$^2$ found on 30 kPa hydrogels, we could state that (i) bulging structures were appearing in both cell lines, (ii) the number of buds was smaller than when cells were grown on stiff plastic substrates, and (iii) LS513 cells bud more (157,5 $\pm$ 13,8 buds/cm$^2$) than LS174T epithelia (49,5 $\pm$ 10,4 buds/cm$^2$) also in this condition (Figure 4.1.4A).

We were intrigued by the difference in bud number between the two cell lines, thus, to better understand the source of this variation, we decided to observe bud formation *de novo*, i.e. from a completely flat portion of the monolayer. LS513 and LS174T epithelia were imaged for up to 3 days, starting from 80-90% confluence, namely from 10-11 days of culture. By using time-lapse microscopy, we imaged the formation of bulging structures arising both from LS513 and LS174T epithelia grown on 30 kPa hydrogels (Figure 4.1.5A-B).

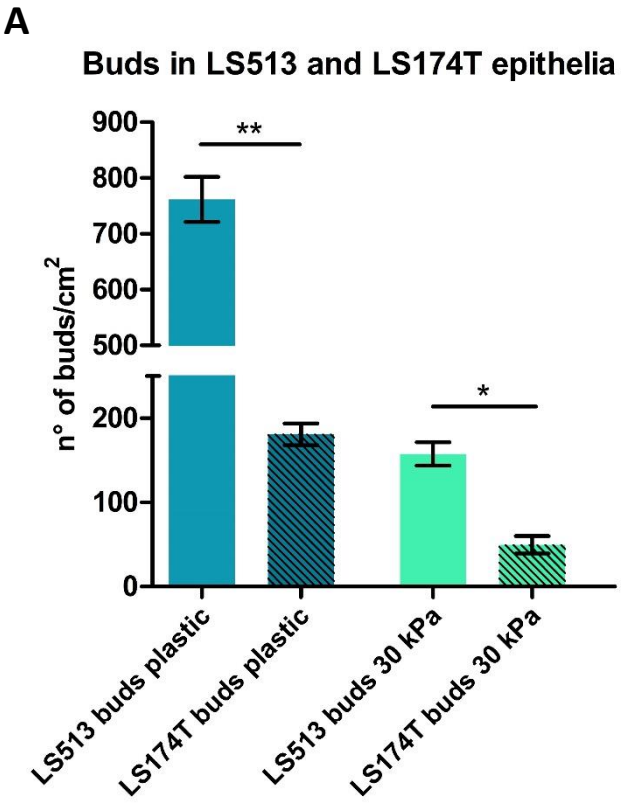


***Figure 4.1.4.*** *(A) Quantification of buds produced by LS513 and LS174T epithelia grown on plastic or on 30 kPa gels. Counts were normalized for a surface of 1 cm$^2$. Results are presented as mean ± standard error of the mean (SEM). P<0.05 = (*), p<0.01 = (**)*, t-tests. *N= 2 experiments.*

The budding process started by the 2D to 3D transition of a portion of the epithelia, showing that it corresponds to a collective phenomenon rather than the sequential aggregation of single cells.

Despite bulging structures appearing in both cell lines, striking differences could be observed between them. The phenomenon was quicker in LS513 epithelia than in LS174T monolayers. Indeed, while round and compact structures were completely developed after 16-17 hours

from the start of process in the former (Figure 4.1.5A), mature buds were only found after approximately 30 hours after onset in the latter (Figure 4.1.5B). Moreover, LS174T epithelia buds formed via retraction of a part of the monolayer (Figure 4.1.5B), while LS513 epithelia buds formed by the appearance of a protruding structure in the monolayer (Figure 4.1.5A). Specifically, in the example shown in Figure 4.1.5B the bud was forming through the retraction of a peripheric portion of the epithelium displaying a finger-like morphology.

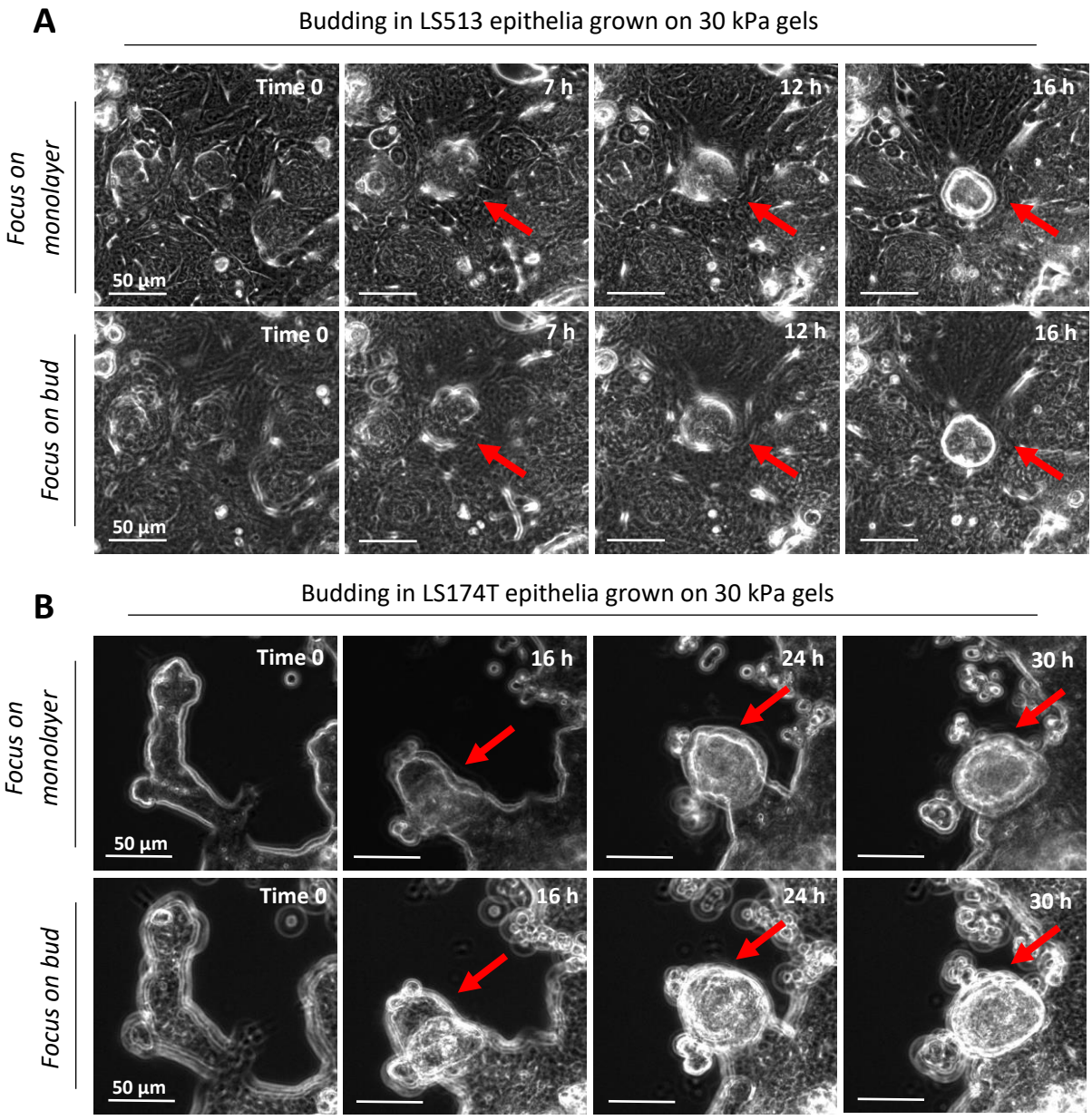

***Figure 4.1.5.*** *(A) Representative phase contrast time-lapses showing bud formation from a flat LS513 epithelium grown on 30 kPa PAA hydrogels. Red arrows point at the monolayer area in which the bud is forming. Scale bars: 50 µm. (A) Representative phase contrast time-lapses showing bud formation from a flat LS174T epithelium grown on 30 kPa PAA hydrogels. Red arrows point at the monolayer area in which the bud is forming. Scale bars: 50 µm.*

Altogether, our results show that both LS174T and LS513 cells are able to produce TSIPs and buds *in vitro* that recapitulate the main characteristics of CRC *ex vivo* buds and TSIPs[65]. However, fundamental differences were observed both in the number of buds and in the process of budding formation between the two cell lines. These differences suggest that LS513 cells might be a better *in vitro* model of CRC than LS174T cells. Moreover, LS513 cells are a good model of CRC budding *in vitro* because they display the same genetic profile of patients showing budding structures in their tumour explants. Indeed, the majority of patients developing budding display a mutation on KRAS gene that is also found in LS513 cells (Tables 8.1.1 and 8.1.2, Appendix). Conversely, KRAS expression was not found in LS174T cells[115,125].

Finally, we decided to study if the LS513 cellular model also recapitulate the Ezrin expression found in human primary colorectal carcinomas. The sample presented a bulging structure protruding from the colon epithelium showing enrichment in the apical marker Ezrin at its external layer (Figure 8.1.1B of the Appendix section). As shown in Figure 4.1.6.A, the buds found on LS513 epithelia showed the same enrichment in the apical marker Ezrin. Moreover, as shown by the Phalloidin staining in 4.1.6 A and by the intensity profiles in figure 4.1.4B, Actin shows a pattern of expression very similar to the one of Ezrin, with both enriched in the external portion of buds.

Thus, for their ability to produce more tumour spheres and buds than LS174T cells and because they recapitulate the morphological and molecular signatures of patients' buds, we chose LS513 cells as a model of colorectal cancer budding. On the other hand, since buds in LS174T cells form through retraction of a portion of monolayer, we thought that these cells could be used as a model of whole epithelial retraction (dewetting).

Therefore, next results section will focus on the mechanical characterization of colorectal cancer budding in LS513 epithelia, while the second part will focus on the study of whole monolayer retraction using LS174T cells as model.

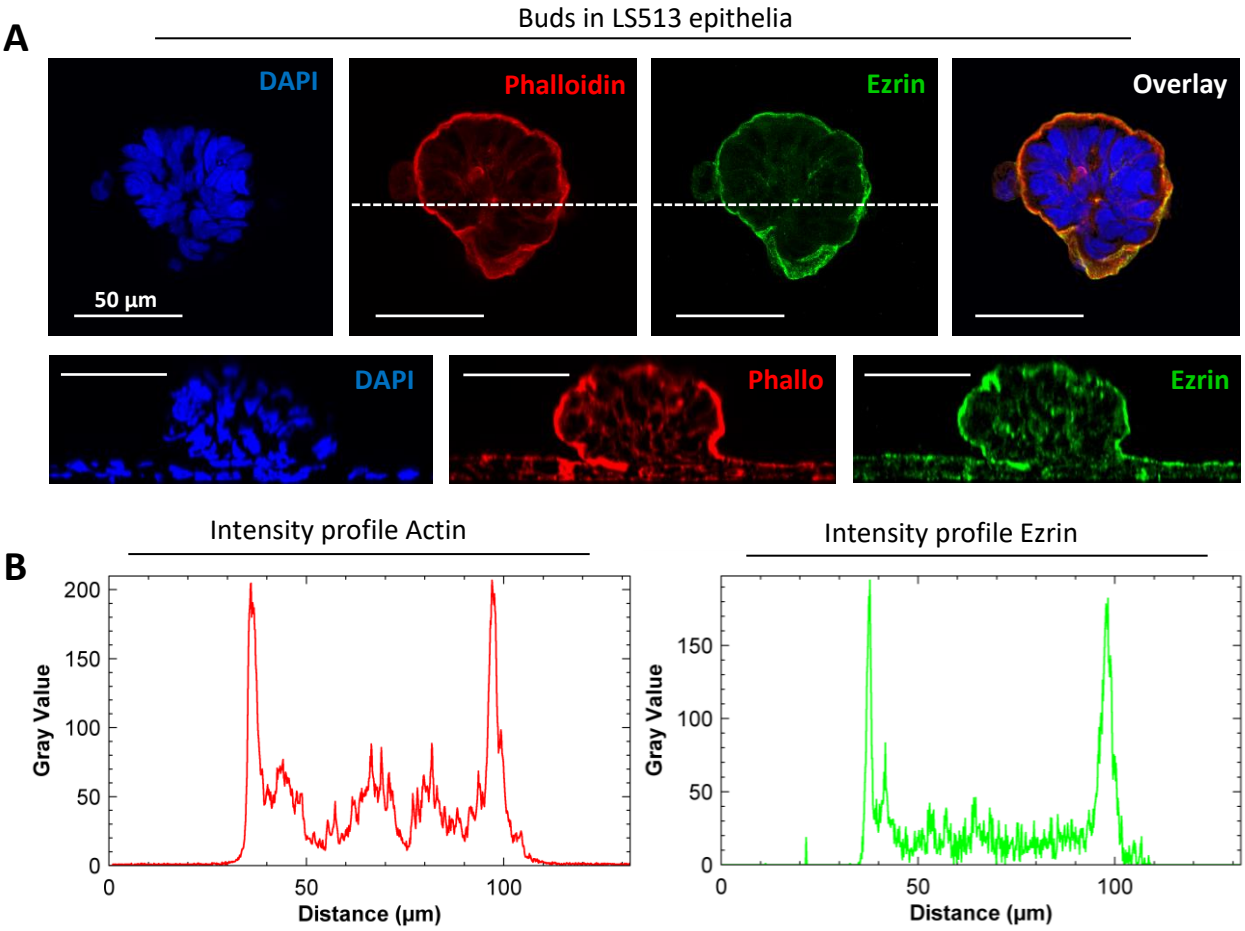


***Figure 4.1.6.*** *(A) Confocal microscopy images of representative middle z-stacks (upper row) and orthogonal cross-sections (lower row), showing a bud protruding from LS513 epithelia grown on glass. Nuclei are labelled in blue, Actin is labelled in red and Ezrin in green. Scale bars: 50 µm. N= 3 experiments. (B). Intensity profile plots for Actin and Ezrin. The graphs plot phalloidin (red) and ezrin (green) intensities along the white dashed line of the z-stacks shown in (B).*

## 4.2 Topological defects are the organizing centers for apical budding in KRAS-mutated colorectal cancer epithelia

### *4.2.1 Budding in LS513 is characterized by defined morphological steps and traction forces increase*

After having identified LS513 cells as a suitable model for studying budding of colorectal cancer epithelia *in vitro* (Results, section 4.1.2), we wondered if we could detect the distinct steps driving this process. To do so, LS513 cells were grown on 30 kPa gels for up to two weeks and stained for Ezrin and Actin. Because buds are characterized by Actin and Ezrin enrichment in their external layer (figure 4.1.6), we decided to use these two markers as a tool to identify morphological changes occurring during the budding process.

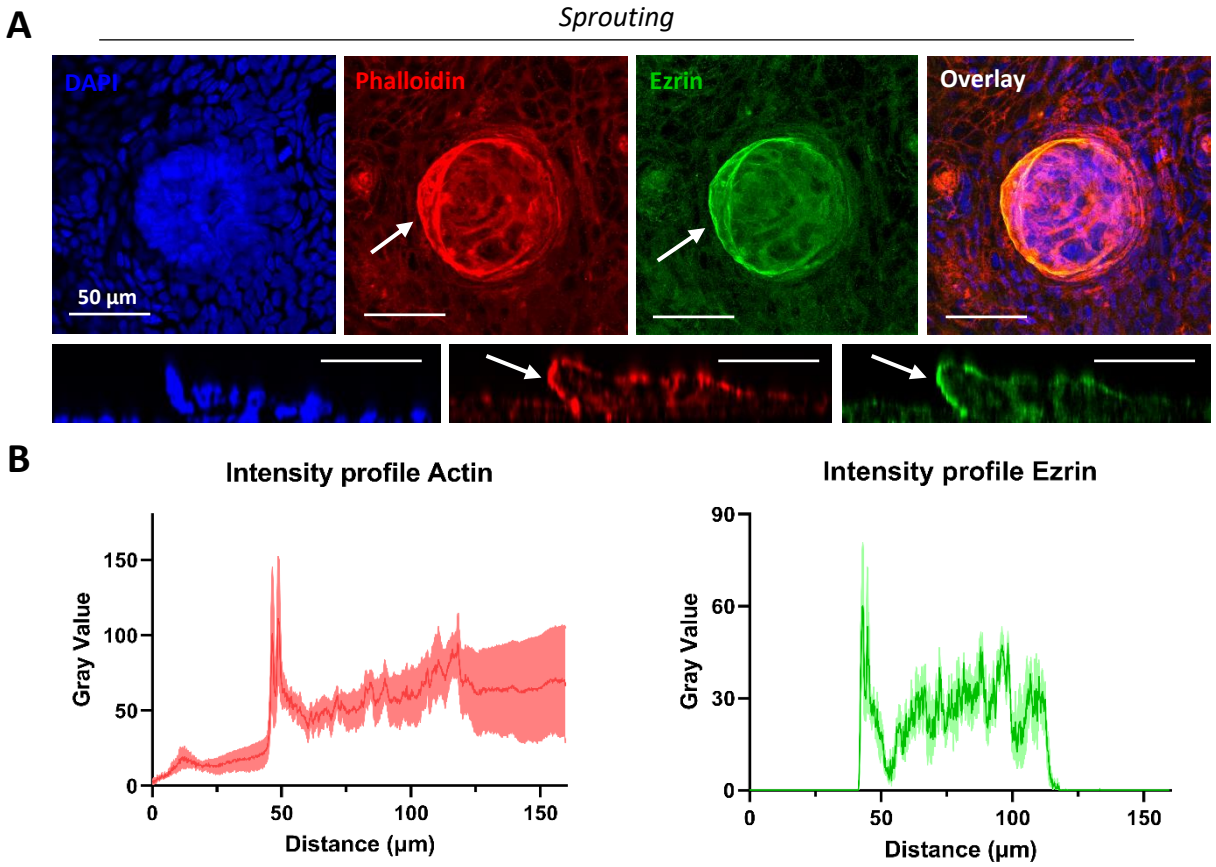


***Figure 4.2.1.*** *(A) Confocal microscopy images of representative MAX projections of middle z-stacks (upper rows) and orthogonal cross-sections (lower rows), showing the first morphological step of bud formation, the sprouting. White arrows point at the portion of the monolayer from where the bud arises. Nuclei are labelled in blue, Actin is labelled in red and Ezrin in green. Scale bars: 50 µm. (B) Intensity profile plots for Actin and Ezrin of buds sprouting from LS513 epithelia grown on 30 kPa PAA hydrogels. Graphs represent means ± SEM of 6 different budding regions. N= 2 experiments.*

Indeed, we could identify three different morphologies in buds, defined by distinct Actin and Ezrin intensity profiles, that we linked to three different budding steps. The first morphology that we identified was characterized by the asymmetrical accumulation of Actin and Ezrin at one side of the structure (figure 4.2.1A-B), corresponding to the monolayer portion already emerged from the rest of the epithelium. The example reported in figure 4.2.1A shows a bud starting to sprout from the left (white arrows), while the right side remains as thick as the rest of the epithelium. We hypothesized that the first step in budding, which we named sprouting, is characterized by the asymmetrical emergence of a protruding structure.

The second morphology identified is shown in figure 4.2.2A. In this case the bud is protruding 20-30 µm from the monolayer, and displays the typical features of mature buds, with Actin and Ezrin strongly expressed in the apical side. Indeed, as displayed by the plots in figure 4.2.2B, this step is characterized by two higher peaks of Ezrin or Actin fluorescence, corresponding to the external sides of bulging structures.

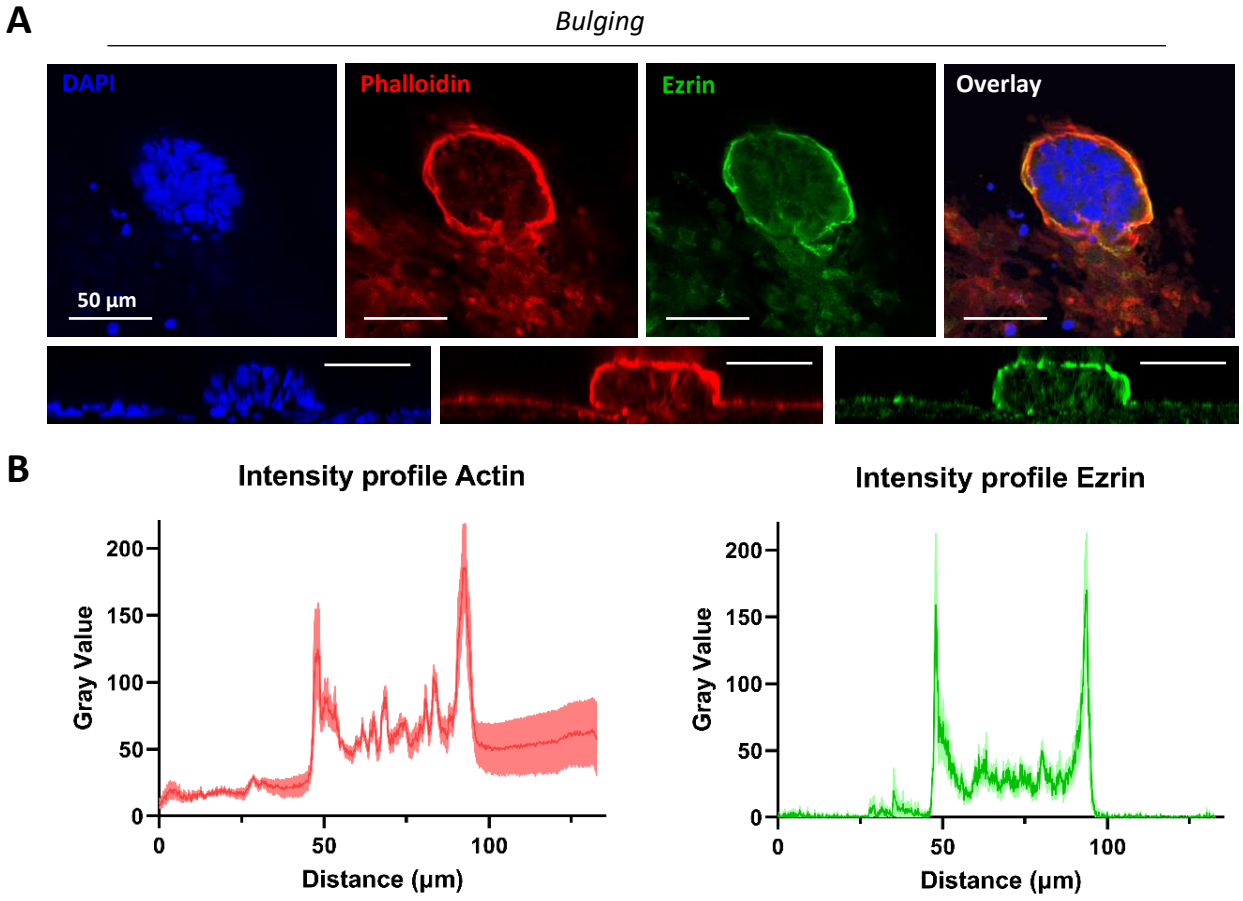

***Figure 4.2.2.*** *(A) Confocal microscopy images of representative MAX projections of middle z-stacks (upper rows) and orthogonal cross-sections (lower rows), showing the second morphological step of bud formation: the bulging. Nuclei are labelled in blue, Actin is labelled in red and Ezrin in green. Scale bars: 50 µm. (B) Intensity profile plots for Actin and Ezrin of buds bulging from LS513 epithelia grown on 30 kPa PAA hydrogels. Graphs represent means ± SEM of 6 different budding regions. N= 2 experiments.*

We hypothesized that this morphology corresponded to a second step leading to TSIPs formation, which we named bulging.

The third morphology identified was less frequent (Figure 4.2.3A), as it was only observed in 4 cases out of approximately 40 buds imaged. It was characterized by the presence of three distinct regions of high Actin or Ezrin fluorescence (plots in figure 4.2.3B). The first and last peaks depicted in the graphs correspond to the external sides of buds, while the middle peak represents the internal side of buds bulging from other pre-existing structures. We hypothesized that this rare morphology corresponds to a third step in budding, defined as the bulging of a pre-existing bud and named scission. We noticed that this secondary bud could develop while still attached to the monolayer, like the one shown in figure 4.2.3A, or in the lumen completely detached from the rest of the epithelium (shown later in figure 4.2.9B)

Therefore, based on Ezrin and Actin expression, we identified three distinct morphological states in the budding structures which we link to different steps eventually leading to TSIPs release: 1) the sprouting, defined by an asymmetric accumulation of Actin and Ezrin at one side of the emerging structure, 2) the bulging, characterized by the formation of a mature bud that emerges of 20-30 µm from the monolayer and 3) the scission, defined as the bulging of a pre-existing bud. The complete process is summarized in the cartoon in figure 4.2.4.

Since we identified different morphological states of bud formation, we wondered if these morphological transitions would have a particular mechanical signature. Namely, we wondered if budding areas would show different traction forces profiles with respect to normal flat (non-budding) epithelium. To do so, LS513 cells were grown on 30 kPa gels and imaged for up to 3 days, starting from 80-90% confluence. As described in the Methods section, forces exerted by the cells were quantified using a custom particle image velocimetry (PIV) software in Matlab. As shown by the time-lapses and by the graph in figure 4.2.5, forces exerted where the bulging structure is arising are significantly higher during budding, if

compared to flat epithelium. Interestingly, when looking at the averaged tractions along time (Figure 4.2.5B), we can observe that monolayer areas that will bud exert higher tractions than non-budding regions even before the onset of budding. Such increase could be caused by the tissue being under compression. Conversely, once the bud is fully formed, traction forces underneath the budding region decrease and match the tractions applied on the substrate by normal flat monolayer.

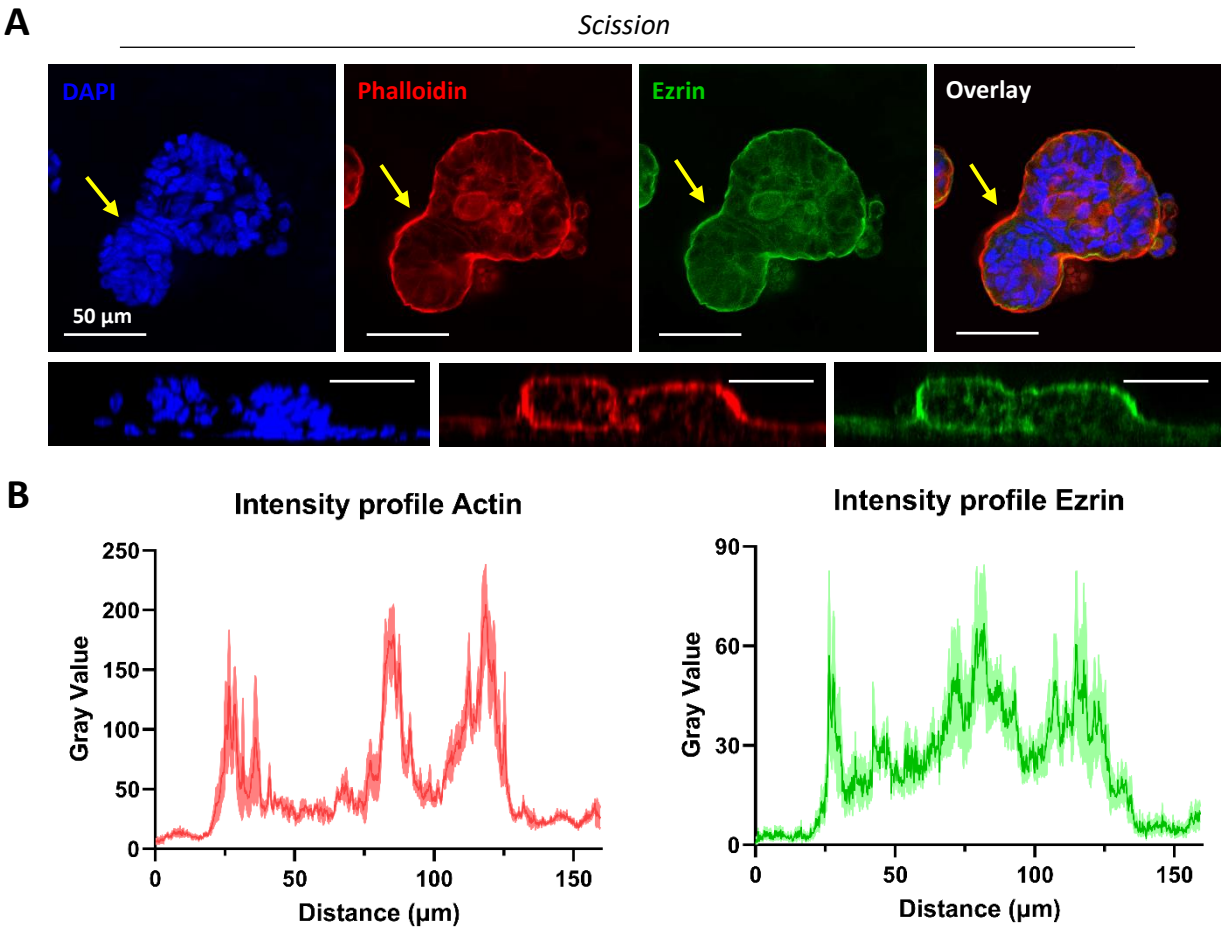


***Figure 4.2.3.*** *(A) Confocal microscopy images of representative MAX projections of middle z-stacks (upper rows) and orthogonal cross-sections (lower rows), showing the last morphological step of bud formation: the scission. Yellow arrows point at a bud forming from a pre-existing budding structure. Nuclei are labelled in blue, Actin is labelled in red and Ezrin in green. Scale bars: 50 µm. (B) Intensity profile plots for Actin and Ezrin of buds undergoing scission, grown on 30 kPa PAA hydrogels. Graphs represent means ± SEM of 4 different budding regions. N= 2 experiments.*

Because tractions are exerted through the adhesion between epithelia and substrate surface, we next analysed focal adhesions of mature buds to account for the decrease in tractions forces.

Imaging and quantification of Vinculin expression in mature buds (figure 8.1.2, Appendix) showed that focal adhesion surface inside buds is almost a half of the one in the rest of the epithelium (Figure 4.2.6C), suggesting that cell adhesion is weaker underneath the buds. We could also observe the presence of a basal cavity, where Actin is absent and only cell debris or dead cells are visible (dotted areas in figure 4.2.6A). Indeed, the basal z-stacks and the orthogonal cross-sections in figure 4.2.6A, clearly show the formation of a cavity. As shown by the graph in figure 4.2.6B, this cavity was visible in 48,5 $\pm$ 1,5 % of mature buds.

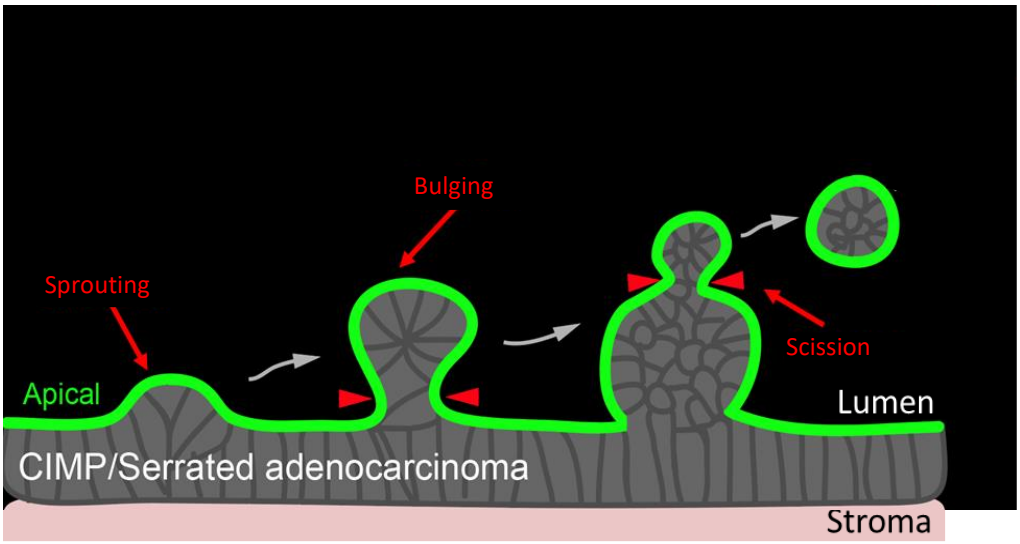


***Figure 4.2.4.*** *Cartoon depicting the hypothesized morphological steps leading to TSIPs release: sprouting of the epithelia, budding and scission. CIMP: CpG island methylator phenotype. Readapted from Zajac et al. (2018).*

These results suggest that mature budding structures are partially detached from the underlying substrate, which could explain the decrease observed in cell tractions.

Altogether, our running model for LS513 epithelia budding is characterized by 3 distinct morphological steps, namely sprouting, bulging and scission, which are characterized by a transient increase of traction forces during sprouting and bulging formation, followed by a decrease of traction forces when buds are mature.

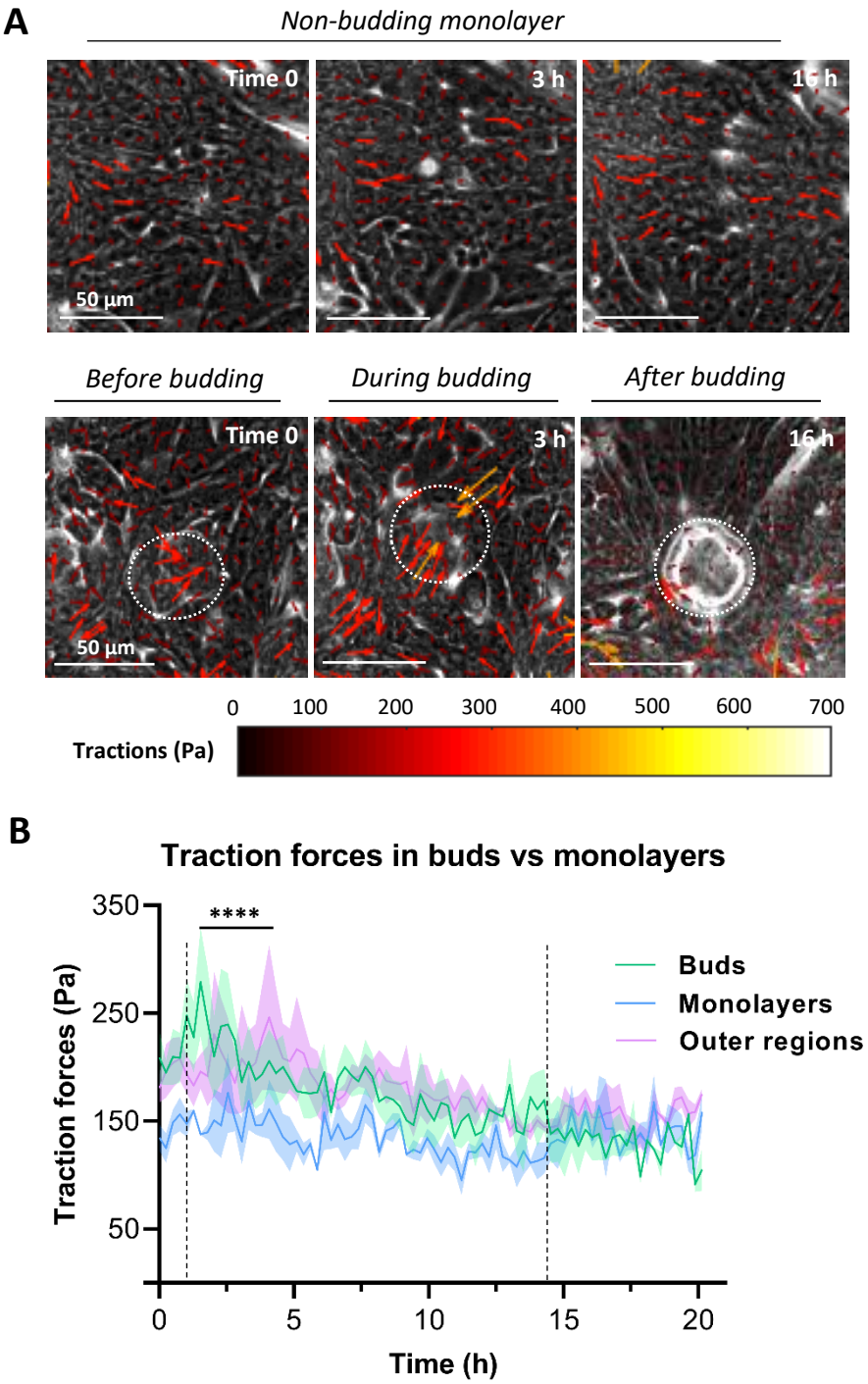


***Figure 4.2.5.*** *(A) Representative phase contrast time-lapses and traction vectors in a bulging area vs in a non-budding monolayer region. Dotted circle: area where bud is forming. Scale bars: 50 µm. (B) Traction forces quantification in budding areas, in regions surrounding budding areas (outer) and in non-budding regions. Dotted lines delimit the three periods shown in (A): before, during and after budding. Analysis done on 3 budding regions, 3 regions surrounding budding and 3 flat non budding areas. Graphs represent means ± SEM of medians at each time point. Two-way ANOVA. Buds vs non-budding regions: before and during budding: p<0.0001 = (****), after budding: not significant. Regions surrounding buds vs non budding regions: before and during budding: p<0.0001 = (****), after budding: not significant. Buds vs regions surrounding buds: always not significant.*

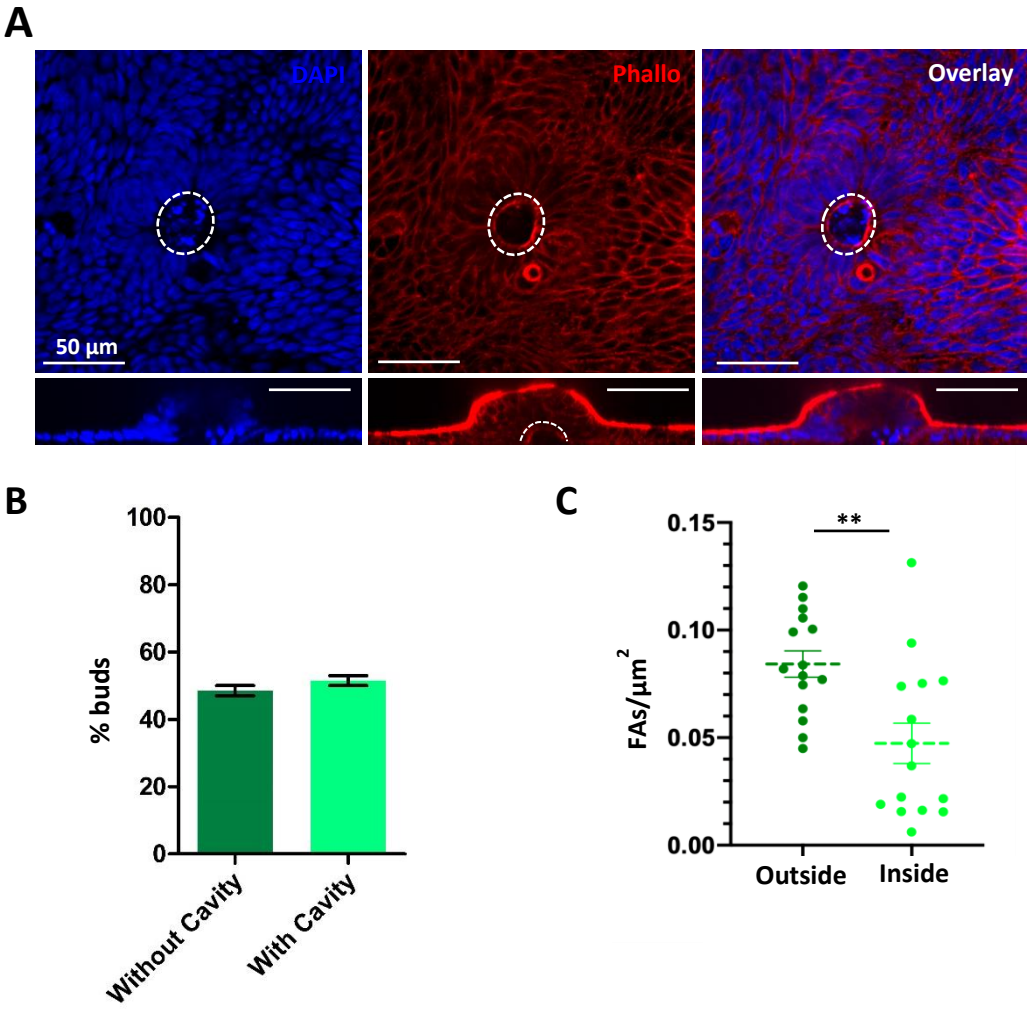


***Figure 4.2.6.*** *(A) Confocal microscopy images of basal z-stacks (upper row) and orthogonal cross-sections (lower row), showing basal cavity (dotted areas) below a mature bud. Actin is labelled in red, Nuclei are labelled in blue. Scale bars: 50 µm. (B) Percentage of mature buds showing a basal cavity. Analysis done on a total of 23 mature buds. N= 2 experiments. (C) Focal adhesion density (for µm$^2$) inside buds vs outside budding regions. p<0.01 = (**), T-test. N= 2 experiments.*

*4.2.2 Substrate stiffness regulates budding in LS513 epithelia*

Most epithelial cells are known to exert more forces on stiff substrates than on soft ones[126,127,128]. Moreover, several research groups have recently reported that stroma stiffening induces cancer cells migration and fosters metastasis[24,56,57,58,59]. Since we showed that traction forces are higher in bulging structures with respect to flat monolayer, we hypothesised that, by changing substrate stiffness, we could alter the budding process.

First, we wanted to confirm that our cell model could apply more forces if plated on stiffer substrates. To do so, we plated LS513 epithelial cells on PAA gels with different stiffness, namely 3, 12, 30 and 60 kPa, and calculated the forces exerted on them by the cells. In order to visualize how the magnitude of traction forces was changing during the time in which LS513 cells were imaged, we combined the data obtained for several experiments and plotted the median values of traction magnitudes. As shown by the graph in figures 4.2.7A, LS513 cells exert higher traction forces if plated on stiffer gels in comparison to softer gels, as it has been reported in other epithelial systems[126,127,128].

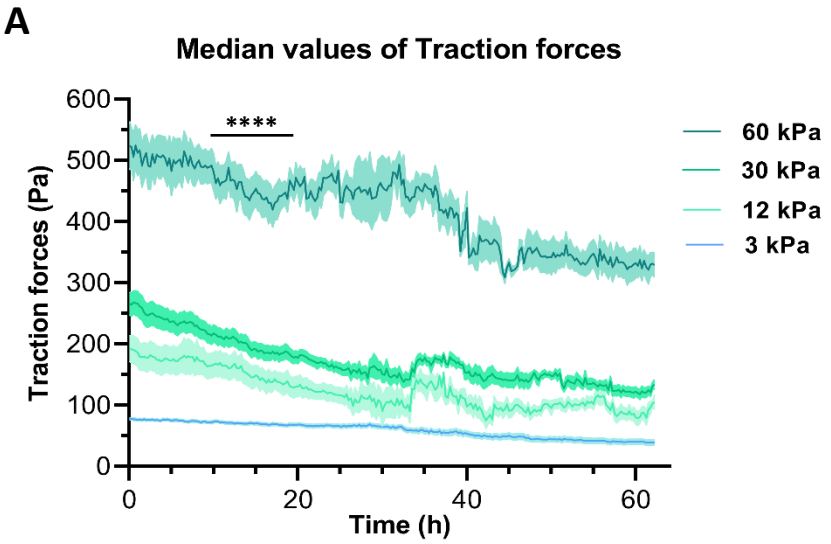


***Figure 4.2.7*** *(A) Time evolution of traction magnitudes over time in whole LS513 epithelia grown on 60, 30, 12 or 3 kPa gels. Curves represent means ± SEM of median values at each time point. Two-way ANOVA, p<0.0001 = (****). Combined data obtained for traction microscopy analysis done on minimum 7 videos for condition, from at least 2 independent experiment repeats.*

Next, we assessed if substrate elasticity would have an impact on bud morphology, as well. To do so, cells were cultured on PAA gels with different stiffness (3, 12, 30 and 60 kPa) for approximately 2 weeks and then immunostained for DAPI, Actin and Ezrin.

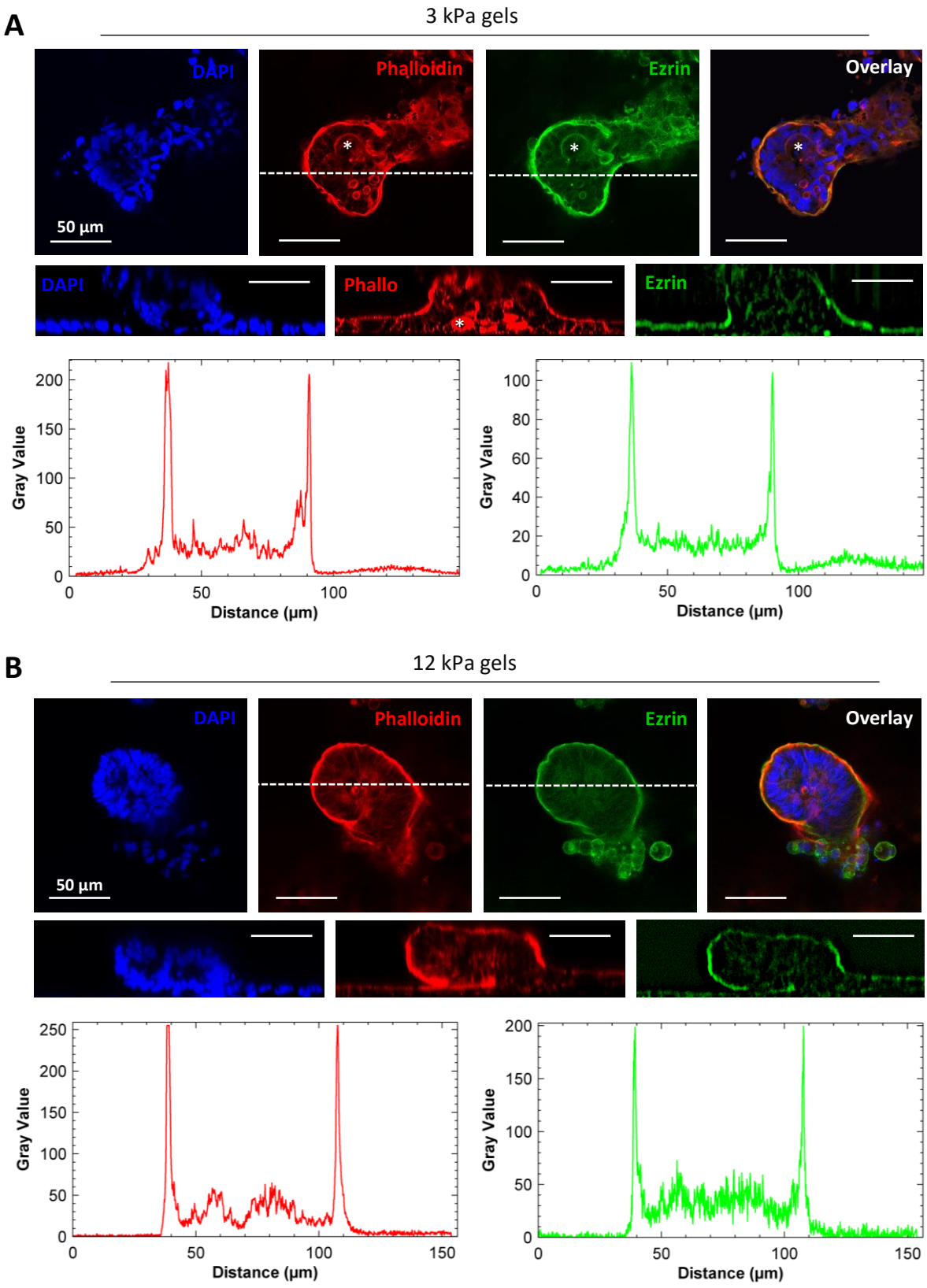


***Figure 4.2.8.*** *(A) Representative confocal microscopy images of middle z-stacks MAX projections (upper rows), orthogonal cross-sections (middle rows), and intensity profiles for Actin and Ezrin (lower rows) of a bud protruding from LS513 epithelia grown on 3 kPa PAA hydrogels. White asterisk points at a lumen-like structure. The graphs plot phalloidin (red) and ezrin (green) intensities along the white dashed line shown in the panels above. (B) Representative confocal microscopy images of middle z-stacks MAX projections (upper rows), orthogonal cross-sections (middle rows), and intensity profile*

*plots for Actin and Ezrin (lower rows) of a bud arising from LS513 epithelia grown on 12 kPa PAA hydrogels. The graphs plot phalloidin (red) and ezrin (green) intensities along the white dashed line shown in the panels above. Nuclei are labelled in blue, Actin is labelled in red and Ezrin in green. Scale bars: 50 µm. N= 3 experiments.*

As displayed by the z-stacks and the cross-sections in figures 4.2.8 and 4.2.9, LS513 cells were able to bud in all the conditions analysed. Moreover, as shown by the intensity profiles reported in figures 4.2.8 and 4.2.9, the expression of polarity markers of buds on hydrogels is analogous to the one on stiff substrate (figure 4.1.6A and B). Indeed, in all the conditions the budding structures show Actin and Ezrin enrichment in the external layer. However, it should be noted that LS513 cells plated on 3 kPa gels often organize in networks instead of monolayer (figure 8.1.3, Appendix) and rarely form a confluent epithelium. Additionally, as shown by the z-stacks and the cross-sections in figure 4.2.8.A, buds formed on 3 kPa gels present vacuoles or small lumens (white asterisk) that are absent in the other conditions.

We then assessed whether culturing the LS513 cells on soft gels could also affect the size of budding structures. Therefore, we evaluated the average surface of buds produced by epithelia grown on substrates with different stiffness. For completeness, a 'super-stiff' condition was included too; therefore, apart from hydrogels, bud area was also measured on conventional plastic or glass-bottom dishes.

As shown by the graph in figure 4.2.10, culturing LS513 cells on soft hydrogels heavily impacts on bud surface. Indeed, the area of bulging structures is bigger on stiffer gels or on plastic, if compared to softer ones. The average surface of buds is 2613 ± 412 $\mu m^2$ on 3 kPa gels, 3560 ± 472 $\mu m^2$ on 12 kPa gels, 5557 ± 1165 $\mu m^2$ on 30 kPa gels, 5450 ± 996 on 60 kPa gels and 8808 ± 1010 on plastic. Surprisingly, despite the difference in tractions (Figure 4.2.7), we found no difference in surface of buds grown on 30 kPa gels, in comparison to the ones grown on 60 kPa gels. This suggests that traction forces do not directly correlate to bud size.

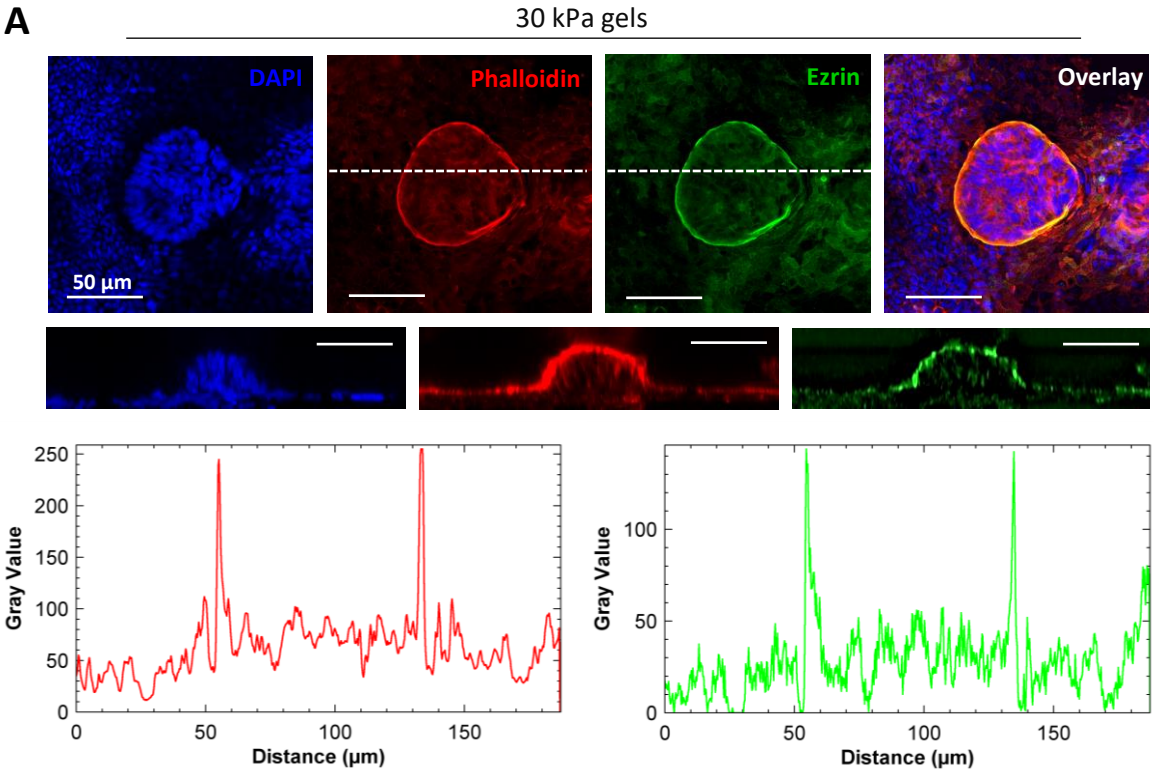
A
30 kPa gels
DAPI
Phalloidin
Ezrin
Overlay
50 µm
Gray Value
Distance (µm)
B
60 kPa gels
DAPI
Phalloidin
Ezrin
Overlay
50 µm
Gray Value
Distance (µm)

***Figure 4.2.9.*** *(A) Representative confocal microscopy images of MAX projections of middle z-stacks (upper rows), orthogonal cross-sections (middle rows), and intensity profile plots for Actin and Ezrin (lower rows) of a bud protruding from LS513 epithelia grown on 30 kPa PAA hydrogels. The graphs plot phalloidin (red) and ezrin (green) intensities along the white dashed line shown in the panels above. (B) Representative confocal microscopy images of middle z-stacks MAX projections (upper rows), orthogonal cross-sections (middle rows), and intensity profile plots for Actin and Ezrin (lower rows) of a bud arising from LS513 epithelia grown on 60 kPa PAA hydrogels. White arrows point at a bud forming from a pre-existing budding structure. The plots show phalloidin (red) and ezrin (green) intensities along the white dashed line shown in the panels above. Nuclei are labelled in blue, Actin is labelled in red and Ezrin in green. Scale bars: 50 µm. N= 3 experiments.*

Finally, we wanted to evaluate if culturing the LS513 cells on substrates with different stiffness could affect not only bud size but also the quantity of buds formed on the epithelia. To quantify the total number of buds produced for each condition, we imaged the cells employing phase contrast, DAPI, Phalloidin and Ezrin signal (figure 4.2.11A) and counted the bulging structures arising in the whole monolayer. As shown in the graph in figure 4.2.11B, cells produce more buds if plated on plastic or on 60 kPa gels, in comparison to 30, 12 and 3 kPa conditions. Indeed, the buds produced for $cm^2$ were 762 ± 40, 586 ± 63, 158 ± 14, 89 ± 12 and 38 ± 3 in the plastic, 60, 30, 12 and 3 kPa conditions, respectively. These results show that bud formation is impaired at very low stiffness, while is heavily induced by substrate stiffening.

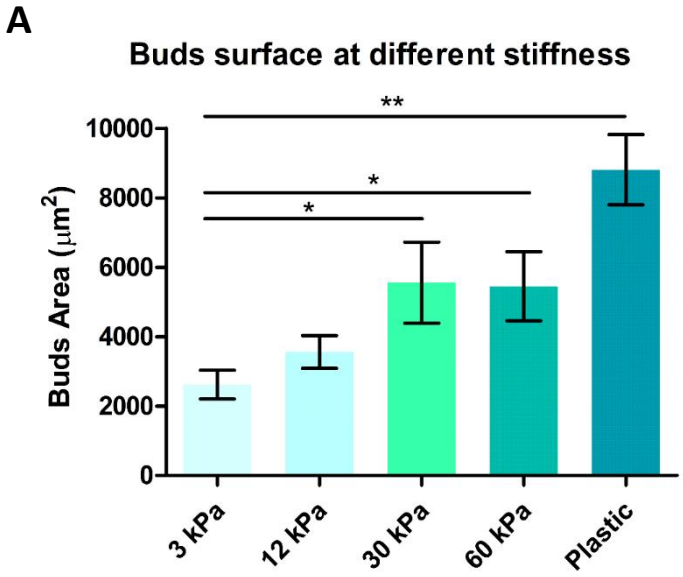


***Figure 4.2.10.*** *(A) Quantification of bud surface at different stiffness. Results are presented as mean ± standard error of the mean (SEM). 3 kPa vs 12 kPa, 30 kPa vs 60 kPa: not significant. p<0.05 = (*), p<0.01 = (**), t-tests, N= 2 experiments.*

Taken together, all these results demonstrate that substrate stiffness regulates the budding process in LS513 epithelia. Both the number of buds formed, and the size of those buds depend on the stiffness of the underlaying substrate. Our results show that bud number and size increase with increasing substrate stiffness, highlighting the importance of matrix stiffening in colorectal cancer.

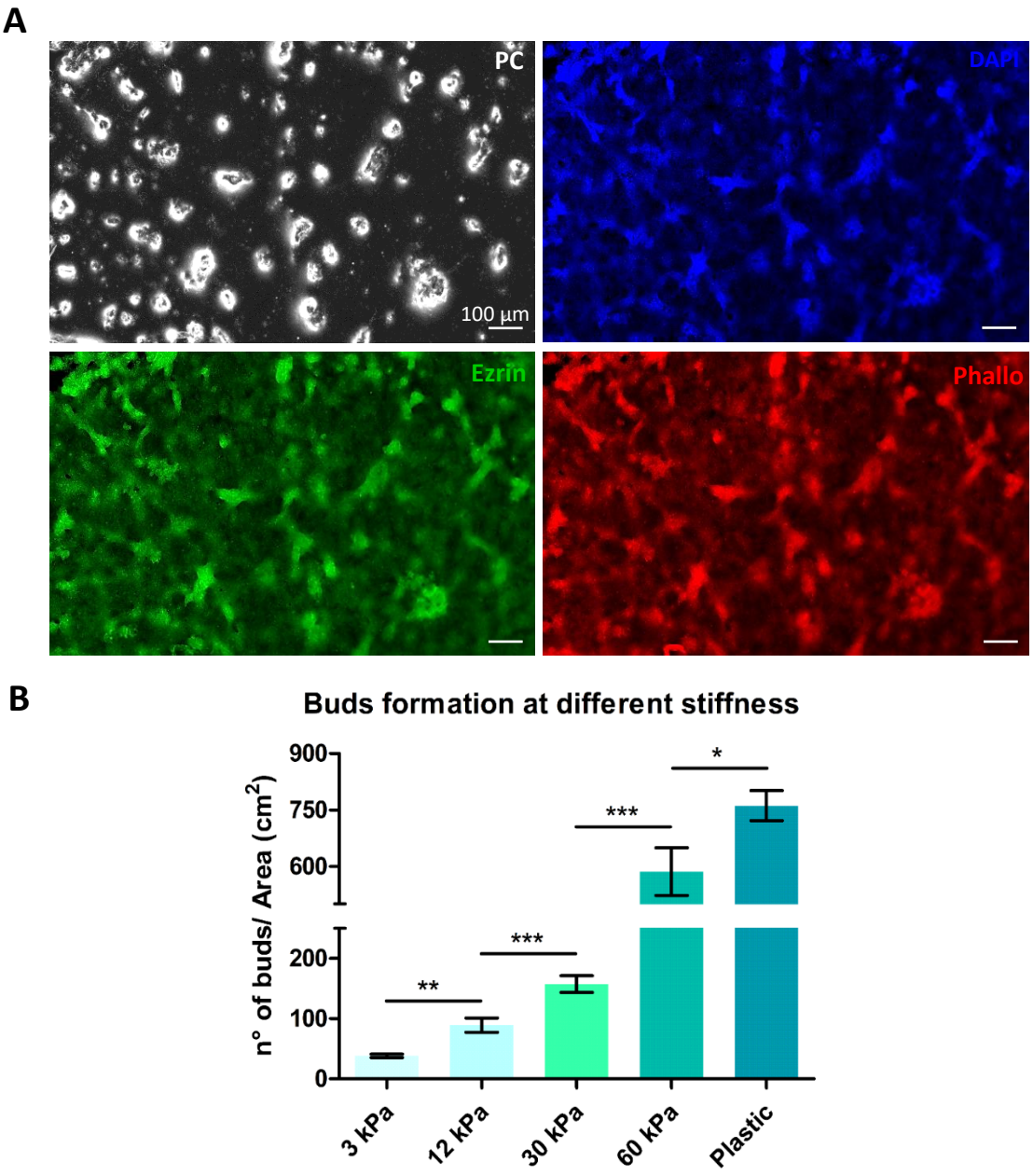


***Figure 4.2.11.*** *(A) Representative phase contrast and epifluorescence images, displaying a portion of LS513 monolayer grown on 60 kPa gels and showing several budding structures. PC: phase contrast, Nuclei are labelled in blue, Actin is labelled in red and Ezrin in green. Scale bars: 100 µm. N= 3 experiments. (B) Quantification of buds' formation at different stiffness. Bud counts were normalized for a surface of 1 cm². Results are presented as mean ± standard error of the mean (SEM). p<0.05 = (*), p<0.01 = (**) and p<0.001 = (***),* t-tests, *N= 3 experiments.*

*4.2.3 MAPK pathway inhibition causes budding impairment in LS513 epithelia*

Once we had established the different steps of the budding process and its dependence to substrate stiffness, we wanted to identify the molecular pathways that could be implicated in budding. Considering that most colorectal cancer patients developing budding had a mutation on KRAS gene, and that our cell model displays the same mutation (tables 1 and 2, Appendix), we wondered if this oncogene and/or the signalling pathways associated to its activation were responsible for budding.

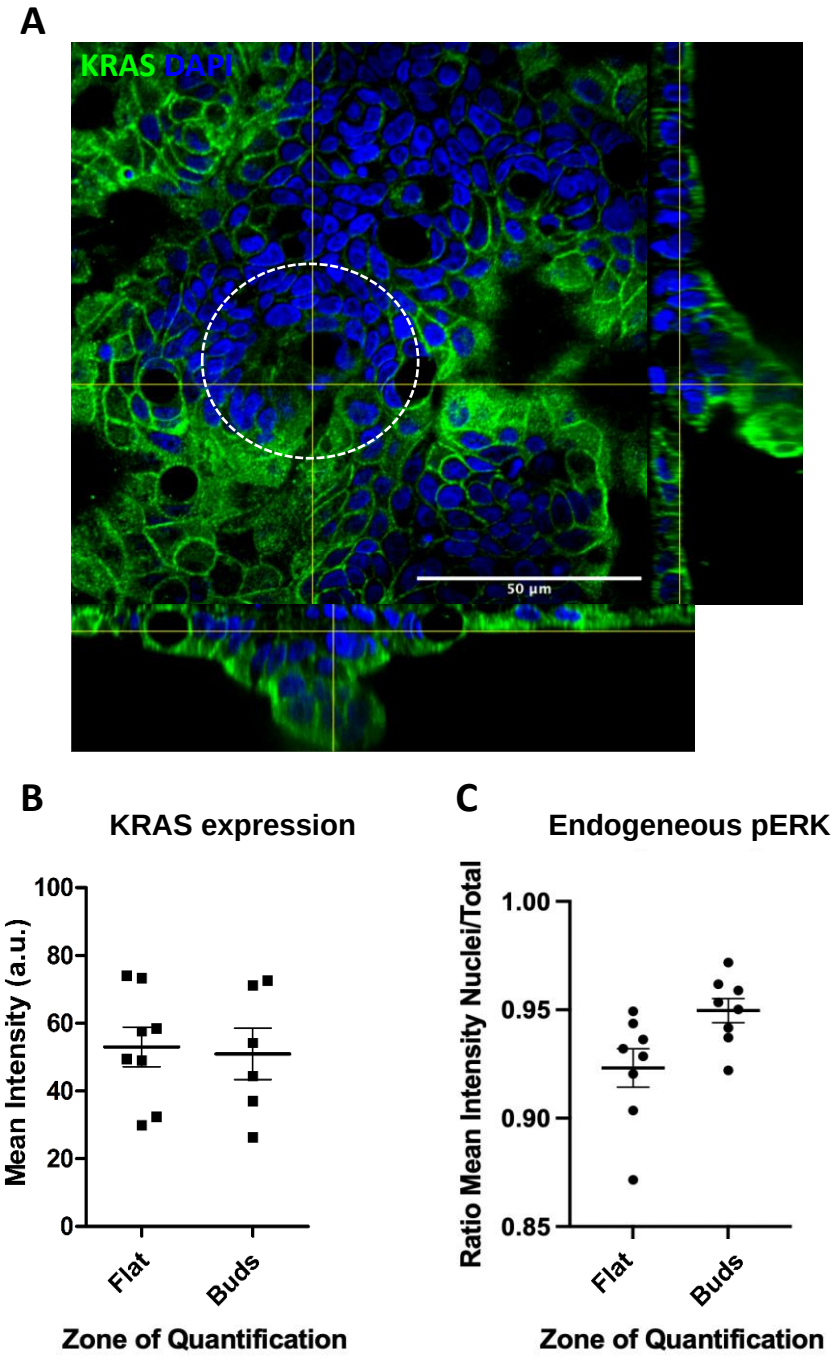

***Figure 4.2.12.*** *(A) Confocal microscopy images showing representative basal z-stacks and orthogonal cross-sections, showing a bud protruding from LS513 epithelia grown on glass. Nuclei are labelled in blue, KRAS in green. The dotted circle frames the budding area. Scale bar: 50 µm. (B) Quantification of KRAS expression in buds vs flat non-budding monolayer. Results are presented as mean ± standard deviation of the mean (SEM). Non-budding monolayer vs Bud: not significant, t-test. N= 2 experiments. (C) Endogenous Phosfo-ERK quantification in buds vs flat non-budding monolayer. Results are presented as mean ± standard deviation of the mean (SEM). Normal monolayer vs Bud: not significant, t-test. N= 3 experiments.*

Several studies have reported that KRAS and HRAS overactivation or overexpression result in mechanical alterations that could lead to large-scale deformations of epithelial tissues, including buckling and folding [18,33,34,39].

Therefore, we hypothesised that also budding regions in LS513 epithelia could be marked by higher expression of KRAS. To evaluate if the presence of buds correlates with a stronger expression of KRAS, we stained LS513 epithelia cultured for up to 2 weeks with an antibody specifically recognizing KRAS protein and we imaged them by Confocal microscopy (figure 4.2.12A).

As shown in figure 4.2.12A and by the graph in figure 4.2.12B, KRAS is not preferentially over-expressed in budding structures with respect to the rest of the epithelium. Therefore, we thought that instead of KRAS expression, we could see a significant difference in the activation of MAPK pathway at the level of buds. This pathway is indeed one of the main signalling cascades induced by KRAS oncogene activation[29].

Since ERK is a downstream effector of the MAPK pathway that it is active if phosphorylated[42], we hypothesised that the phosphorylated form of this protein (pERK) could be more abundant in budding structure with respect to the rest of the monolayer. Therefore, we quantified the levels of endogenous pERK in buds with respect to the rest of the monolayer. As depicted by figure 4.2.12C, the increase in pERK in bulging structures was only modest and not statistically significant.

Even if we did not see a significant increase in the expression of KRAS nor in the levels of pERK, we still wanted to assess whether LS513 cells treated with MAPK inhibitors produced less buds in comparison to control epithelia. Thus, we treated the cells with two different MAPK inhibitors, Trametinib and SCH772984 (SCH), and we evaluated the number of buds after 3 days of treatment.

As displayed by the brightfield images in figure 4.2.13A and by the plot in figure 4.2.13B, cells treated with SCH or Trametinib showed a significant reduction in buds' number, when compared to untreated LS513 cells. Therefore, despite the absence of a preferential localization of KRAS or pERK in budding structures, we can state that overall MAPK activation throughout the epithelium is required for budding.

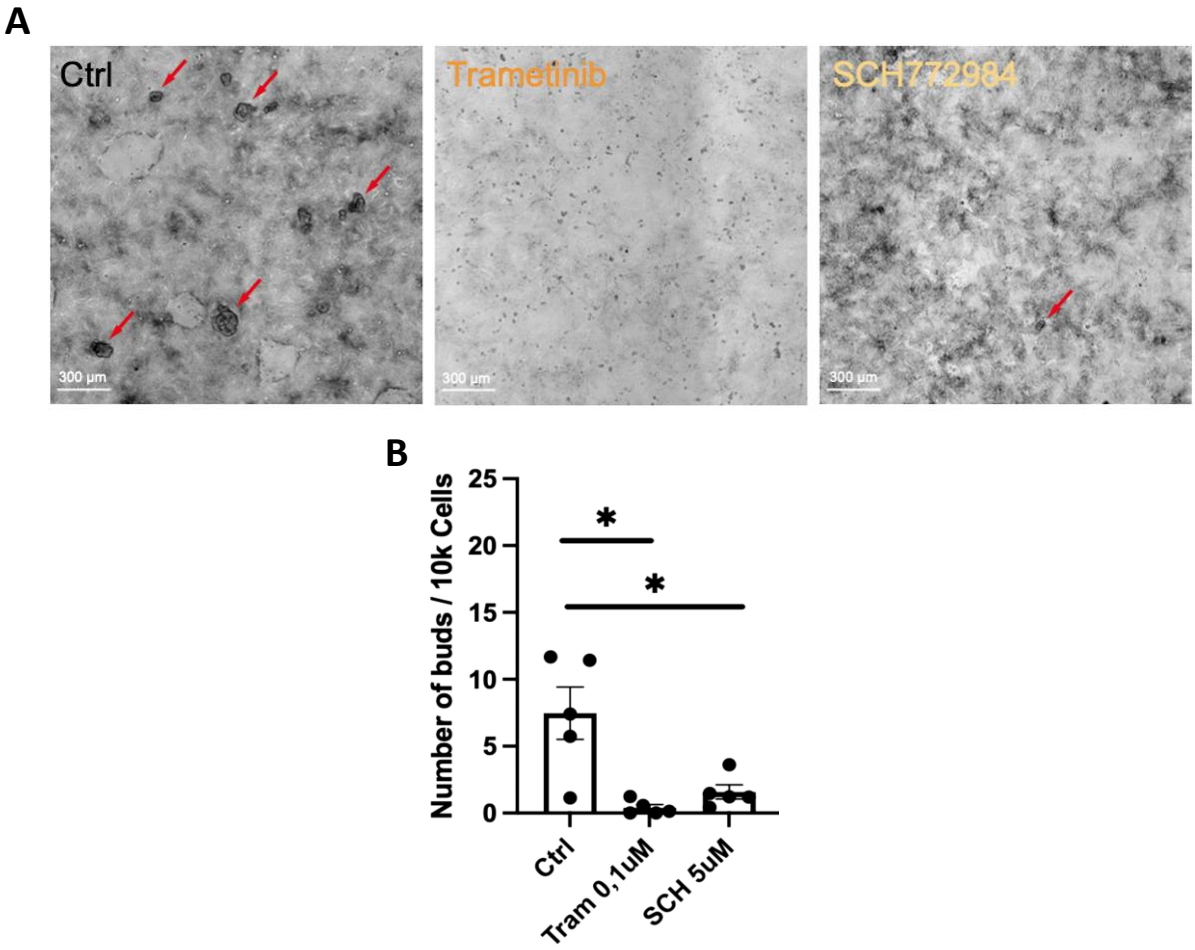


***Figure 4.2.13.*** *(A) Brightfield images showing not-treated LS513 epithelia and monolayers treated with SCH or Trametinib. Red arrows point at budding structures. Scale bars: 300 µm. (B) Bud quantification on LS513 cells not treated vs cells treated with MAPK inhibitors (Trametinib and SCH). Results are presented as mean ± standard deviation (SD). p<0.05 = (*)*, t-test. *N= 3 experiments.*

Our results attest that MAPK pathway activation is a necessary condition for LS513 budding, but immunostaining of KRAS and pERK, respectively upstream and downstream to MAPK cascade induction, showed an overall expression rather than a particular spatial localization. On the contrary, the characterization of the budding process in section 4.2.1 showed that budding is a local phenomenon with a specific mechanical signature.

Therefore, what triggers the formation of buds at specific locations within the monolayer remained unknown. At this point, to gain deeper insight into this phenomenon, we decided to study two local cellular features, namely cellular velocities and cellular orientations, during budding formation.

*4.2.4 Budding of LS513 epithelia is associated with higher cellular vorticity*

We wanted to assess if bud formation could be associated with specific cellular movements that could drive the budding process. We wondered if it would be possible to identify a specific pattern of cell velocities that might anticipate bud arising. Therefore, we characterized the velocities of LS513 cells grown on 30 kPa gels, using PIV software in Matlab. We chose to perform this analysis on hydrogels having this stiffness, because such value mimics the average rigidity of the colorectal tumour microenvironment[57].

Figure 4.2.14A shows a representative analysis on velocities (vectors in green), done on videos taken before, during and after the formation of a bud in a budding area as well as a non-budding area of the monolayer. During bud formation, we always noticed the presence of a peculiar pattern of cell velocities, creating a sort of vortex/whirlpool around the area where the bud would form, as displayed by the middle panel in the second row in figure 4.2.14A (framed by the white square). These velocities patterns rapidly disappeared after the formation of the bud (last panel, figure 4.2.14A).

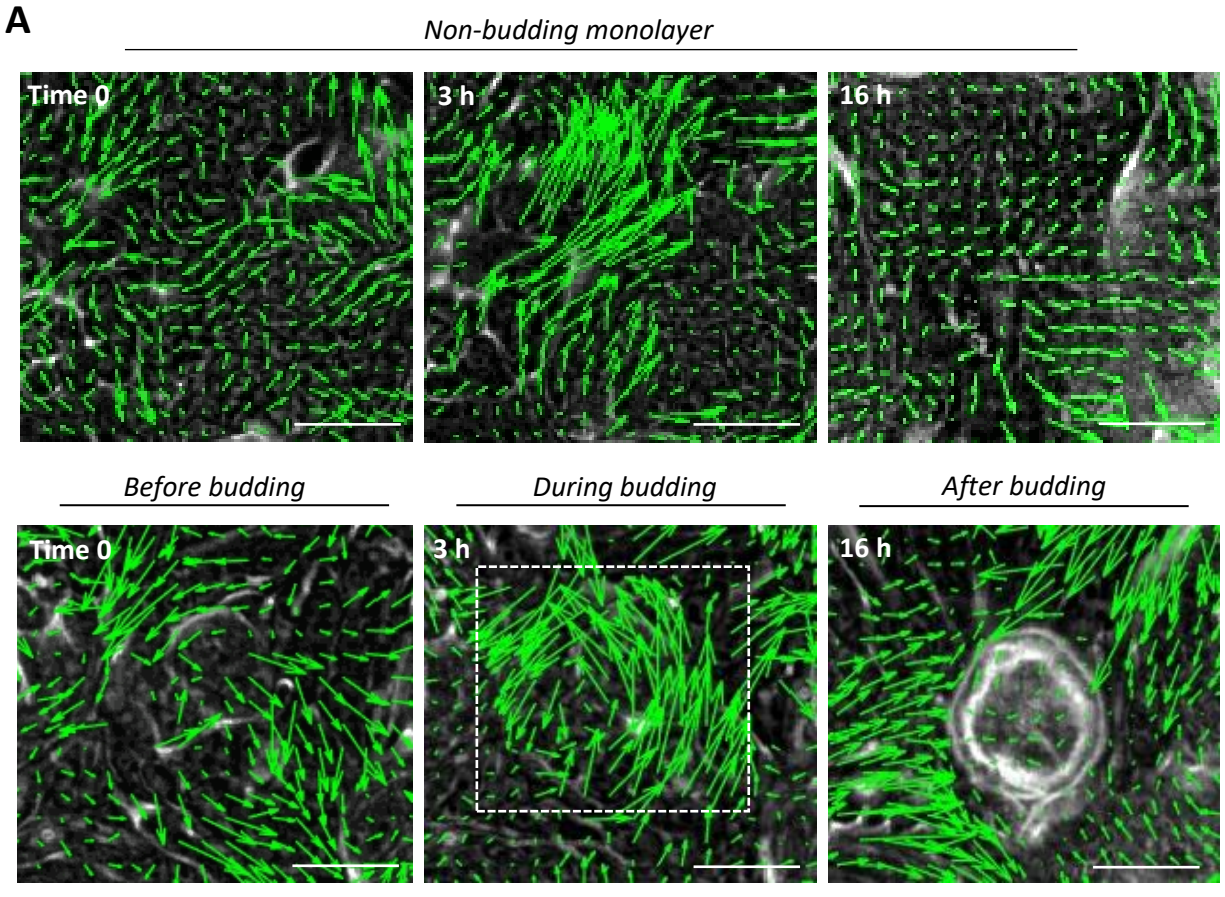

***Figure 4.2.14.*** *(A) Velocity vectors (in green) of L513 cells grown on 30 kPa PAA hydrogels before, during and after bud formation and in a non-budding portion of monolayer. White square frames the monolayer portion where the bud is forming. Scale bars: 50 µm.*

Since the presence of vortexes in the monolayer is associated with vorticity, we measured this variable in budding regions and in non-budding regions of LS513 epithelia. For this analysis, we selected just budding regions in which only a single bud was arising and that were completely flat at the beginning of the imaging. We therefore assessed the vorticity before, during and after budding formation, namely when a fully formed structure was emerged.
As depicted by the representative heatmaps and by the violin dotted graphs shown in figure 4.2.15, regions where a bud is emerging present several whirling spots (red and dark blue spots in 4.2.15A) and higher average vorticity, if compared to non-budding areas (4.2.15B, plot in the middle). Moreover, even if the vorticity slightly decreases when the buds are already emerged, it is still significatively higher than in non-budding regions (figure 4.2.15B, last panel). On the other hand, before budding, the vorticity of areas where a bud would form and the one of non-budding areas are comparable (4.2.15B, plot on the left).

Overall, these results indicate that budding occurs in regions of LS513 epithelium characterized by high cell vorticity.

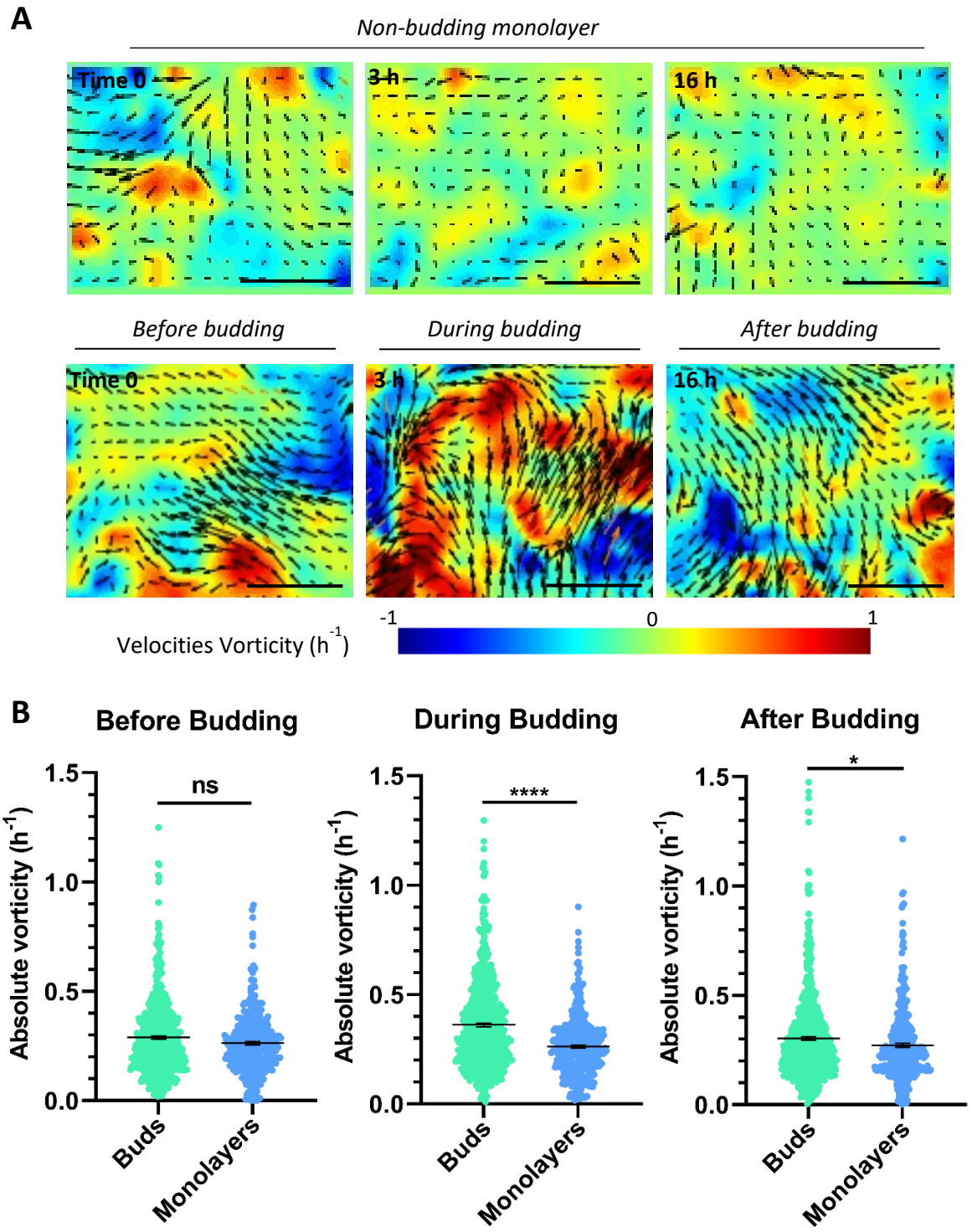


***Figure 4.2.15.*** *(A) Heatmaps displaying velocities vorticity of the same budding area shown in 4.2.13 vs a non-budding portion of LS513 epithelium grown on 30 kPa gels. Scale bars: 50 µm. (B) Violin dotted plots showing the absolute value of vorticity of LS513 cells in budding areas vs non budding areas. Each dot corresponds to the absolute vorticity of a singular interrogation window (roughly a cell). Analysis done on 3 budding regions vs 6 non-budding monolayer areas. Thin black line: mean value of velocity magnitude. Thick black line: standard deviation of the mean (SEM).*

*4.2.5 Buds emerge from monolayer regions with high topological charge*

Having demonstrated that bud formation is associated with the presence of cellular swirls and higher vorticity, we wondered whether also specific cell orientations and topological defects could play a role in this process. In the last decade, various groups have highlighted the importance of topological defects in regulating cellular processes such as extrusion, apoptosis and the emergence of complex multicellular architectures[108,112,113,102,129]. Therefore, as budding of LS513 could be seen as a sort of multicellular apical extrusion, we hypothesised that topological defects could play a fundamental role also in this process as well.

To confirm that the presence of budding structures was associated with topological defects, we studied the cellular orientations in confocal images of buds grown on stiff substrates as well as on soft ones. To do so, we imaged E-cadherin or Actin and processed the images on ImageJ to properly visualize cells boundaries, as described in section 3.9 of Materials and Methods. As shown in figure 4.2.16, both on glass and on 30 kPa gels, cells below buds were showing abrupt changes in cell orientation (middle and bottom panel), if compared with monolayer areas in which buds were not found (top panel).

As we wanted to understand if we could identify these specific cell orientations even before mature bud formation, we also studied cell orientation in live imaging. Indeed, we wanted to assess whether we could use these abrupt changes in cell orientations as predictors of monolayer areas where buds would form. Therefore, we took 3-day-videos of LS513 cells grown on 30 kPa gels and we analysed the cell orientations in all the resulting phase contrast time-lapses. To maximize the chance of catching the formation of various buds, we started imaging the cells after they reached a confluence of at least 80-90%.

As shown in figure 4.2.17A, discontinuities in the orientation field of LS513 cells were visible also before and during bud formation; indeed, cells around the bulging area were organized in distinct domains having different long-range directional order. These cells were behaving as if they were trying to circumvent a sort of obstacle encountered in the monolayer[130]. Later, we characterized which topological defects were associated with these specific cell orientation patterns.

Using cell orientations calculated with OrientationJ plugin and employing a customized code in Matlab, as described in section 3.10.1 in Material and Methods, we evaluated the presence of -1/2 (trefoil-like) and +1/2 (comet-like) defects (schematized in figure 4.2.17C).

As shown in the representative phase contrast images reported in figure 4.2.17B, we found both -1/2 and +1/2 defects in the area in which the bud was arising. We noticed that the same defects were already visible in the monolayer before the arising of mature buds (figure 4.2.17B, first panel).

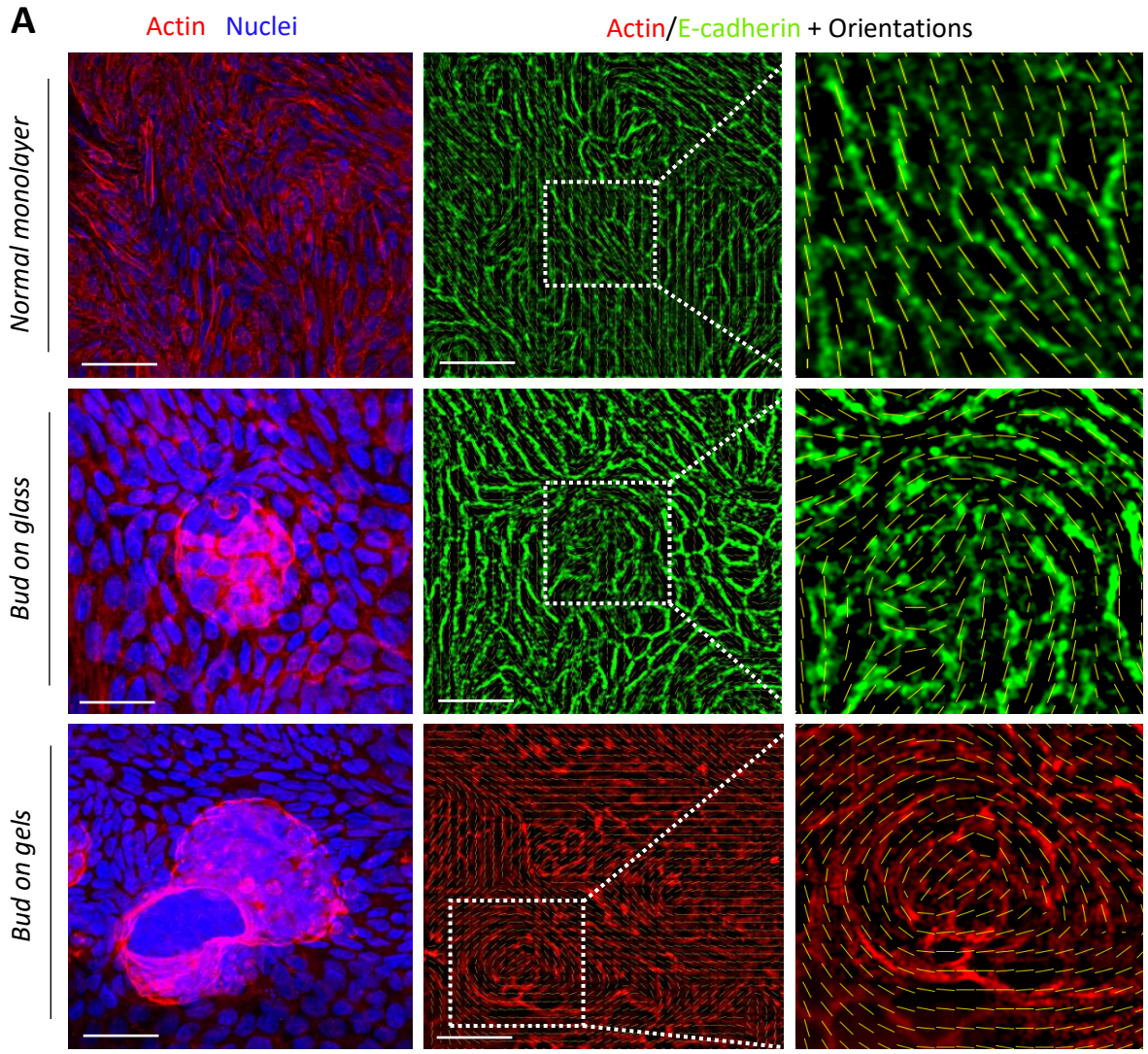


***Figure 4.2.16.*** *(A) Representative confocal images showing the different cell orientations (in yellow) in LS513 epithelia without buds vs. budding monolayer grown on glass and on 30 kPa gels. Panels on the left are MAX projections of apical z-stacks, while panels in the middle column represent MAX projections of basal z-stacks. Panels on the right are close-ups of the area framed by dotted squares. Nuclei are labelled in blue, Actin is labelled in red and E-cadherin in green. Scale bars: 50 µm. N= 3 experiments.*

We then wanted to understand if we could detect a specific pattern of -1/2 or +1/2 defects before and during the formation of the bud, in the monolayer region that would bud and in the surrounding epithelium. Ideally, the identification of a unique pattern of defects, could serve as a predictor of the areas in which the bulging structures would arise. Since both the +1/2 and -1/2 defects found in the monolayer with our customized code were highly motile and highly fluctuating in time, defects were not plotted individually, but they were overlapped in time as heatmaps, as described in section 3.10.2 of Materials and Methods.

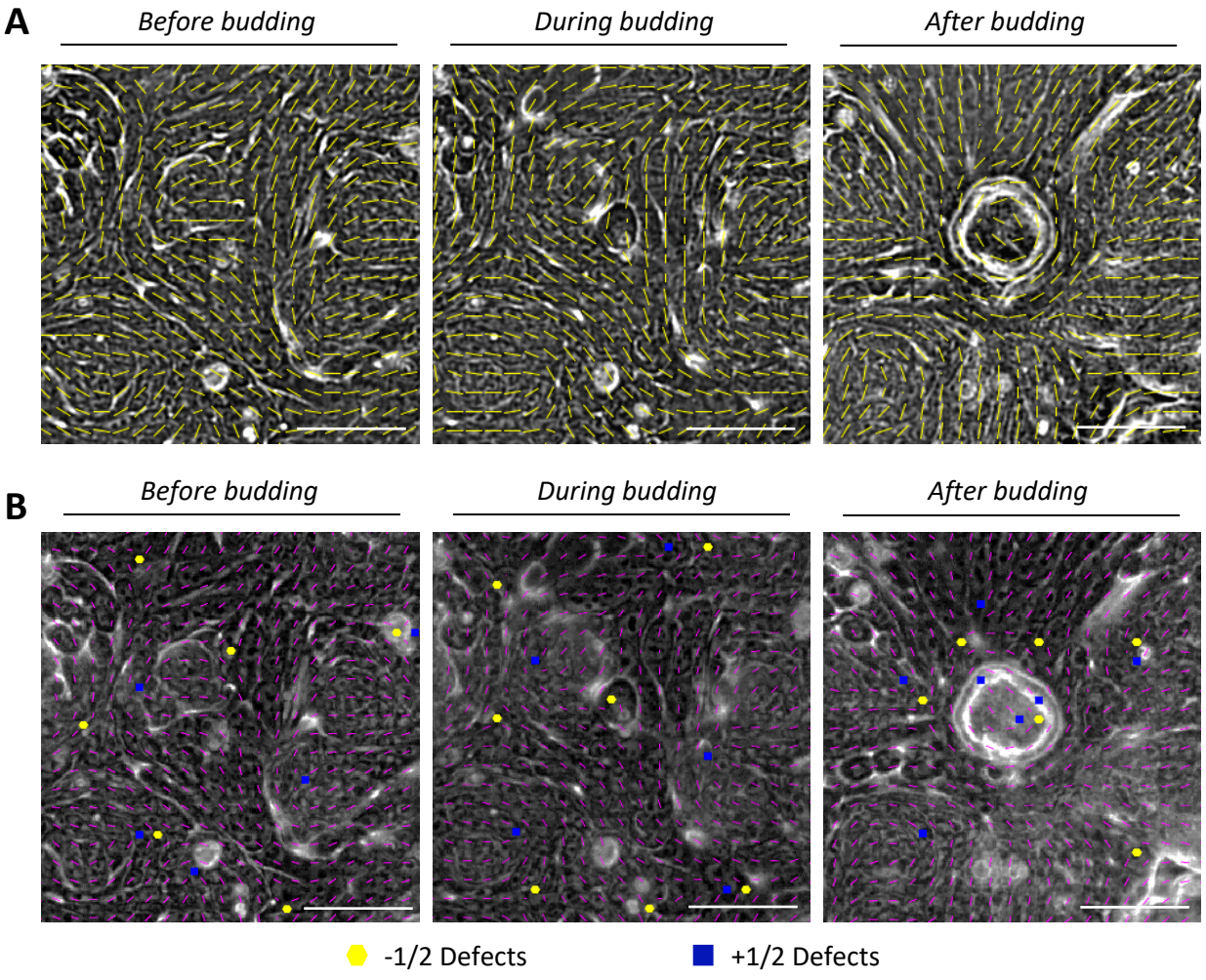

***Figure 4.2.17.*** *(A) Representative phase contrast time-lapses and cell orientations (in yellow) of L513 epithelia grown on 30 kPa PAA hydrogels before, during and after bud formation. (B) Cell orientations (in violet) and topological defects of the same time-lapses shown in (A). Yellow hexagons: -1/2 defects, blue squares: +1/2 defects. Scale bars: 50 µm. N= 2 experiments. (C) Schematic representation of the most common defects found in proximity of buds: -1/2 trefoil-like defects and +1/2 comet-like defects.*

Since we were interested in understanding if defects were present prior to the formation of fully formed buds, we considered only the time-lapses 24 hours before the appearance of mature bulging structures. The resulting graphs are heatmaps where x and y depict the space components of the monolayer regions analysed and the colour displays the total charge of topological defects, a numerical indicator describing the change in the orientation of cells around a given point.

As shown in the representative heatmaps in figure 4.2.18A, this analysis permitted to identify that, those monolayer sub-regions in which a bud would appear, were displaying a 'cloud' of +1/2 defects (right panel), while no peculiar pattern of defects was present in non-budding areas (left panel). To confirm that defects were present in budding monolayers even before buds' emergence, we measured the topological charge in the monolayer 24 hours before the formation of a mature bud and we plotted it with respect to bud centroid, as described in the Materials and Methods, section 3.10.3. As depicted by the representative kymograph in figure 4.2.18B, in the 24 hours prior to mature bud emergence, the topological charge density was already high in the monolayer region where the bud centroid would then be located.

To understand how the defects were disposed with respect to buds, we plotted all the -1/2 and +1/2 defects found in different budding regions in a graph in which the x component is the distance from bud centroids once the bud is mature, and y is the density of total defect charge (figure 4.2.18C). As negative control, we selected monolayer regions in which no bud was found, over a time-lapse of 48 hours. As shown by this graph in figure 4.2.18C, the total charge density peaks on the centroid of buds, while it rapidly decreases going further from this point. The defect charge density was strikingly higher in all the budding areas analysed, with respect to non-budding portions of the monolayer (box-plot graph, figure 4.2.18D). Overall, this analysis confirmed that the presence of topological defects could be used as predictors of areas where buds would emerge.

Being the total charge positive, we reasoned that +1/2 defects are the main ones to be located in close proximity to the bud centroid.

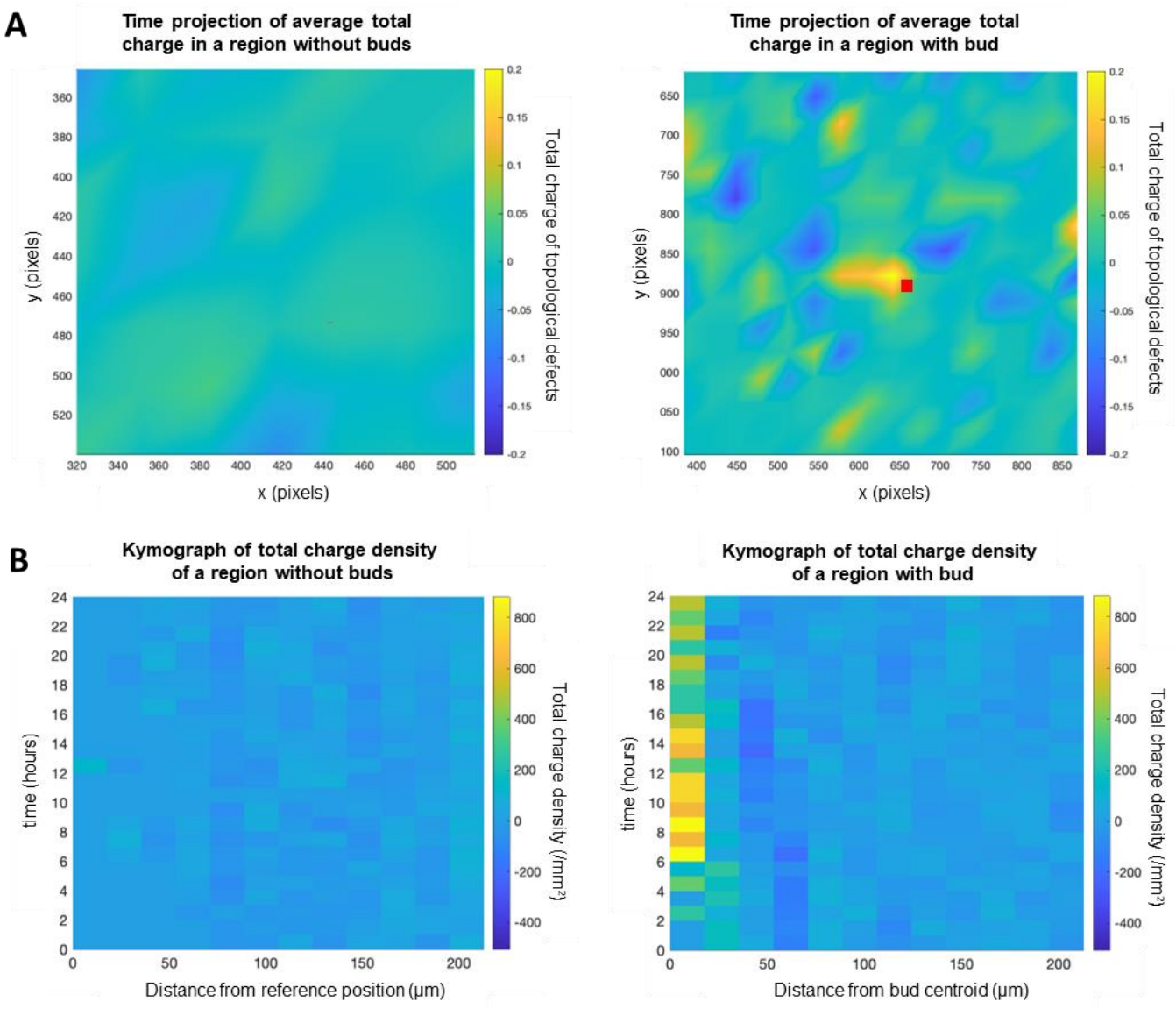

***Figure 4.2.18.*** *(A) Representative heatmaps displaying defects charge in monolayer with buds vs. normal monolayer in 30 kPa gels. Red square= centroid location once bud is fully formed. (B) Representative kymographs showing total charge density (on mm$^2$) in a region without a bud vs in a budding region in 30 kPa gels. (C) Total charge density (on mm$^2$) of regions with buds vs regions without bud. In areas with bud, the reference position corresponds to the average centroid location of 20 buds, in control regions it refers to the centre of the ROI. Red dotted line: average bud radius (25 µm). Graphs represent means ± SEM of total charge density of 20 regions with buds and 6 regions without bud. (D) Box plot of total charge density on the reference position shown in (C) in budding zones vs not budding zones. Mann-Whitney test, **=p≤0.01. N= 2.*

Moreover, as the total charge becomes negative just beyond the average location of bud contours once the structure is fully formed (red spotted line, figure 4.2.18C), we thought that this could be due to the presence of more -1/2 defects, with respect to the +1/2 ones.

Therefore, to further characterize the contribution of trefoil-like and comet-like defects at budding regions, we quantified the absolute charge, the total number of positive defects and the total number of negative defects (Figure 4.2.19 A-C*).* As shown by graph in figure 4.2.19A, the absolute charge density is higher at buds' centroid, and it decreases moving away from this point. This means that, regardless of the sign, defects are dramatically more where buds centroid are located, in comparison to other regions of the monolayer.

When we quantified the total number of positive (4.2.19B) or negative defects (4.2.19C), we noticed that, as hypothesised, positive defects peak at bud centroid and rapidly decrease moving further from it, while negative defects are slightly more at buds' border and only gradually decrease in number moving from this zone. As expected, the total charge of monolayer regions without buds is completely different to the one of budding regions, as it is always around 0 (4.2.18C-D).

Together, these results show that the formation of buds is marked by the presence of specific topological defect patterns.

Having demonstrated that MAPK cascade inhibition causes budding reduction in LS513 cells (Results section 4.2.3), we then wanted to evaluate if MAPK pathway inhibition could have any effects on topological defects formation. We indeed wanted to assess whether the reduction in bud number in LS513 epithelia treated with MAPK inhibitors could also correlate with a decrease of topological defects arising in the monolayer.

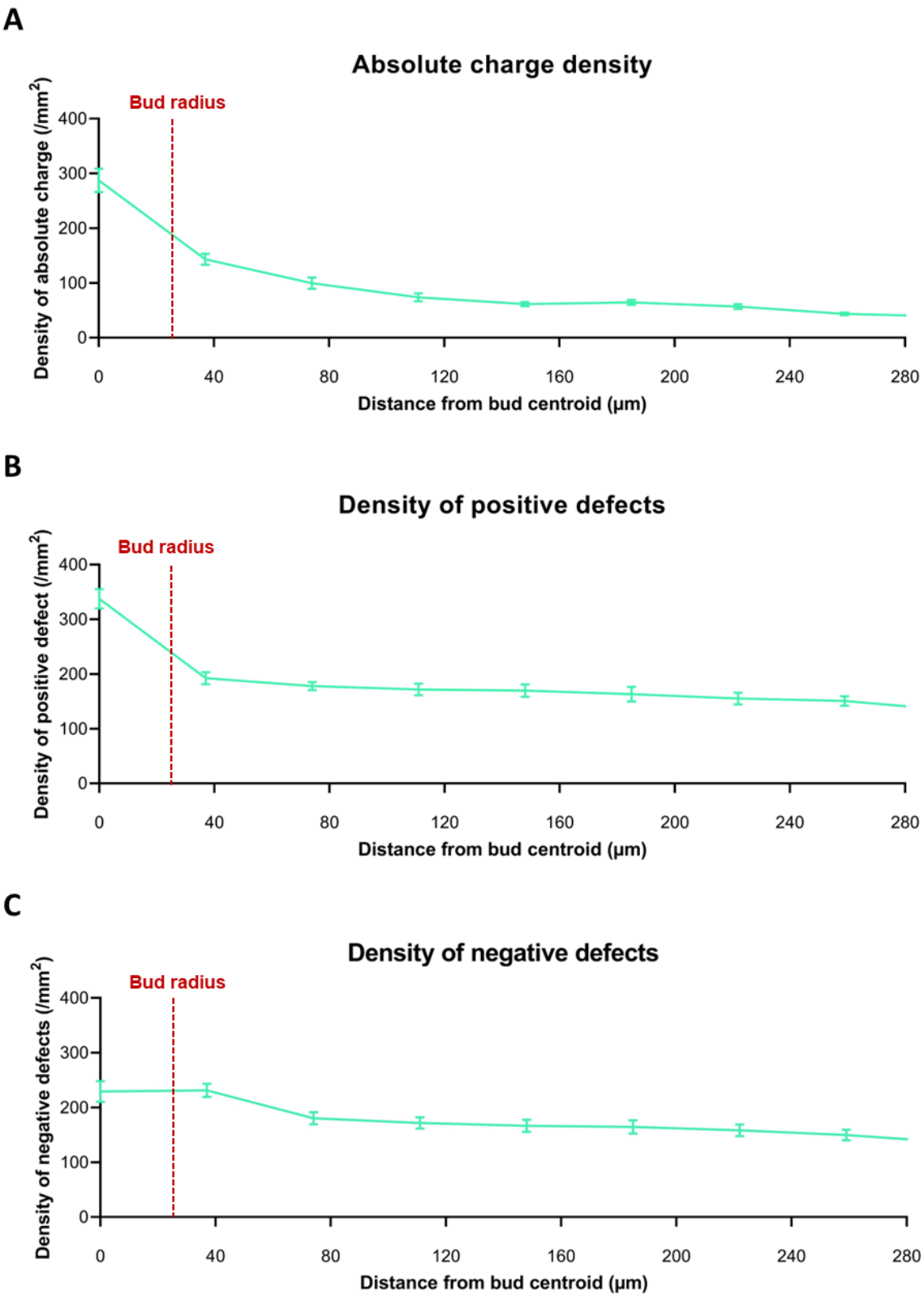


***Figure 4.2.19.*** *(A) Absolute charge density (on mm$^2$) in budding regions on 30 kPa gels. B) Total number of positive defects (on mm$^2$) in budding regions on 30 kPa gels. (C) Total number of negative defects (on mm$^2$) in budding regions on 30 kPa gels. The reference positions (0) correspond to the average centroid location of buds (averaged in time and in space). Red dotted line: average bud radius (25 µm). Graphs shown represent means ± SEM of 20 budding regions.*

To do that, we imaged for 3 days LS513 cells plated on 30 kPa gels and treated with SCH or with Trametinib, and we analysed the local cell orientations with OrientationJ plugin.

In our experimental setting, LS513 cells treated with Trametinib had a high mortality and several were detaching from the monolayer, so the orientations analysis was not reliable. Therefore, just the results obtained for cells treated with SCH are reported here. As shown in figure 4.2.20A, non-treated cells (image on the left) presented the typical orientations pattern found in flat gels prior to budding. However, after just 24 hours of treatment with SCH, the same cells already displayed fewer topological defects. By 2 days of treatment, cells were almost completely aligned and only few discontinuities in the orientation field were visible in the monolayer.

We then overlapped all the -1/2 and +1/2 defects appearing in the LS513 epithelia in the time-lapses before and after MAPK inhibitor treatment and we measured the total topological charge. Figure 4.2.20B shows a representative heatmaps displaying topological defect charge in the same epithelium sub-region before and after SCH treatment*;* interestingly, the topological defects present in the monolayer before SCH addition dramatically decreased in number after drug treatment*.* This finding is further confirmed by kymographs, as the one displayed in figure 4.2.20C, that show that topological charge density is almost completely cleared after MAPK inhibition (6-8 hours from time 0).

We also quantified the total charge density in various monolayer regions before and after SCH treatment (figure 4.2.20D). As shown by this graph, the total charge density peak, that is present before the addition of SCH, is almost completely flatten after 48 hours of treatment. The results reported in figure 4.2.20 show that, after SCH treatment, the whole LS513 epithelium looks like non-budding areas (4.2.16A and 4.2.18A-C).

Overall, these results show that MAPK inhibition causes topological charge and defects reduction in LS513 epithelia.

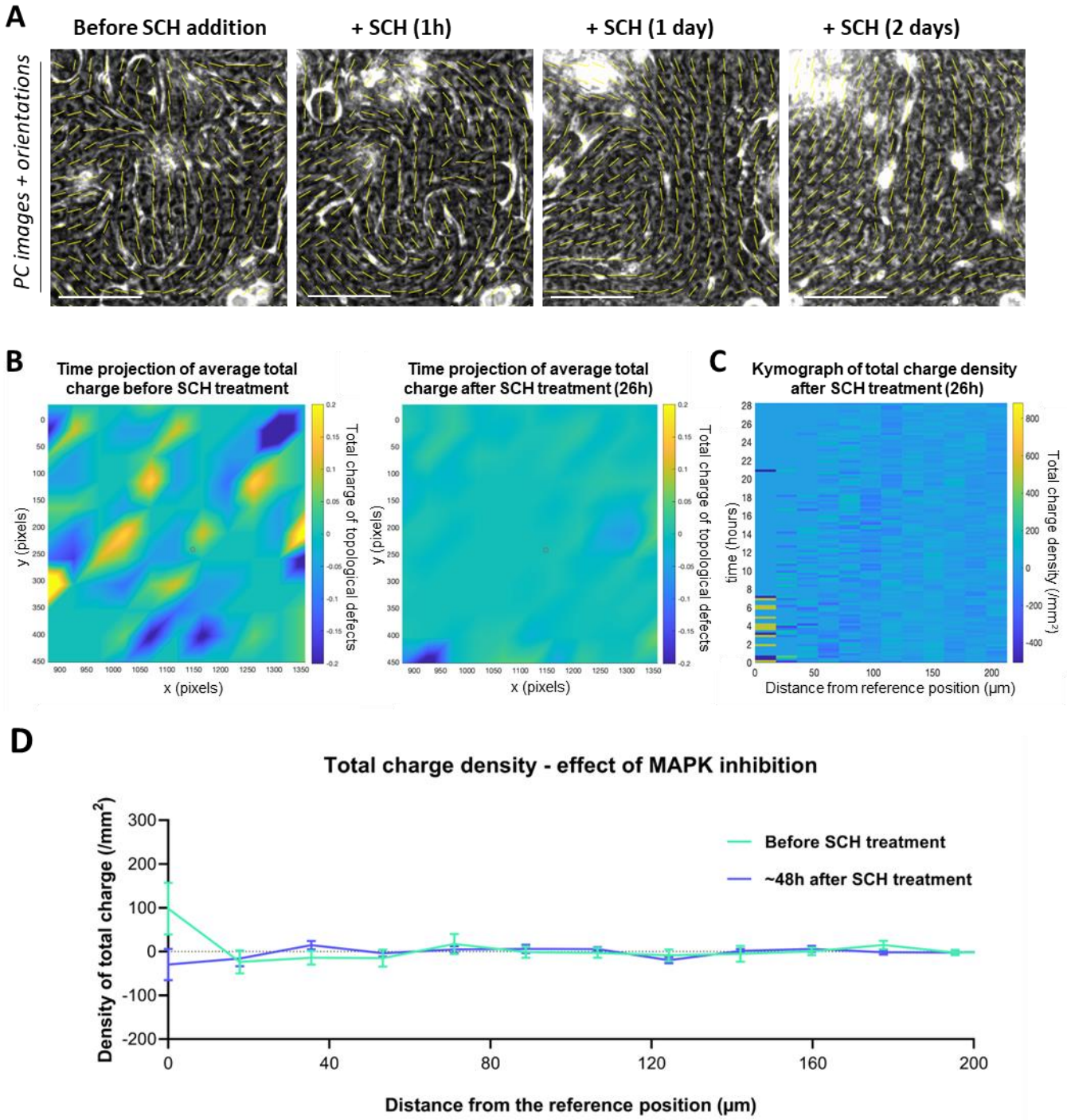


***Figure 4.2.20.*** *(A) Representative phase contrast images and orientations (in yellow) of LS513 cells plated on 30 kPa gels, before and after SCH addition. Scale bars: 50 µm. (B) Representative heatmaps displaying total defect charge of the same monolayer region shown in (A) before (2 hours) and after addition of SCH (26 hours). Red circles represent the centre of the ROI. (C) Representative kymographs showing total charge density (/mm$^2$) of LS513 epithelia treated with SCH for 26 hours, after 2 hours of normal culture. (D) Comparison of total charge density (on mm$^2$) of monolayer regions before and after SCH treatment. The reference position corresponds to the centre of the ROI. Graphs represent means ± SEM of total charge density of 8 regions of monolayer before and after SCH addition.*

*4.2.6 Topographical-induced cellular alignment causes budding impairment in LS513 epithelia*

Since we showed that budding areas are characterised by high density of topological defects, we hypothesised that forced cellular alignment could impair defects formation and therefore reduce budding events. Cells were thus plated on micro-structured gels with squared ridges of 2 µm in width and 1 µm in height (as displayed by the schematics in figure 4.2.21A) and having the same stiffness of the flat ones (3, 12, 30 and 60 kPa). Like for the flat gels, we took 3-day-videos of LS513 cells grown on these substrates, starting from a minimum confluence of 80-90%.

Figure 4.2.21B shows phase contrast images at different timepoints of cells growing on micro-structured 30 kPa gels and aligning on top of the grooves. To verify if this alignment was real and not biased by the accumulation of cellular material inside the grooves, we also imaged LS513 cells grown on 30 kPa micro-structured gels with confocal microscopy. As shown by the second panel in figure 4.2.21.C, Actin looks aligned in the same direction of the grooves, as depicted by the grey dotted line, that points out to parallel Actin filaments, disposed at exactly 2 µm of distance.

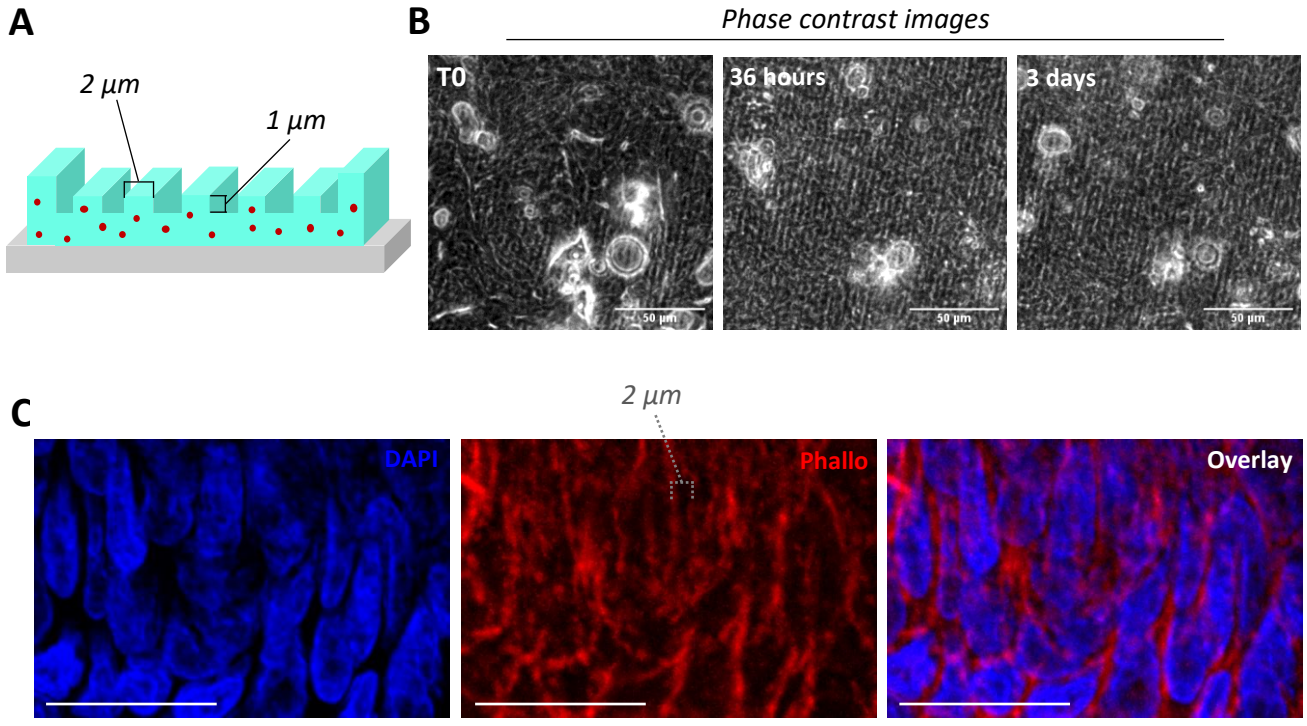

***Figure 4.2.21.*** *(A) Schematics showing a micro-structured PAA hydrogel. Red dots represent fluorescent beads dispersed in the PAA gel. (B) Representative phase-contrast images showing LS513 cells grown on 30 kPa grooved gels. Scale bars: 50 µm. (C) Representative confocal microscopy images, displaying LS513 cells aligned on the micro-structured grooves. Nuclei are labelled in blue and Actin is labelled in red. Scale bars: 20 µm.*

We then quantified the number of buds produced by LS513 epithelia grown for up to 14 days on these micro-structured hydrogels, with respect to flat gels with the same stiffness. To quantify the total number of buds for each condition, we imaged the whole monolayer (figure 4.2.22A) and counted the bulging structures employing phase contrast, DAPI, Phalloidin and Ezrin signal, as described in section 3.8 of Materials and Methods. Results are shown in figure 4.2.22B; as displayed by this graph, bud formation on grooved gels was significantly lower than in flat hydrogels, even for stiffer conditions (30 and 60 kPa). Therefore, culturing the LS513 cells on micro-structured gels with grooves impairs budding, regardless of substrate stiffness.

We then wanted to evaluate if this budding impairment could be due to vorticity and topological defects reduction. Thus, as we previously assessed the high vorticity of budding LS513 epithelia and the presence of velocities swirls in correspondence to the forming buds (figures 4.2.14 and 4.2.15), we also wanted to characterise the overall cellular vorticity on grooved and on flat gels. Indeed, we would expect vorticity to be lower in epithelia grown on grooved gels, which are more constrained, with respect to epithelia plated on flat hydrogels.

Therefore, we analysed the videos taken on 30 kPa flat or grooved gels with PIVlab software in Matlab and we plotted the velocity vorticity of the cells as heatmaps. As depicted by the representative heatmaps and the violin dotted plots in figure 4.2.23, the vorticity is significantly lower in grooved gels, in comparison to flat gels, especially after 3 days of experiment.

Indeed, while at the beginning of the video (T0), the vorticity of cells cultured on micro-structured hydrogels was just slightly lower than the one on flat gels, after only 36 hours it was significantly reduced and after 3 days it was almost completely null. As depicted by the top panels in figure 4.2.23A, LS513 epithelia grown on flat 30 kPa gels, present several whirling spots (red and dark blue areas), especially at the beginning of the video and after 36 hours.

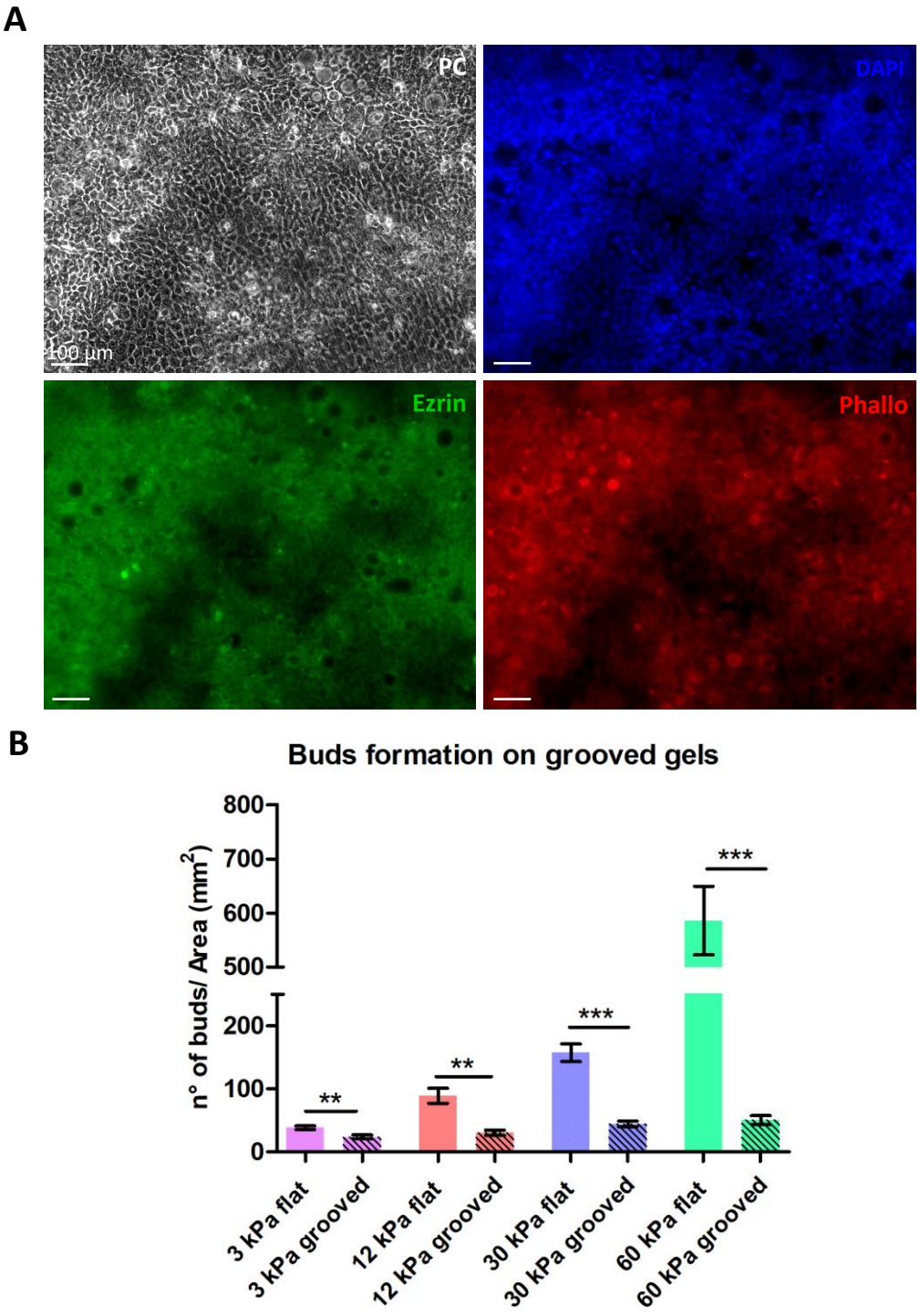


***Figure 4.2.22.*** *(A) Representative phase contrast and epifluorescence images, displaying a big portion of LS513 monolayer grown on 30 kPa grooved gels and showing no budding structures. PC: phase contrast, Nuclei are labelled in blue, Actin is labelled in red and Ezrin in green. Scale bars: 100 µm. N= 3 experiments. (B) Quantification of bud formation at different stiffness. Bud counts were normalized for a surface of 100 mm². Results are presented as mean ± standard error of the mean (SEM). p<0.05 = (*), p<0.01 = (**) and p<0.001 = (***),* t-tests. *N= 3 experiments.*

Even if the overall vorticity on flat gels clearly decreases after 3 days of video, it is still possible to distinguish several swirling points, that are almost completely absent on grooved gels.

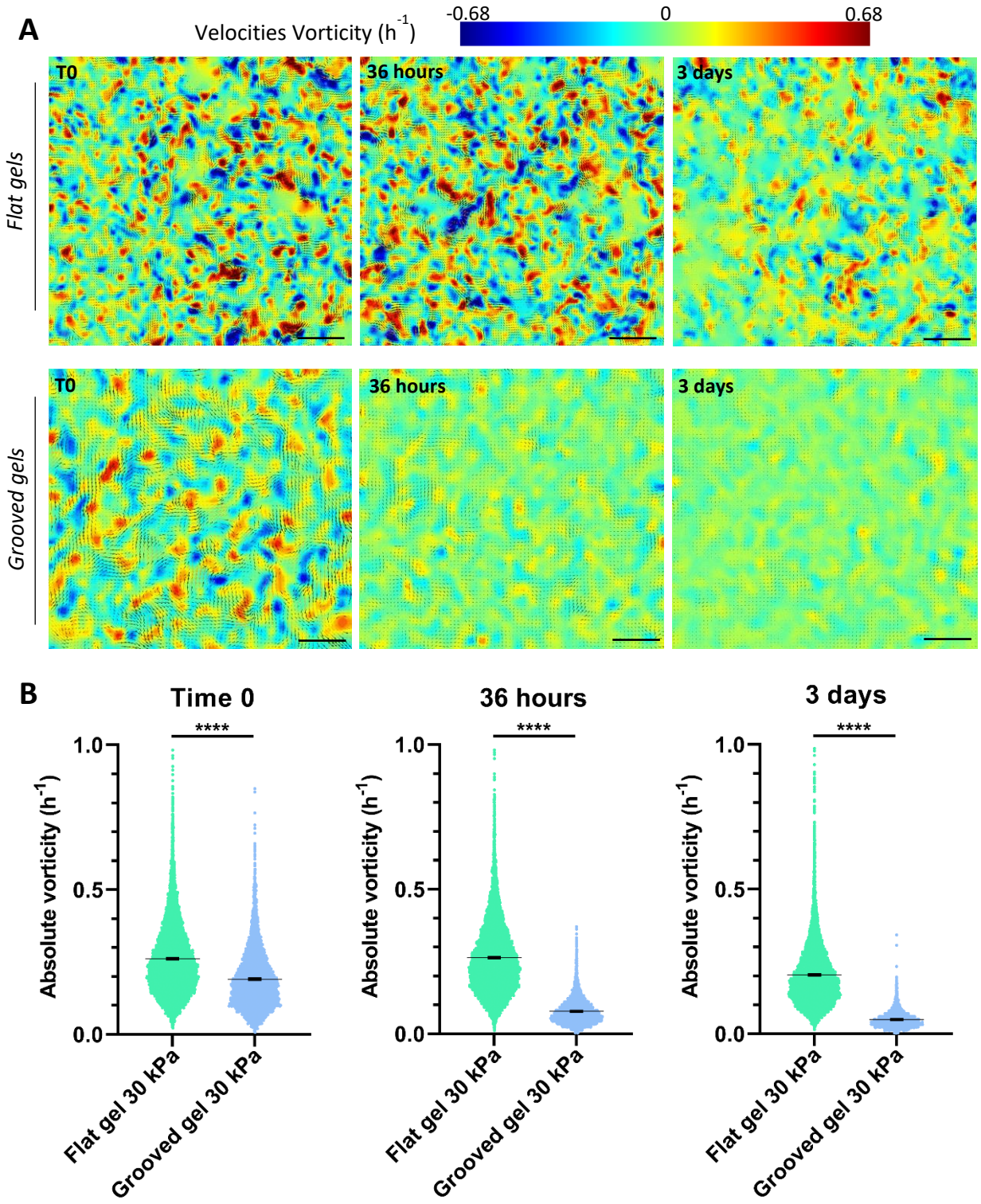

***Figure 4.2.23.*** *(A) Heatmaps displaying velocities vorticity of LS513 cells grown on flat gels or on grooved 30 kPa gels and imaged for up to 3 days. Scale bars: 100 µm. (B) Violin dotted plots showing the absolute value of vorticity of LS513 grown on flat gels or on grooved 30 kPa gels, at t0, 36 hours and 3 days. Each dot corresponds to the absolute vorticity of a singular interrogation window (roughly a cell). Thin black line: mean value of velocity magnitude. Thick black line: standard deviation of the mean (SEM). N= 3 experiments.*

We also quantified the velocities magnitude of LS513 cells grown on flat gels and on micro-grooved ones. As shown by the representative heatmaps and the violin dotted plots in figure 4.2.24, as vorticity, velocity magnitude is significantly lower in grooved gels, in comparison to flat gels, especially after 3 days of experiment. Indeed, at this time point the velocity magnitude of cells grown on micro-structured gels is almost null.

These results indicate that growing LS513 cells on micro-structured gels with grooves highly reduces the motility and the vorticity of these cells.

We then wanted to characterize the orientations and the topological defects of LS513 cells grown on these micro-structured substrates. Indeed, we wanted to evaluate if growing these cells on grooved gels was sufficient to significantly reduce the topological aberrations. As shown by the cellular orientations overlapped on phase contrast images (Appendix, figure 8.1.4), after few hours of video, the cells were still not completely aligned, and they were forming some topological defects (red asterisks). However, after 12 hours some defects had already disappeared and, by 2 days of video, all the cell orientations were almost completely aligned. This result was further confirmed by confocal microscopy imaging, followed by analysis of the orientations of LS513 cells grown on grooved 30 kPa gels for up to 2 weeks. As showed by the representative images in 4.2.25A, no abrupt changes in cell orientation were visible in LS513 epithelia grown on micro-structured hydrogels.

Later, we wanted to evaluate if, also on LS513 monolayers grown on micro-structured gels, we could find the peculiar patterns of topological defects observed in epithelia grown on flat hydrogels. As for flat gels, we evaluated the presence of -1/2 (trefoil-like) and +1/2 (comet-like) defects, employing a customized code in Matlab (Material and Methods, section 3.10.1). Also in this case, defects were not mapped individually, but they were overlapped in time. Thus, all the -1/2 and +1/2 defects appearing on LS513 epithelium were superposed in time and plotted in heatmaps where x and y corresponds to the spatial coordinates of the sub-regions analysed and the colour displays the total charge of topological defects.

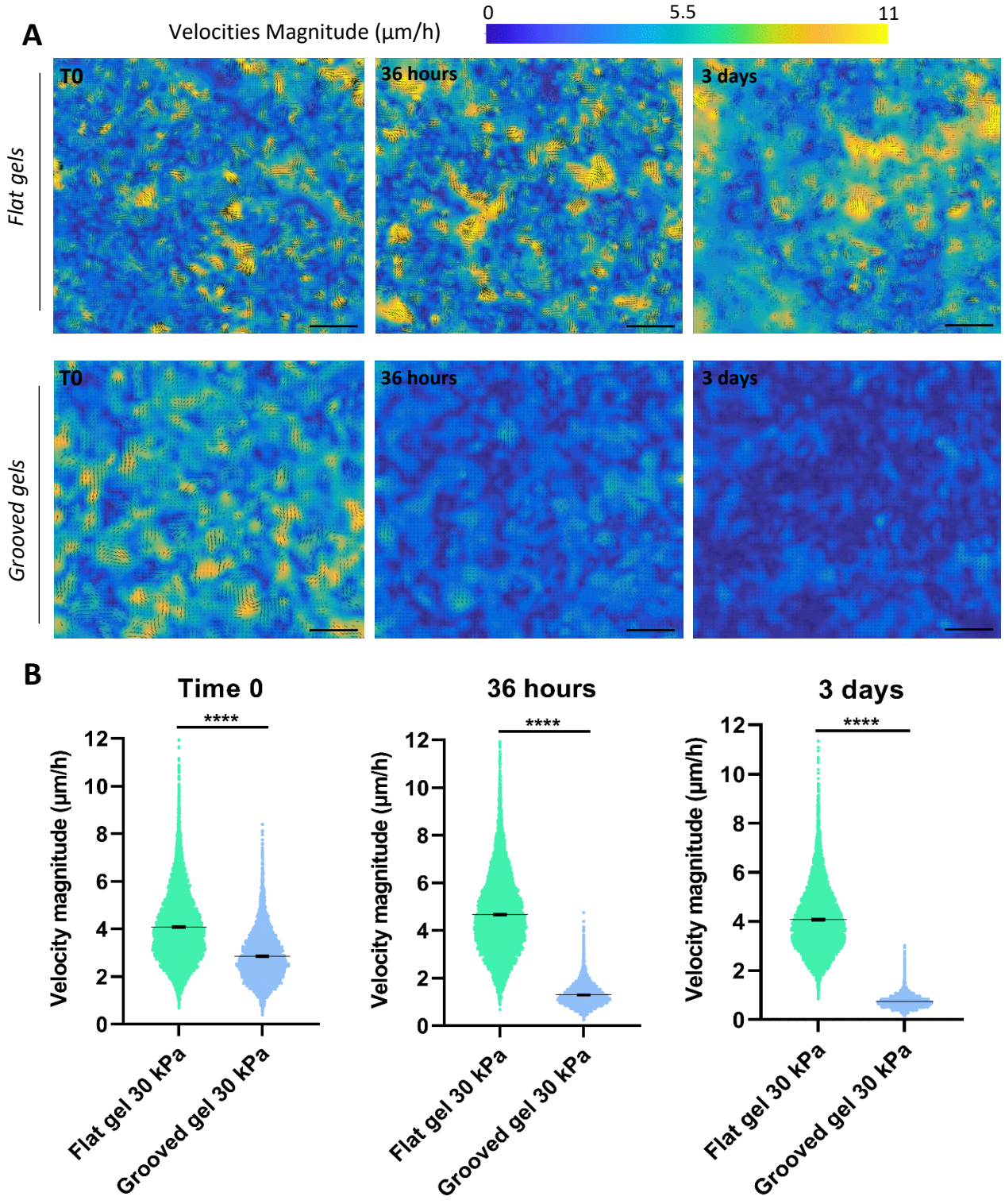


***Figure 4.2.24.*** *(A) Heatmaps displaying velocities magnitude of LS513 cells grown on flat gels or on grooved 30 kPa gels and imaged for up to 3 days. Scale bars: 100 µm. (B) Violin dotted plots showing velocity magnitudes of LS513 grown on flat gels or on grooved 30 kPa gels, at t0, 36 hours and 3 days. Each dot corresponds to the velocity magnitude of a singular interrogation window (roughly a cell). Thin black line: mean value of velocity magnitude. Thick black line: standard deviation of the mean (SEM). Please note that the SEM of velocity magnitudes of cells grown on grooved gels at 3 days was so low that it was impossible to visualize it in the graph. N= 3 experiments.*

As depicted by the representative heatmaps in figure 4.2.25B, defect charge was lower in hydrogels with grooves than in flat ones. Similarly, kymographs, as the representative one displayed in figure 4.2.25C, show that topological charge density of LS513 cells is almost completely null on grooved 30 kPa gels. We also quantified the total charge density of various micro-structured regions and compared it to the one of flat hydrogels having the same stiffness (figure 4.2.25D). As shown by this graph, the total charge density of aligned cells is strikingly lower that the one of LS513 cells plated on flat substrates. These results confirm that LS513 cells grown on micro-structured gels present less topological defects.

Overall, these results show that topographical-induced cellular alignment causes topological defects and vorticity reduction, as well budding decrease in LS513 epithelia.

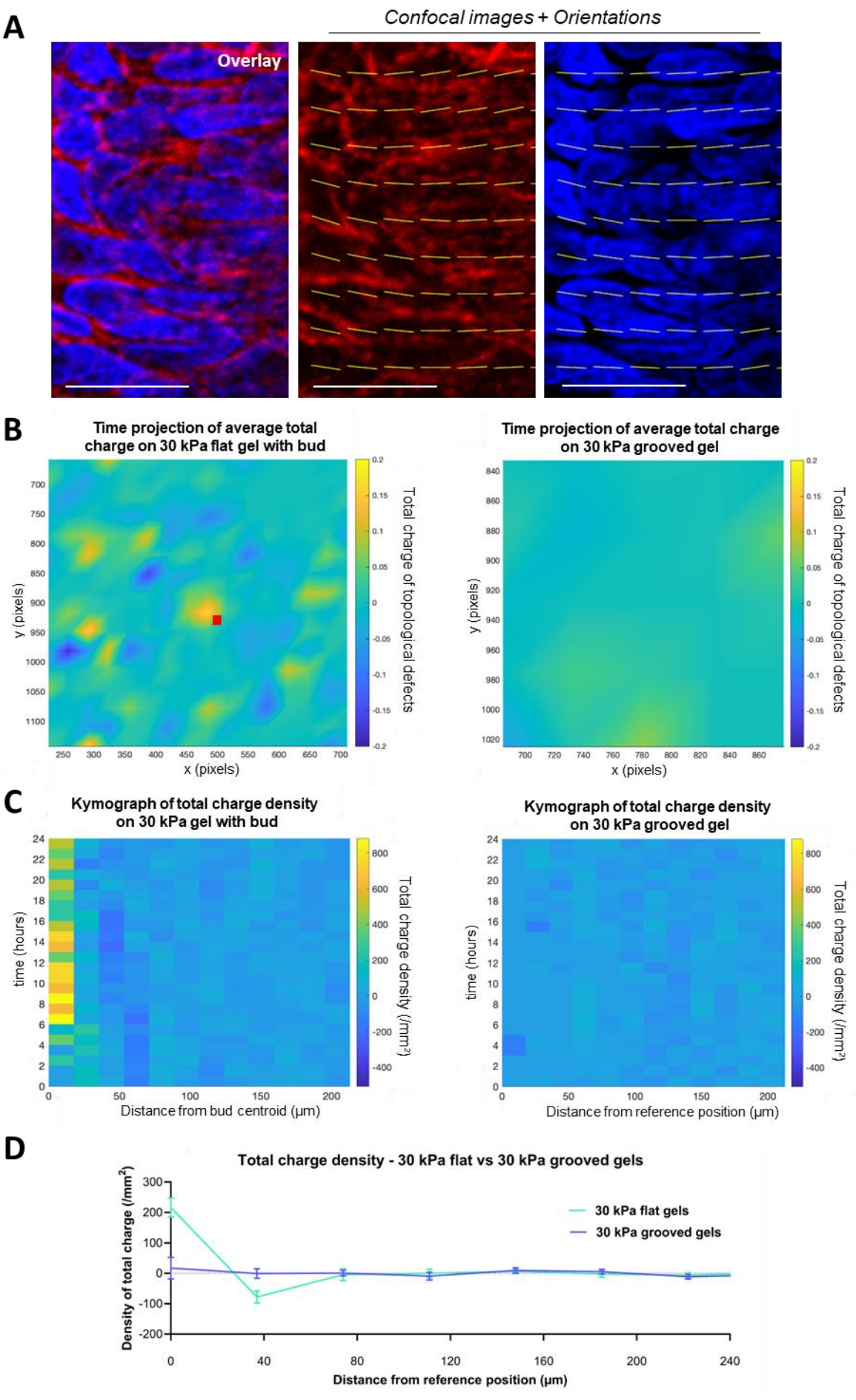
A
Confocal images + Orientations
Overlay
B
Time projection of average total charge on 30 kPa flat gel with bud
y (pixels)
x (pixels)
Total charge of topological defects
Time projection of average total charge on 30 kPa grooved gel
y (pixels)
x (pixels)
Total charge of topological defects
C
Kymograph of total charge density on 30 kPa gel with bud
time (hours)
Distance from bud centroid (µm)
Total charge density (/mm²)
Kymograph of total charge density on 30 kPa grooved gel
time (hours)
Distance from reference position (µm)
Total charge density (/mm²)
D
Total charge density - 30 kPa flat vs 30 kPa grooved gels
Density of total charge (/mm²)
Distance from reference position (µm)
30 kPa flat gels
30 kPa grooved gels

***Figure 4.2.25.*** *(A) Representative confocal microscopy images and cell orientations (in yellow), displaying LS513 cells aligned on the micro-structured grooves. Nuclei are labelled in blue, and Actin is labelled in red. Scale bars: 20 µm. (B) Representative heatmaps displaying total defect charge in LS513 epithelia grown on 30 kPa flat gels (on the left) and on 30 kPa grooved gels (on the right). Red square= centroid location once bud is fully formed. (C) Representative kymographs showing total charge density (/mm$^2$) on 30 kPa flat gel vs on a 30 kPa micro-structured gel. (D) Total charge density (on mm$^2$) of 30 kPa flat gels vs 30 kPa grooved gels. In flat gels, the reference position corresponds to the average centroid location of buds, in grooved gels it refers to the centre of the ROI. Graphs represent means ± SEM of total charge density of 20 regions for flat gels and 10 for grooved ones.*

### 4.3 Mechanical characterization of spontaneous malignant retraction in LS174T epithelia

*4.3.1 LS174T cells as a model of dewetting in confined patterns*

In the previous section, we have demonstrated that LS513 cells are an excellent model to study budding *in vitro*. On the contrary, as we assessed in section 4.1, LS174T cells could barely bud when cultured as monolayers. However, since we observed retraction of a portion of the epithelium in experiments with LS174T cells (section 4.1, figure 4.1.5B), we wondered if they could be a good model to study another type of morphological 2D to 3D transition associated to malignant transformation, namely the spontaneous retraction of whole epithelia.

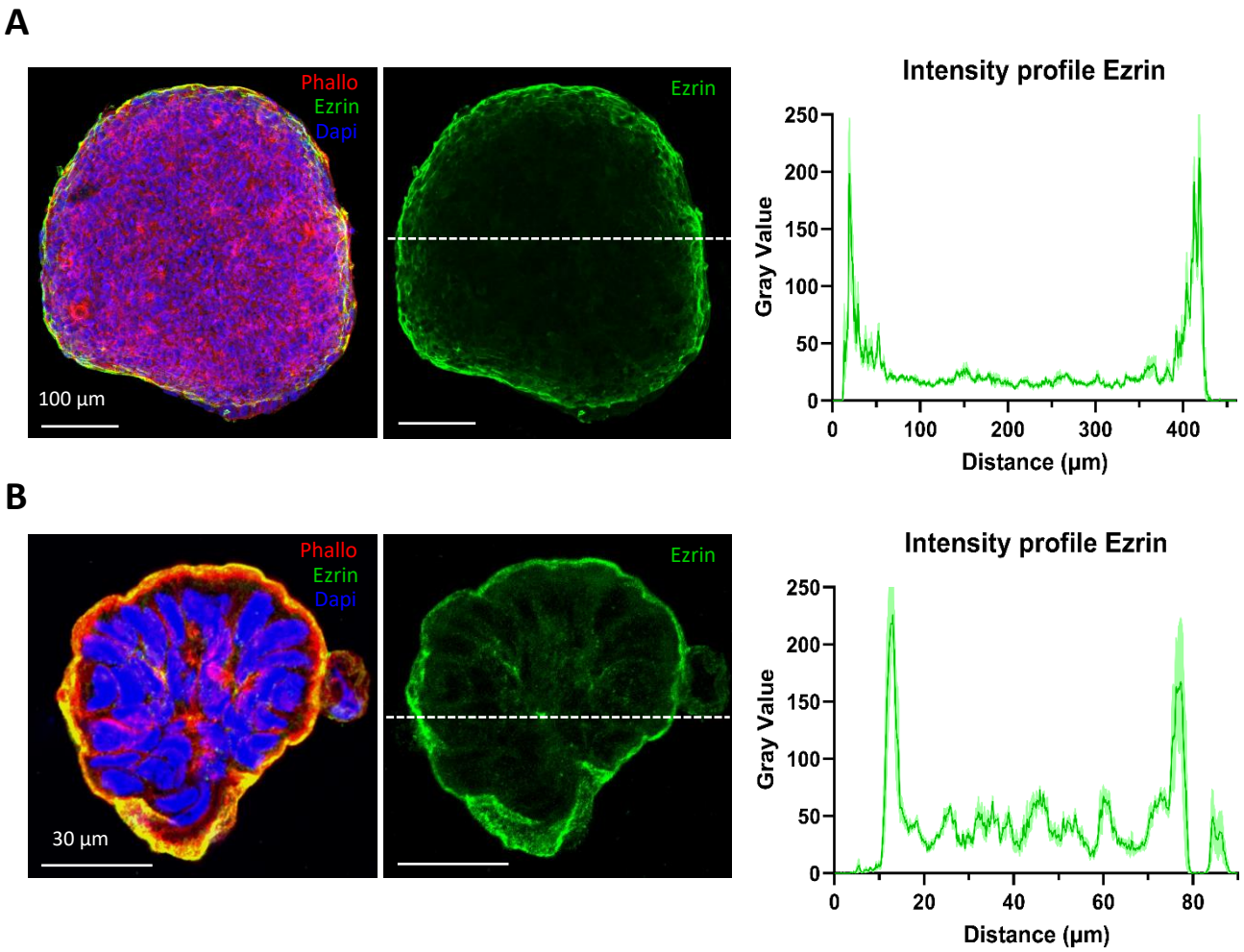

***Figure 4.3.1.*** *(A) Confocal microscopy images and intensity profiles for Ezrin of a representative 400-µm pattern of LS174 cells grown on 12 kPa PAA hydrogels. Nuclei are labelled in blue, Actin is labelled in red and Ezrin in green. Scale bars: 100 µm. The graph plots the average value of ezrin intensity along the white dashed line and in other samples. N= 2 experiments. (B) Confocal microscopy images of middle z-stacks MAX projections and intensity profile for Ezrin of a bud arising from LS513 epithelia grown on 12 kPa PAA hydrogels. The graph shows the average value of ezrin intensity along the white dashed line and in other samples. Nuclei are labelled in blue, Actin is labelled in red and Ezrin in green. Scale bars: 30 µm. N= 3 experiments.*

This process, which has been framed in the context of dewetting, consists of the retraction of confined flat circular monolayers leading to the formation of 3D spheroid-like structures. Such phenomenon has been previously described by Perez and colleagues in MDA-MB-231[64] and by our laboratory in MCF10A epithelia[39] but has never been evaluated using LS174T as model.

First, to assess the spontaneous retraction of LS174T epithelia and the subsequent formation of compact 3D cell aggregates, we confined these cells employing micropatterning technique, as described in the methods.

We employed microfabricated circular stencils that resulted in LS174T islands on 12 kPa polyacrylamide gels with an area of 108.380 ± 1.401 $\mu m^2$ (figure 4.3.2), much bigger than LS513 buds grown on 12 kPa polyacrylamide gels (average surface of 3.560 ± 472 $\mu m^2$), but comparable to the circular monolayers employed in previous studies[39],[64]. Next, we looked for polarity markers, that, as we reported for LS513 cells (figures 4.1.6, 4.2.1, 4.2.3 and 4.2.4), are present in the budding process. As depicted by the z-stacks and the intensity profiles in figure 4.3.1.A, LS174T confined islands show an Ezrin expression profile similar to the one of LS513 buds.

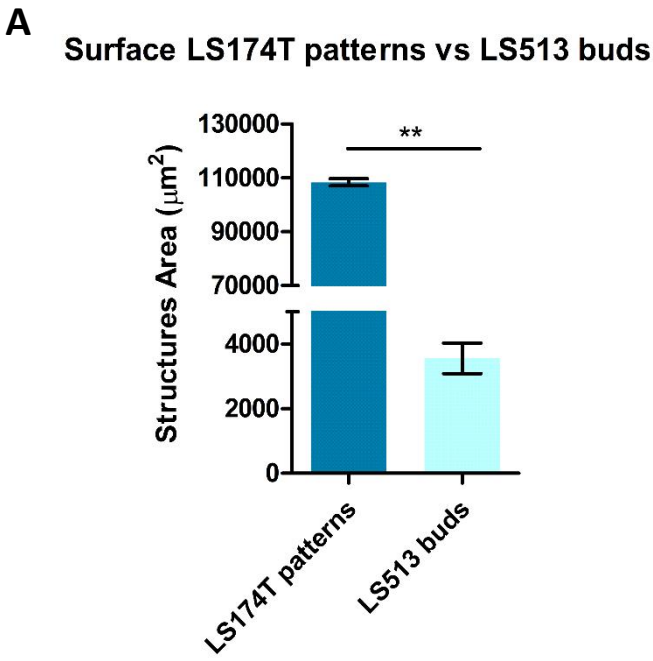


***Figure 4.3.2.*** *(A) Quantification of LS513 buds and LS174T patterns surface on 12 kPa gels. Results are presented as mean ± standard error of the mean (SEM). P<0.01 = (**)*, t-tests, *N= 3 experiments.*

Finally, confined circular patterns of LS174T cells were imaged for minimum 3 days, to monitor if they were indeed able to dewet. Experiments were started once the islands were at least 95% confluent (approximately 24 hours after plating); for simplicity, from now on we will here refer to this time point as T0.

As showed in figure 4.3.3, we observed two types of behaviour: non-dewetting (Figure 4.3.3A) and dewetting epithelia (Figure 4.3.3B). Among 42 patterns analysed in 3 independent experiments, 39 ± 5% dewetted after 30-35 hours of imaging, while 61 ± 5% did not dewet throughout the experiment (figure 4.3.3C). In dewetting LS174T patterns, after approximately 35 hours from T0, the entire monolayer started retracting forming a sort of spheroid-like structure. On the other hand, non-dewetting patterns showed the formation of a thicker peripheral rim of cells (figure 4.3.3A, red arrows).

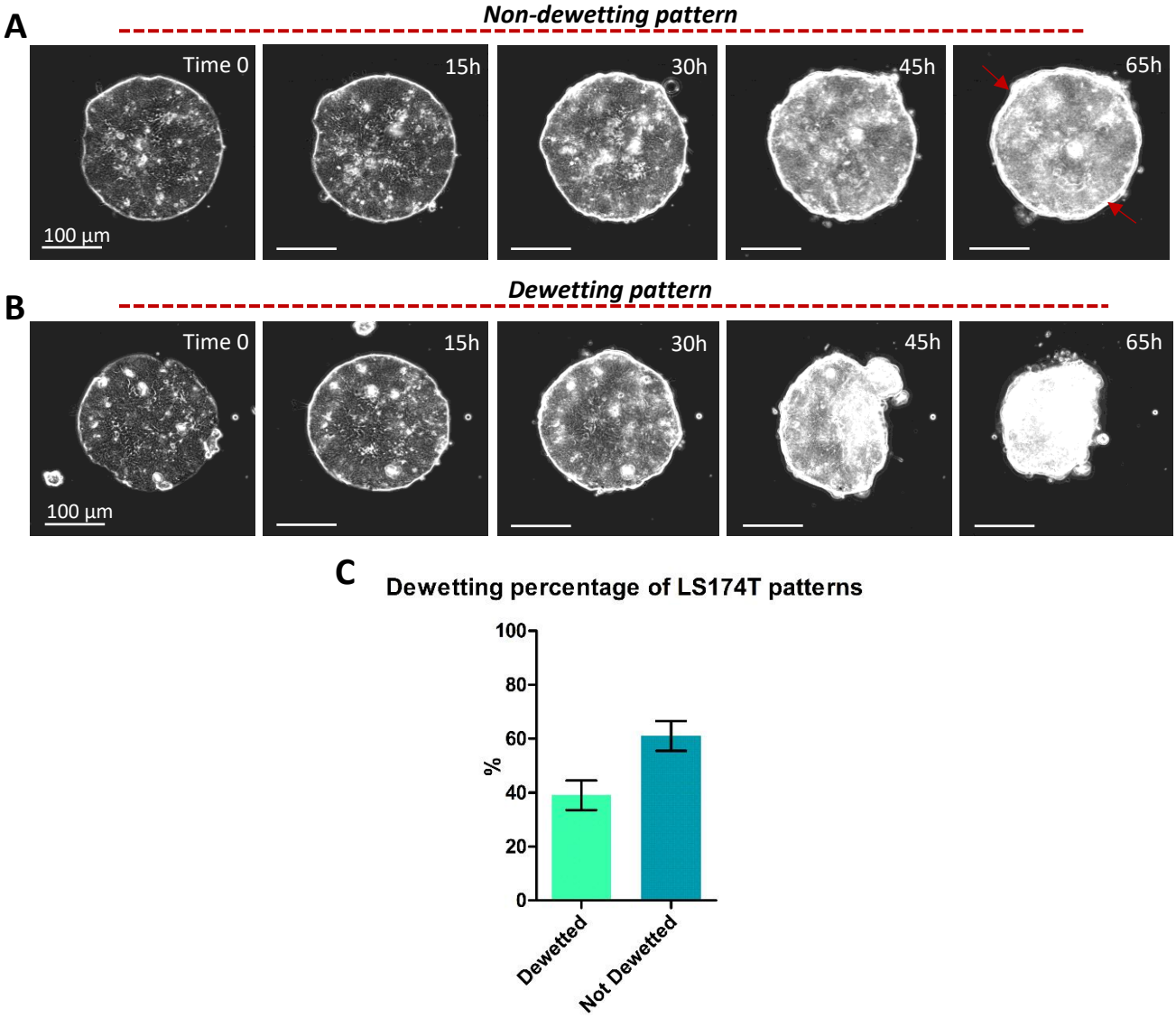


***Figure 4.3.3.*** *(A) Phase contrast time-lapses, showing a representative a pattern of LS174T cells that did not dewet. (B) Phase contrast time-lapses, showing a representative dewetting pattern of LS174T cells grown on PAA gel. Scale bars: 50 µm. (B) Comparison of dewetting percentage in LS174T patterns plate on 12 kPa. Results are presented as mean ± standard error of the mean (SEM). N= 3 experiments.*

*4.3.2 Dewetting of LS174T patterns occurs in a non-symmetric fashion*

We then wanted to characterize the changes happening at the level of the monolayer during dewetting of LS174T patterns. To do so, we imaged the dewetted and the not dewetted patterns at different time-points via Confocal microscopy and we analysed the cellular organization in the z plane orthogonal to the underlying elastic substrate.

Like previously noticed via live imaging (figure 4.3.3), not dewetted patterns maintained their original circular shape throughout the experiment, while the dewetted ones lost their circularity during monolayer retraction (figure 4.3.4A). As displayed in figure 4.3.4B, if imaged in z after around 70 hours post-confluence, both not dewetted and dewetted patterns showed juxtaposition of various layer of cells. However, as previously noticed via live imaging (figure 4.3.3A), not dewetted patterns presented a peripheral rim of cells which was not found in dewetted ones (figure 4.3.4B, white arrowheads). Indeed, dewetted islands showed the same thickness throughout the pattern, while not dewetted islands displayed thicker borders with respect to the centre of the monolayer, that looked thinner (approximately 1-2 layers of cells less). As displayed by the orthogonal sections, this rim was starting to appear already after 48 hours from confluence. Moreover, in dewetted patterns borders were 'lifting', like if they were detaching from the underlaying substrate.

To define the path leading to this 2D-to-3D cellular transformation, we monitored the dewetting process via a set of objective morphological parameters. We compared the morphological properties of dewetted patterns to the ones of not dewetted patterns. Specifically, we quantified surface area, perimeter, axis ratio and eccentricity of each cellular island.

As shown in the top graphs in figure 4.3.5, the area and the perimeter of the dewetted patterns dropped once the morphological transition started, approximately between 30 and 40 hours from pattern confluence. This reduction in area and perimeter was a progressive rather than a sudden change and reached its maximum (30%) on average after 65 hours. Conversely, the perimeter and the area of the not dewetted islands increased slightly (around the 10%).

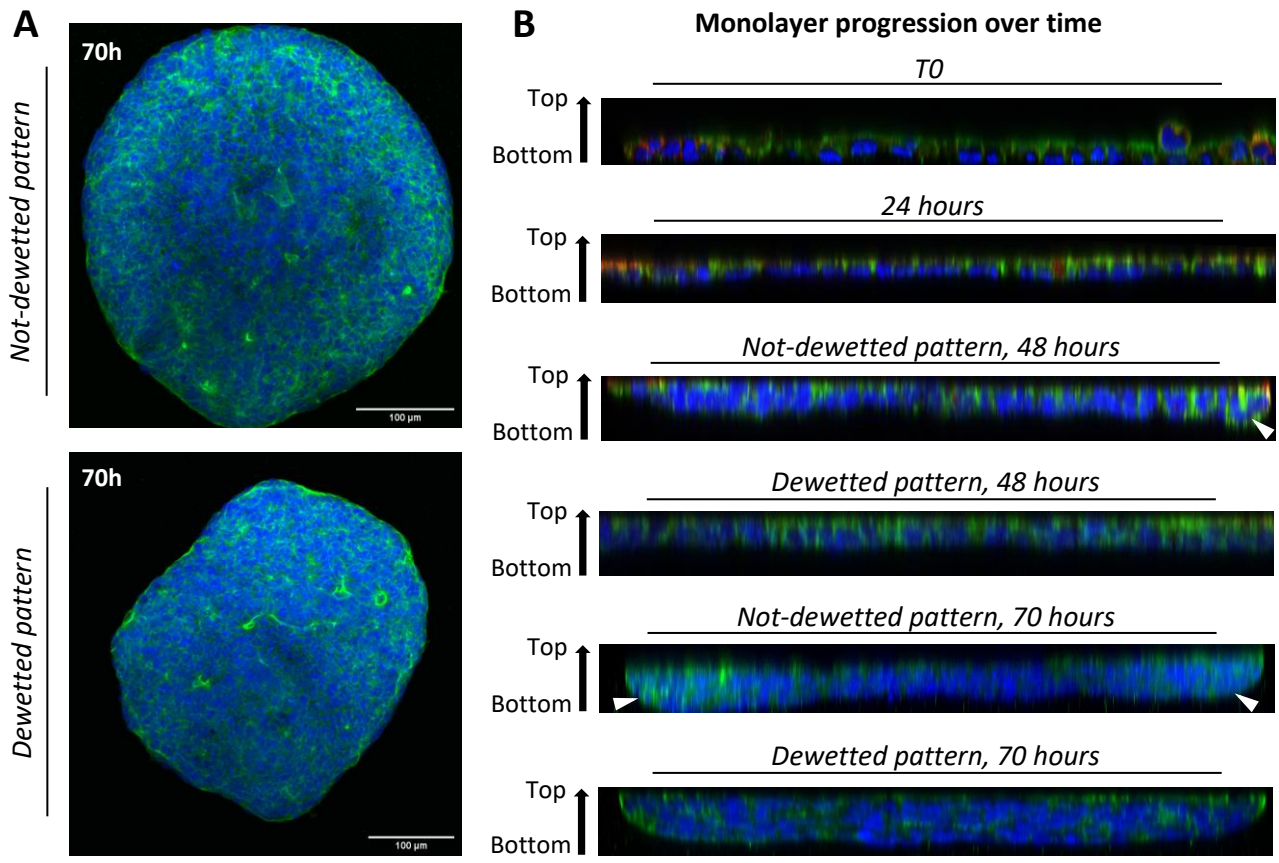


***Figure 4.3.4.*** *(A) Representative MAX- projection of not dewetted and dewetted LS174T pattern, imaged 70 hours after confluence. F-actin= green, DAPI= Blue. (B) Orthogonal views of dewetted or not dewetted LS174T patterns, imaged at different time points. All the patterns were stained for F-actin (green), DAPI (blue); T0 and T24 were also stained for Ezrin (red). White arrowheads point at rim-like structures.*

This change in area and perimeter of dewetted LS174T patterns was not isotropic but asymmetric. This could be assessed from both the axis ratio and the eccentricity, which increased in dewetted patterns. Therefore, islands lose their circularity and assume a shape closer to the one of an ellipse during the dewetting (figure 4.3.5, bottom panels).

On the other hand, the not-dewetted patterns maintain their circular shape throughout the experiment, as displayed also by live imaging and confocal microscopy (figures 4.3.2A and 4.3.4A). Taken together, these results show that that the phenomenon of dewetting in LS174T patterns is a morphological transition that starts after 30-35 hours from confluency and occurs in a progressive and non-symmetric fashion.

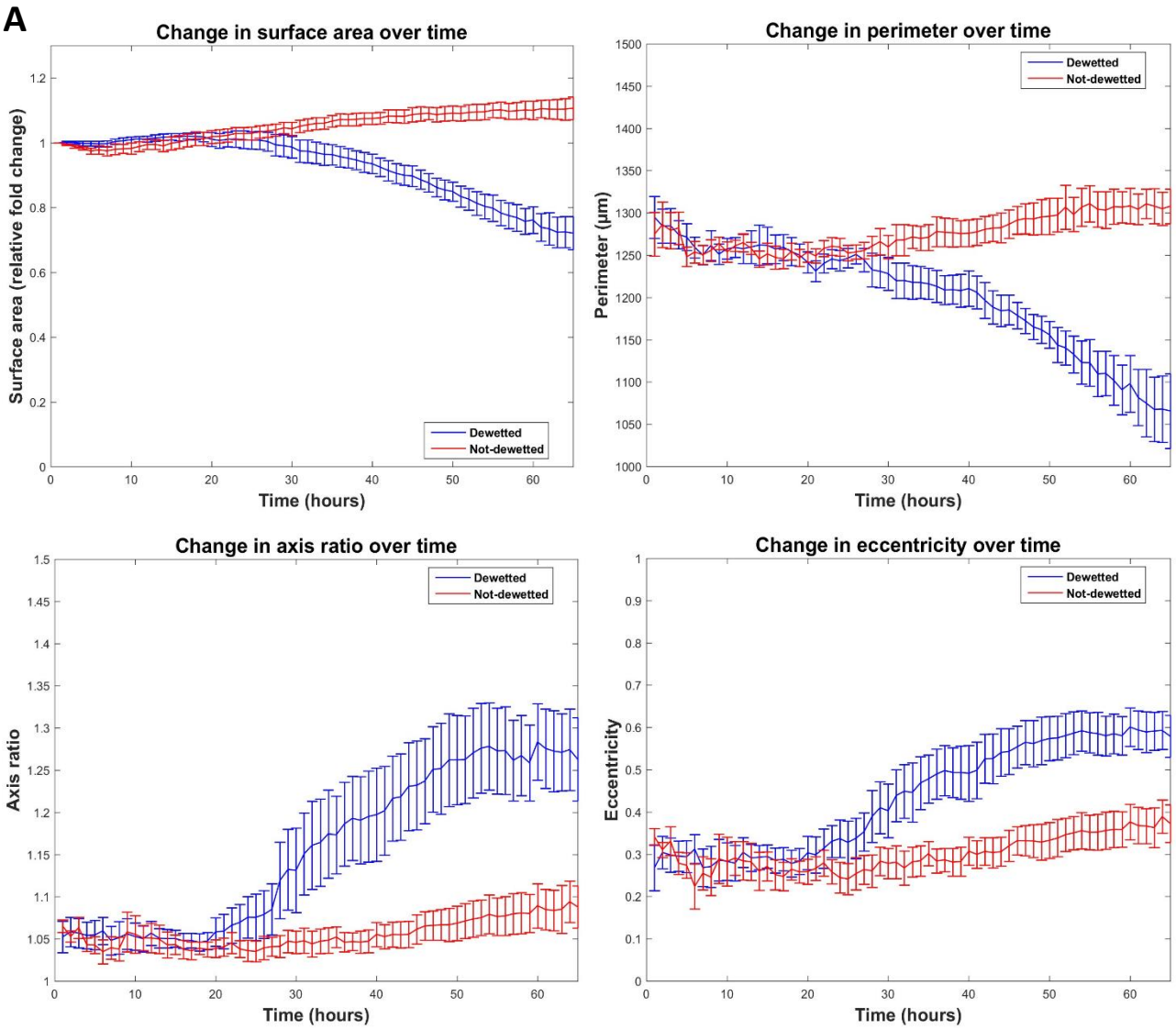


***Figure 4.3.5.*** *(A) Quantification of morphological properties in dewetted (blue) and not dewetted patterns (red): change in surface area over time, change in perimeter over time, change in axis ratio over time and change in eccentricity over time. Eccentricity is defined as the deviation of a curve or orbit from circularity, and it ranges from 0 for a circle to 1 for a parabola. Analysis done on 8 dewetted patterns and on 6 not-dewetted ones, selected among 3 independent experiments.*

*4.3.3 Dewetting in LS174T patterns is characterized by a specific mechanical signature*

To evaluate if these morphological changes happening during dewetting could be associated with different traction profiles, we quantified the total traction forces exerted by the dewetting patterns in comparison to the not dewetted ones (figure 4.3.6).

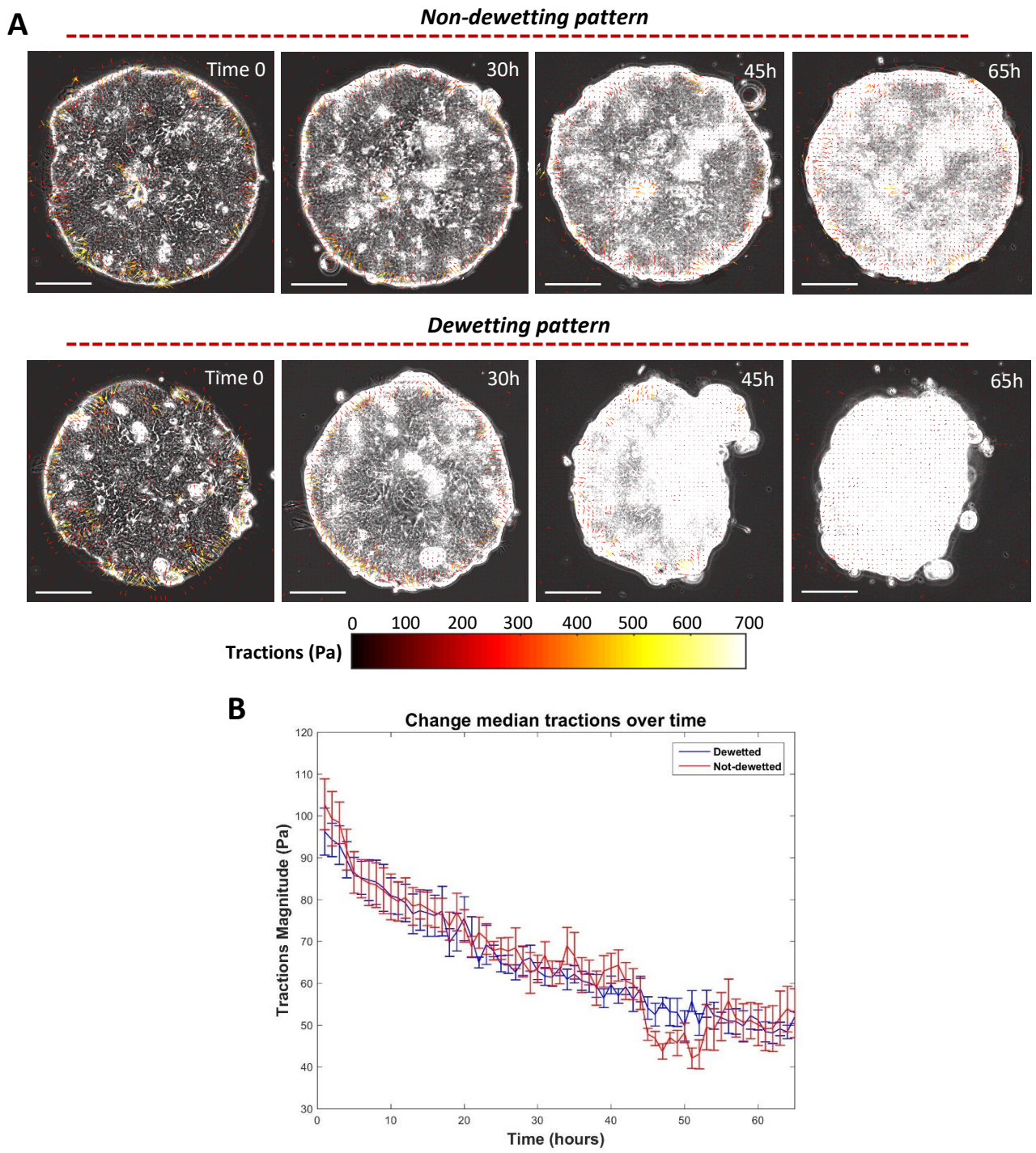

***Figure 4.3.6.*** *(A) Representative phase contrast time-lapses and traction forces of a dewetting patterns vs a non-dewetting one. Scale bars: 50 µm. (B) Quantification of traction forces exerted by dewetted or not-dewetted LS174T patterns on the substrate. The median of traction magnitudes is plotted over time. Analysis done on 8 dewetted patterns and on 6 not dewetted ones, selected among 3 independent experiments.*

Interestingly, we found out that the overall traction profiles were very similar, as traction forces dropped of approximately 50% in both cases, namely from 100 Pa to 50 Pa, on average (figure 4.3.6B). As the quantification of forces in whole epithelia did not reveal any noticeable difference between dewetted and not dewetted samples, we decided to subdivide the islands in 3 sub-domains to evaluate if we could find differential traction profiles in these distinct subregions (figure 4.3.7). The different subdomains, namely internal, external and middle ones, are characterized by the same number of pixels for unbiased statistical analyses over the three regions.

**A**

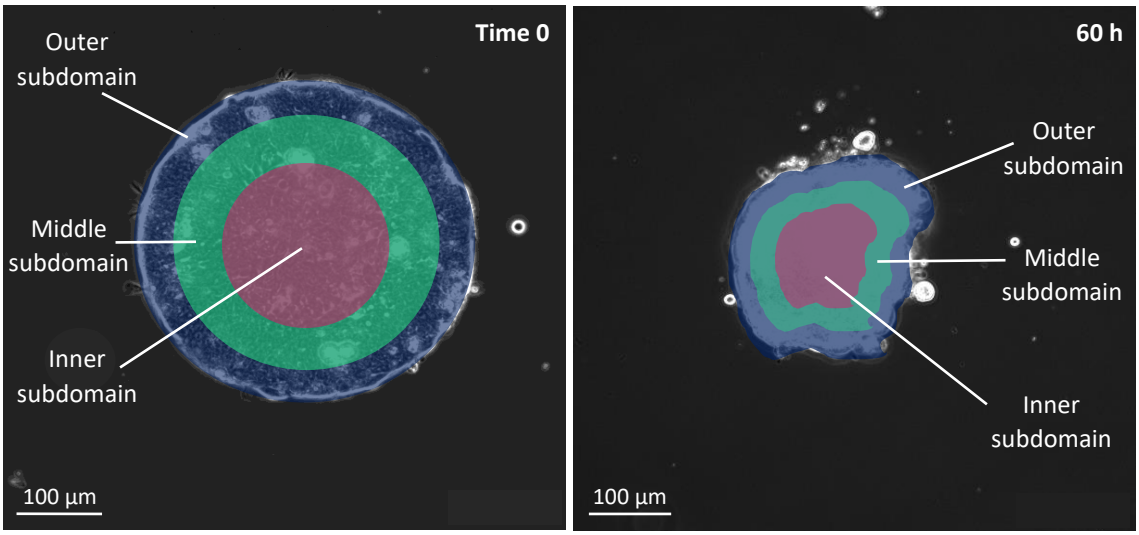


***Figure 4.3.7.*** *(A) Schematics representing a whole LS174T pattern divided in outer, middle and inner subdomains, at the beginning of the experiment (on the left) and after retraction (on the right).*

We quantified the magnitude of tractions (|T|) and decomposed the traction field along the normal and tangential directions with respect to the epithelial domain's edge. We then computed the net normal and net tangential traction force components as a function of time in the different sub-domains.

**A**

*Not-dewetted LS174T pattern*

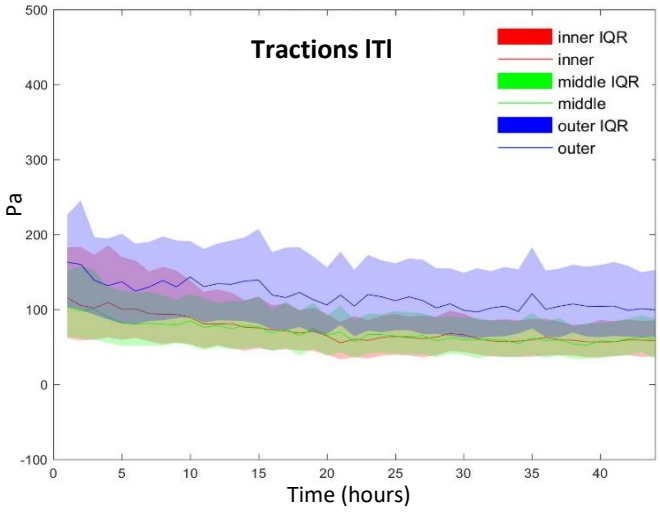


*Dewetted LS174T pattern*

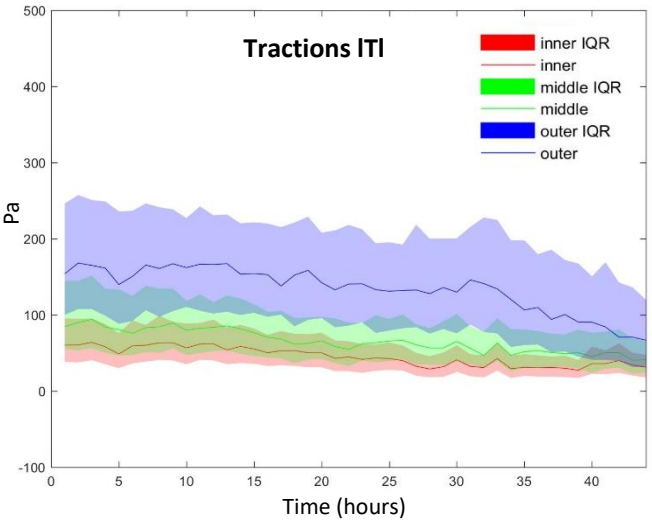


**B**

*Not-dewetted LS174T pattern*

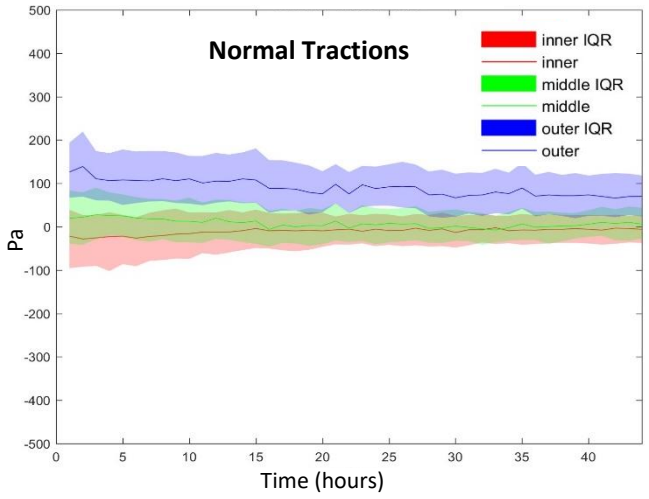


*Dewetted LS174T pattern*

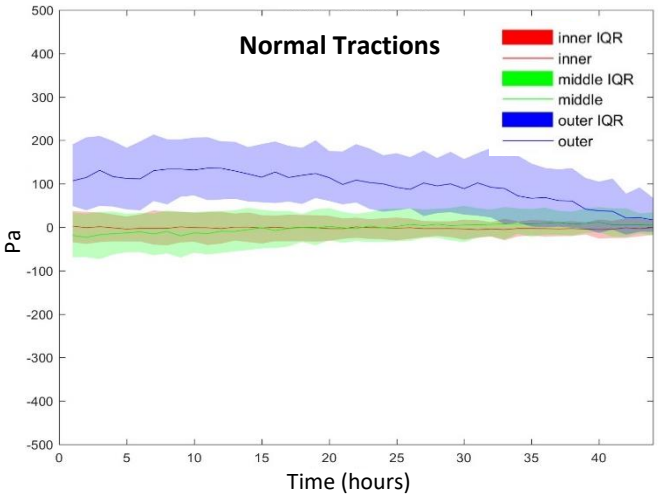


**C**

*Not-dewetted LS174T pattern*

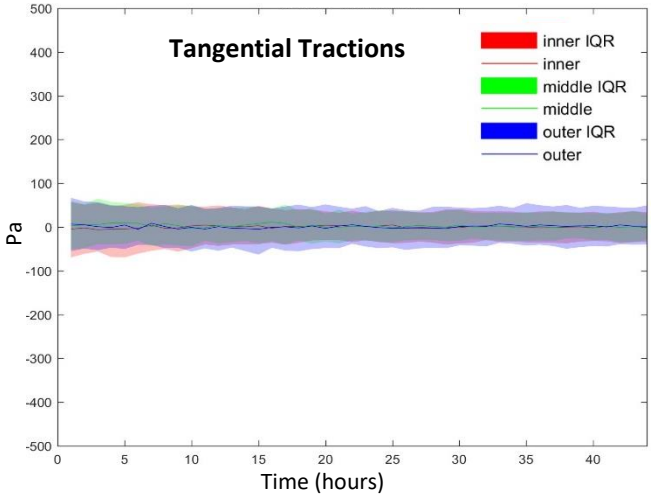


*Dewetted LS174T pattern*

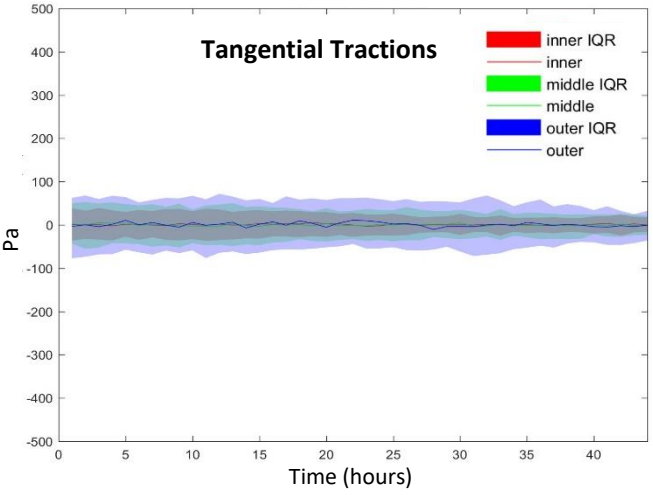

***Figure 4.3.8.*** *(A) Magnitude of tractions (*|T|*) of not-dewetted and dewetted patterns, divided in inner, outer, and middle subregions. (B) Normal tractions of not-dewetted and dewetted patterns, divided in inner, outer, and middle subregions. (C) Tangential tractions of not-dewetted and dewetted patterns, divided in inner, outer, and middle subregions. Results are plotted as mean ± interquartile range (IQR). Analysis done on 8 dewetted patterns and on 6 not dewetted ones, selected among 3 independent experiments.*

As shown by figure 4.3.8A, outer, middle and inner traction magnitudes in not dewetted samples had a very similar profile and were quite stable in time. On the other hand, in dewetted samples the outer region was exerting higher forces at the beginning of the video, forces that were then rapidly dropping when the monolayer started retracting, namely between 30 and 40 hours. In both cases, the external subregion was exerting higher forces in comparison to the other two sub-domains.

However, in not dewetted patterns the magnitude of inner and middle tractions was comparable, while in dewetted patterns the internal part forces were lower than the middle ones. Regarding normal tractions, also in this case the tractions were steadier in the not dewetted samples, while in the dewetted ones the forces exerted in the outer subregion, higher at the beginning, were dropping after approximately 30-40 hours (4.3.8B). The tangential tractions, on contrary, were almost null and approximately the same throughout the experiments, for both dewetted and not dewetted samples (4.3.8C).

This analysis does not reflect the asymmetrical nature of monolayer retraction in LS174T patterns. Therefore, we subdivided the islands in right and left sub-domains to evaluate if, during monolayer retraction, we could find differential traction profiles in the retracting side with respect to the other one (figure 4.3.9A). We measured forces exerted by the cells in the left and in the right sides of the patterns before, during and after monolayer retraction and we compared them to tractions exerted by not dewetting islands at the same time-lapses. To compare different islands at once, dewetted patterns were disposed to have the retracting part always on the right side. As shown by the graph in figure 4.3.9B, during monolayer dewetting, the retracting side exerts less forces with respect to the non-retracting one. On the other hand, before and after monolayer retraction, cells exert similar tractions in the right and in the left subdomains of dewetting patterns.

Throughout the whole experiment, non-dewetting islands exert comparable forces in the right as well as in the left subdomains. Overall, this analysis underlines that, during monolayer dewetting, traction forces are exerted in a non-symmetrical fashion.

Altogether, these results demonstrated that dewetting in confined LS174T epithelia show a specific mechanical signature that reflects its asymmetrical nature.

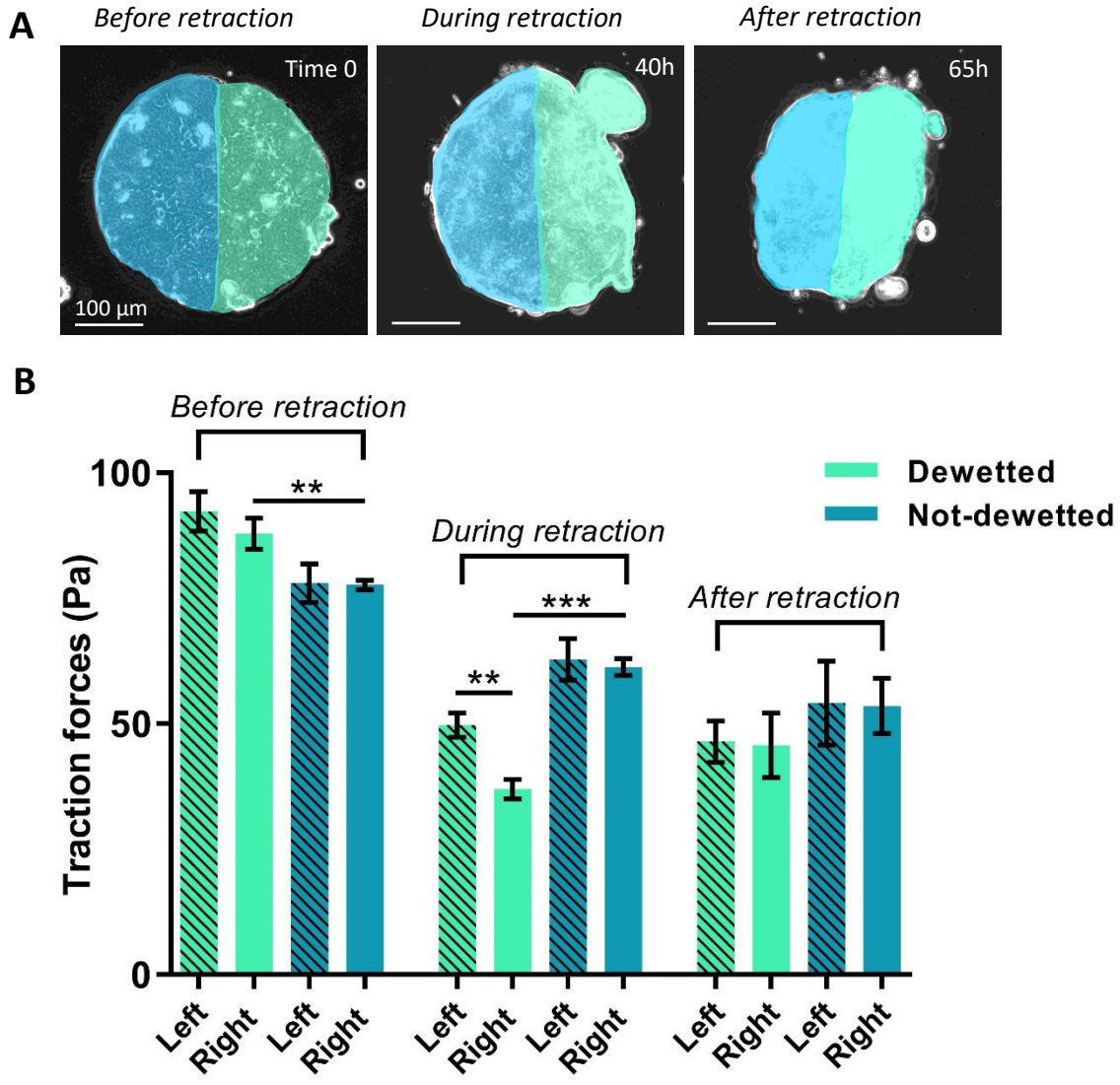


***Figure 4.3.9.*** *(A) Schematics representing a whole LS174T pattern divided in left and right subdomains, before, during and after monolayer retraction. Scale bars: 50 µm. (B) Quantification of traction magnitudes of left and right subdomains, measured before, during and after epithelia retraction. Not-dewetted left vs not-dewetted right subdomains: not significant, in all the time points analysed. Dewetted left vs dewetted right subdomains, analysed before and after monolayer retraction: not significant. Results are presented as mean ± standard error of the mean (SEM). p<0.05 = (*), p<0.01 = (**) and p<0.001 = (***),* t-tests, *N= 2 experiments.*

*4.3.4 Dewetting of LS174 patterns depends on adhesion to the substrate*

As described by Perez and colleagues, substrate adhesion is a key pattern in determining dewetting of confined MDA-MB-231 patterns in which E-cadherin expression has been induced[64]. Therefore, we hypothesised that adhesion to the substrate could play a role in the dewetting of confined LS174T patterns as well.

To assess that, we fabricated polyacrylamide hydrogels having different ECM ligand densities (100, 10 or 1 μg/ml Collagen type I coating). As depicted by figure 4.3.10A, the percentage of dewetting patterns increases dramatically, when the concentration of Collagen I is reduced.

Indeed, 39 ± 5 % of LS174T patterns dewetted in the 100 μg/ml condition, while the dewetting percentage was reaching 82,7 ± 2,4 % and 100% in the 10 μg/ml and in the 1 μg/ml conditions, respectively.

Interestingly, while the patterns grown on hydrogels with higher ECM ligand density dewetted between 30 and 40 hours, the ones with intermediate and low ligand density dewetted between 20 and 25 hours and 10-15 hours, respectively (figure 4.3.10.B). Therefore, also in LS174T confined patterns, substrate adhesion is a key parameter in determining transition from cellular spreading to dewetting. Moreover, as depicted by the bottom time-lapses, LS174T cells grown on hydrogels with 1 μg/ml coating completely detached from the substrate by the end of the experiment. This complete detachment from the underlying gel was displayed by the 67% of the patterns grown with low Collagen density and by the 18 % of the islands plated on intermediate ECM-dense substrates. It should also be noted that cells grown on hydrogels with low ECM ligand density fail to reach complete confluence in the experimental conditions tested.

Taken together, these results demonstrated that dewetting in LS174 confined epithelia depends on adhesion to the substrate.

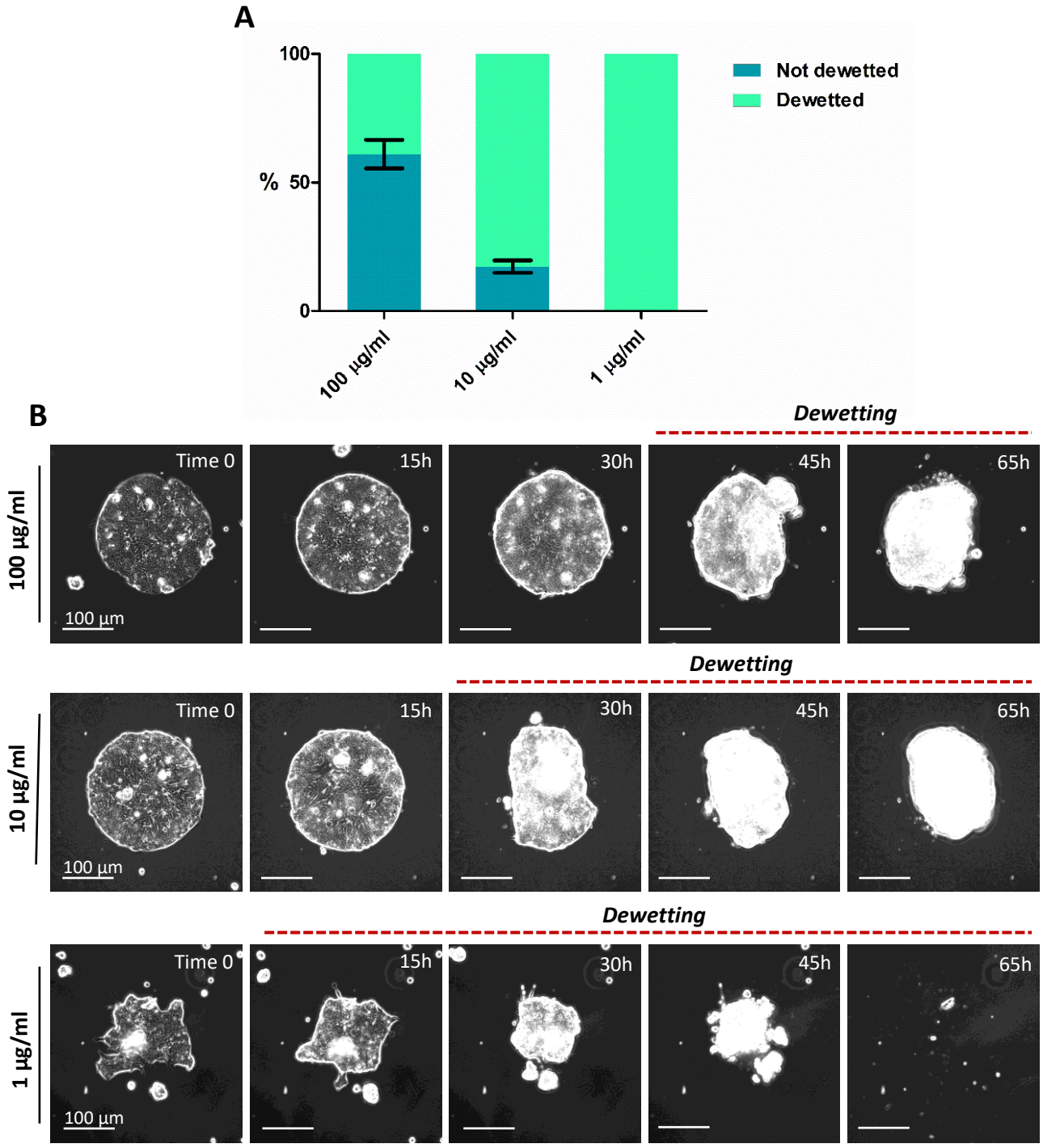


***Figure 4.3.10.*** *(A) Comparison of dewetting percentage in substrate coated with 100, 10 and 1 µg/ml Collagen type I solution. Results are presented as mean ± standard error of the mean (SEM). Two-way ANOVA, p<0.0001 = (*). N= 3 experiments. (B) Representative phase contrast time-lapses of dewetting in PAA hydrogels coated with 100, 10 and 1 µg/ml Collagen type I. N= 3 experiments.*

# 5. Discussion

With the discovery of the interplay between molecular and mechanical mechanisms in cancer[1,4,9], interest in the mechanobiology of tumour progression has significantly raised. Indeed, over the past decade, scientists have highlighted the importance of mechanical cues such as matrix stiffness, substrate topography, mechanical stresses in cells or tissues, and cell deformation in influencing over-proliferation, tumour growth and metastasis[1,2,3]. The clinical relevance of cancer mechanical properties is for example stressed by the fact that the diagnosis of certain solid tumours can involve examination of changes in tissue density and stiffness, evaluated by palpation or imaging techniques such as mammograms. Indeed, various research groups have demonstrated that higher stiffness and more elevated density of the tumour microenvironment drive cancer progression and cause differentiation into more invasive cellular phenotypes[4,5].

The relevance of mechanical cues has also been highlighted by the discovery of novel mechano-based therapies and mechano-medicines targeting increased tissue stiffness and/or associated cellular responses[24,59]. For example, Shen *et al*. demonstrated that targeting tissue stiffness in metastatic colorectal cancers using mechano-drugs Losartan and Captopril[131], could improve the therapeutic outcome of anti-angiogenic treatments[58]. Similarly, Vennin and colleagues, showed that the Rho kinase inhibitor Fasudil increases the efficacy of chemotherapy in pancreatic cancer by reducing stroma stiffening and fibrosis[132]. Altogether, these examples underline how clinically relevant is to further characterize the mechanical alterations arising during cancer progression and metastasis.

In this context, the experiments and results presented in this thesis aim to shed light on the biomechanics of colorectal cancer progression. In particular, in the first part of this PhD, we demonstrated the fundamental role of mechanical cues in determining the budding of colorectal cancer, while in the second part we elucidated the mechanical properties of dewetting colorectal carcinoma epithelia.

To study the phenomenon of budding and to monitor cell mechanics during this process, we built an *in vitro* platform where the polyacrylamide hydrogels mimic the tumour stroma and the LS513 cells model the colorectal lining. We chose this line because LS513 cells show the same genetic profile of most colorectal cancer patients displaying buds and tumour spheres

with inverted polarity (TSIPs) in their explants and effusions. Therefore, we reasoned that they could be employed to decipher *in vitro* the mechanism of budding. Indeed, these cells show a G12D mutation in the KRAS gene, one of the most prevalent and oncogenic KRAS mutant variant[133], that is also present in the 65% of patients with TSIPs (tables 8.1.1 and 8.1.2, Appendix).

Despite the lack of the tumour microenvironment, that could also potentially influence the budding process *in vivo*, our *in vitro* model permits to characterise the biomechanical properties of budding epithelia and to better tune this process, with respect to *in vivo* experiments or *ex vivo* explants. Moreover, this model allows us to study in a systematic way and under very controlled conditions how budding responds to mechanical cues and to decipher the physical mechanisms driving this process.

The workflow we put in place for the simultaneous imaging and quantification of buds' morphology and mechanics, allowed us to image the formation of buds *de novo*. This workflow also allowed us to report evidence of different morphological steps of TSIPs/buds formation in LS513 epithelia grown on 30 kPa polyacrylamide hydrogels (Figures 4.2.1, 4.2.2 and 4.2.3). We chose this stiffness because it mimics the rigidity of the colorectal tumour microenvironment, thus being suitable to reproduce the mechanical stimuli sensed by cancer cells during pathological conditions[57]. Moreover, we noticed that the formation of mature buds is marked by an increase in Actin and Ezrin expression in the apical side. This is in line with what was described by Zajac *et al*., who showed that, *ex vivo*, the tumour spheres with inverted polarity employ acto-myosin contractility to invade extracellular matrices[65].

We then wondered if budding areas and regions surrounding budding spots could show different traction forces profiles with respect to normal flat epithelium. As shown by figure 4.2.5B, during budding, forces exerted where the bulging structure is arising and in the surrounding monolayer are significantly higher, if compared to other regions of the epithelium. Interestingly, monolayer areas that will bud, exert higher tractions even before the onset of budding, probably because under compression. Conversely, once the bud is fully formed, forces rapidly decrease and match the tractions applied on the substrate by normal flat monolayer.

Moreover, traction forces in budding areas peak around 2 hours before than the surrounding monolayer regions. Such shift in traction peaks underlines a delay in contractility between the

regions where a bud would eventually emerge and the surrounding monolayer regions. This means that, during budding, compression is initially higher in the area that would prospectively emerges, while after few hours it becomes higher in the surrounding regions.

Because tractions are exerted through the adhesion between epithelia and the substrate, we hypothesised that this decrease in traction forces could be due to partial bud detachment from the substrate. We confirmed this hypothesis by imaging (figure 8.1.2, Appendix) and focal adhesion quantification of mature buds (figure 4.2.6C). Indeed, we demonstrated a significant reduction of focal adhesion inside the bud, with respect to surrounding flat monolayer. Moreover, we also showed that, in around 50% of cases, a hollow cavity between the substrate and the central part of the mature bud was visible (figure 4.2.6A-B).

Since we demonstrated that budding portions of the monolayer exert higher forces on the substrate with respect to flat non-budding monolayer, we hypothesised that we could tune the budding process by altering substrate properties. We focused on substrate stiffness because several groups recently highlighted that the metastatic potential of cancer cells could be modified by tuning stroma elasticity[4,5,57,134]. Indeed, as budding of colorectal cancer epithelia *in vivo* give rise to epithelial cellular clusters that act as invasive and metastatic tumoral intermediates[93], we reasoned that this process could be tuned by increasing or decreasing substrate stiffness. As displayed by figures 4.2.10 and 4.2.11, we showed that substrate stiffening and softening have an impact on the morphology as well as on the number of buds produced by LS513 epithelia. Indeed, we demonstrated that matrix softening causes a reduction in bud production and a decrease in average bud surface, while substrate stiffening triggers an increment in bud area and an increase in LS513 epithelia budding.

We then wanted to assess if budding was occurring only because of cell mechanics or if any molecular pathways could be implicated as well in the onset of this phenomenon. Considering that most colorectal cancer patients developing budding have a mutation on KRAS gene and that our cell model displays the same mutation (tables 8.1.1 and 8.1.2, Appendix), we wondered if this oncogene or the signalling downstream its activation could be involved in budding. Indeed, while most colorectal carcinomas are characterized by the loss of function of adenomatous polyposis coli (APC) gene[48, 50,55], the majority of patients with TSIPs and buds in their biopsies have a CpG island methylator phenotype (CIMP) subtype, characterized either by KRAS or BRAF mutation[65].

Several studies have reported that KRAS and HRAS overactivation or overexpression result in mechanical alterations that could lead to large-scale deformations of epithelial tissues, including buckling, folding and even budding[18,33,34,39]. Moreover, various groups have recently reported that the cell competition between cells with hyperactivated HRAS or KRAS and the rest of the monolayer could lead to basal or apical extrusion of transformed clusters from the epithelium[35,37]. Although cell extrusion is commonly regarded as a defence mechanism of epithelia, extruded transformed cells can hijack this mechanism to ultimately enable distant organs invasion[15].

Therefore, as budding in LS513 epithelia could be seen as a multicellular apical extrusion from the surrounding monolayer, we hypothesised that KRAS could be over-expressed in bulging structures with respect to non-budding regions. However, the expression of this oncogene was not significantly higher in buds in comparison to flat non-budding regions (figure 4.2.12A-B).

Since KRAS activation results in the induction of the downstream signalling cascade of the mitogen-activated protein kinase/extracellular signal-regulated kinase (MAPK/ERK), we then wondered whether this pathway could be implicated in the budding. Indeed, despite the lack of a significant difference in the expression of KRAS at budding sites, LS513 cells treated with MAPK inhibitors SCH or Trametinib almost completely lost the capability to bud (figure 4.2.13). This indicate that that an overall MAPK activation throughout the epithelium is required for budding in LS513 epithelia.

Since these results attest that KRAS-induced MAPK activation causes budding with no particular spatial localization, we wanted to evaluate if any local phenomena could drive this process. Indeed, we wanted to understand if the presence of buds could be associated with a characteristic 'cell signature' at the level of the monolayer. Therefore, we assessed the role of two local features, namely cellular velocities and cellular orientations, in budding formation.

In particular, we wanted to evaluate if bud formation could be associated with specific cellular movements that could drive the budding process. We reasoned that it would be possible to identify a specific pattern of cell velocities that might anticipate bud arising. Indeed, during bud formation we noticed the presence of a peculiar pattern of cell velocities, creating a sort

of vortex around the area where the bud would form (figure 4.2.14). Moreover, we also revealed that budding areas area characterized by higher vorticity, with respect to non-budding areas (figure 4.2.15).

Having demonstrated that bud formation is associated to the presence of cellular swirls and higher vorticity, we wondered whether also specific cell orientations and topological defects could play a role in this process. Various research groups have highlighted the importance of topological defects in regulating cellular processes such as extrusion, apoptosis and the emergence of complex multicellular architectures[108,112,113,102,129]. For example, Saw and colleagues studied apoptotic cell extrusion in MDCK epithelia and demonstrated that this phenomenon is caused by defects in cell alignments in the form of comet-shaped topological defects (+1/2)[112]. Thus, as budding of LS513 could be seen as a multicellular apical extrusion from the surrounding monolayer, we wondered if topological defects could play a role in this process as well.

As displayed by figures 4.2.16 and 4.2.17 we confirmed that the presence of mature budding structures is associated with abrupt changes in cell orientations and topological defects, both on stiff as well as on soft substrates. We then wanted to assess whether we could identify specific patterns of -1/2 or +1/2 defects before and during the formation of the bud, that could serve as a predictor of the areas in which the bulging structures would arise. We found out that the monolayer sub-regions in which a bud would appear were displaying high topological charge and high density of +1/2 defects, while low charge and fewer defects were found in non-budding areas (figure 4.2.18). These results confirmed that budding formation in LS513 epithelia is correlated with the emergence of +1/2 defects. These findings are in line with previous literature demonstrating that cell extrusion occurs in epithelia regions characterized by comet-shaped topological defects[112].

Since we demonstrated that +1/2 defects are associated with the emergence of bulging structures, we thought that forcing cellular alignment would result in budding impairment by reducing topological defects. To do so, LS513 cells were plated on micro-structured hydrogels with rectangular grooves. As shown in figure 4.2.22, bud formation on grooved gels was significantly impaired with respect to flat gels having the same stiffness.

We hypothesized that this budding impairment on grooved gels could be due to vorticity and topological defects reduction. Indeed, we thought that vorticity and topological charge would

be lower in epithelia grown on grooved gels, which are more constrained, with respect to epithelia plated on flat hydrogels. As shown by figures 4.2.23 and 4.2.25, both vorticity and topological defects of LS513 cells were drastically reduced on micro-structured gels. Therefore, we demonstrated that topographical-induced cellular alignment causes budding impairment in LS513 epithelia via defects and vorticity reduction.

Overall, these results underline the pivotal role played by substrate topology in determining colorectal carcinomas budding. As these findings demonstrate the relationship between cellular alignment and the appearance of malignant 3D structures in colon epithelium, it would be fascinating to identify the molecular mechanisms that could enhance or hinder this alignment, to ultimately reduce the ability of these epithelia to bud.

Having demonstrated that MAPK cascade inhibition causes budding reduction in LS513 cells, we then wanted to assess whether this inhibition could have any effects also topological defects formation. We indeed wanted to evaluate whether the reduction in bud number in LS513 epithelia treated with MAPK inhibitors could also correlate with a decrease of topological defects arising in the monolayer. As depicted by figure 4.2.20, LS513 cells treated with SCH, present less topological charge than untreated cells.

To our knowledge, this is the first study establishing a link between MAPK pathway inhibition and the decrease of topological defects in the LS513 epithelium. We speculate that one of the mechanisms through which MAPK cascade inhibition hinders budding is topological defects reduction. This reduction could be directly caused by MAPK pathway inhibition or by other pathways that have an upstream effect on cellular orientations, vorticity and topological defects.

Therefore, the mechanisms through which MAPK inhibition causes defects and buds reduction are still far to be understood. In this context, it would be particularly relevant to also assess the effect of MAPK over-activation on budding of LS513 epithelia as well as on the emergence of topological defects. On the other hand, it would also be fascinating to evaluate if substrate topology influences MAPK activation; indeed, due to the lower number of buds found on micro-structure gels, we would expect LS513 cells grown on these substrates to show less MAPK activation, with respect to flat gels. However, these are assumptions that need to be confirmed by further investigations.

Besides having mechanically characterised the phenomenon of the cell cluster budding in LS513 monolayers, we also studied the morphological transitions occurring in whole confined LS174T epithelia.

Indeed, since we evaluated that the phenomenon of budding in LS174T cells might occur via retraction of a portion of epithelium (figure 4.1.5B), we wondered if we could also find examples of spontaneous whole monolayer retraction.

Such process, which has been outlined in the context of dewetting, is characterized by the retraction of confined flat circular monolayers leading to the formation of 3D spheroid-like structures. This phenomenon has been previously described by Perez and colleagues in MDA-MB-231[64] and by our laboratory in MCF10A epithelia[39] but, to our knowledge, has never been evaluated using LS174T as model.

First, we assessed the spontaneous retraction of LS174T epithelia and the subsequent formation of compact 3D cell aggregates. Among the LS174T patterns analysed, 40% dewetted forming a spheroid-like structure approximately 35 hours after having reached confluence, while 60% did not dewet throughout the experiment (figure 4.3.3).

To characterize the changes occurring at the level of the monolayer during dewetting of LS174T patterns, we compared the morphological properties of dewetted patterns to the ones of not dewetted patterns.

We discovered that the area and the perimeter of the dewetted patterns dropped once the morphological transition started, while the axis ratio and the eccentricity increased (figure 4.3.5). This means that, during dewetting, patterns lose their circularity and symmetry and assume a shape closer to the one of an ellipse.

These results let us conclude that dewetting in LS174T epithelia happens in a non-symmetric fashion; indeed, if the monolayer retraction occurred in a symmetric way, circularity would be preserved during monolayer retraction. This striking symmetry breaking is in contrast with the known isotropic dewetting of passive fluids[94,135,136]. This suggests that, in our system, epithelia retraction could be due to morphological instability of active origin.

We therefore speculated that this asymmetrical retraction could derive from mechanical instability, specifically from differences in contractility. Indeed, we found out that, in dewetting patterns, the retracting edge exerts less forces on the substrate, if compared to the non-retracting side of the island (figure 4.3.9B). On the other hand, the symmetry of non-

dewetting patters is reflected by the traction profiles of its two sides, that are always comparable throughout the experiment (figure 4.3.9B).

To further characterize the changes occurring at the monolayer level during dewetting, we imaged the patterns at different time-points via Confocal microscopy and we analysed the cellular organization in the z plane orthogonal to the underlying elastic substrate. This analysis revealed that both dewetted and non-dewetted patterns showed juxtaposition of several sheets of cells (figure 4.3.4.B). However, non-dewetted patterns presented a peripheral thicker border of cells which was not found in dewetted ones.
The emergence of an analogous external rim was also showed by Deforet *et al*. in confined patterns of MDCK cells. They demonstrated that the formation of such 3D structure could be the result of proliferation as well as of the additional degrees of freedom of border cells[137]. In our case, the biological and biophysical meaning of this border of LS174T cells is still far to be understood.
Since we did not report the presence of a similar structure in dewetted patterns, we speculated that the emergence of this rim could prevent the retraction of confined patterns.

To study the mechanical contribution of this external border to the process, we divided the patterns in 3 concentric zones in which the most external one roughly corresponded to the rim region (figure 4.3.7), and we evaluated the forces exerted in the three subregions. Since the superposition of force vectors on phase contrast images showed that most of the tractions were located in the external regions of the patterns (figure 4.3.6A), we hypothesised that we could find differential traction profiles among the distinct zones of the islands.

As shown in figure 4.3.8, in non-dewetted samples, the magnitudes and the normal tractions applied on the substrate by the outer, the middle and the inner sub-regions were quite stable in time. Conversely, in dewetted samples the outer domain was exerting higher forces before the onset of monolayer retraction, forces that were then dropping as soon as the dewetting started. Therefore, these differential forces exerted by distinct parts of the island could be an indicator of differential contractility within the monolayer and could play as the main actors of dewetting in confined LS174T epithelia.

As substrate properties were reported to be a key factor in tuning several morphological and malignant events[1,2,3,64], we wondered if changes in ECM density could have any effects on the

dewetting of confined LS174T islands. Indeed, as described by Perez and colleagues, substrate adhesion is a key pattern in determining dewetting of confined MDA-MB-231 patterns in which E-cadherin expression has been induced[64]. Therefore, we hypothesised that, also in our system, this cue could play a fundamental role in determining the switch from cellular spreading to cellular retraction.

As reported in image 4.3.10A, the percentage of dewetting in LS174T islands grown on hydrogels with lower ECM ligand density is higher in comparison to gels with higher Collagen type I coating. Moreover, monolayer retraction starts much earlier in islands with lower ECM ligand density, with respect to patterns with higher-density Collagen coating (4.3.10B). Therefore, we managed to demonstrate that also in LS174T confined patterns, substrate adhesion is a key parameter in determining transition from cellular spreading to dewetting.

Apart from adhesion, Perez and colleagues described substrate stiffness and pattern size as other key players in governing the dewetting transition in MDA-MB-231 confined epithelia[64]. Therefore, in the future we will assess the role played by substrate elasticity and pattern size in determining the dewetting of LS174T patterns. It would be especially interesting to evaluate if LS174T patterns with a diameter closer to the one of LS513 buds (50-100 µm) could retract faster, in comparison to bigger islands. Indeed, we speculate that a smaller pattern diameter would result in a faster transition from spreading to dewetting of LS174T epithelia. On the other hand, we also suppose that this process could be tuned by substrate softening or stiffening, as we showed for budding (figures 4.2.10 and 4.2.11) and as was previously demonstrated for other examples of morphological transitions[64] or malignant transformations[4, 5, 134].

In addition to stiffness and pattern size, it would be also relevant to assess the role of topological defects in the dewetting of confined monolayer. Indeed, it would be intriguing to correlate the emergence of topological defects to this multicellular 2D/3D transition as well. Moreover, identifying specific patterns of comet-like or trefoil-like defects appearing before monolayer retraction could serve as a predictor of the islands that would dewet.

Therefore, additional investigations are needed to further characterise the mechanical cues that could play a role in the phenomenon of LS174T patterns dewetting. A deeper knowledge of this malignant 2D/3D retraction could help us shedding light on the behaviour of certain

solid tumours that can alter their wetting states and/or invasiveness in response to changes in cell contractility, cell adhesion and ECM composition[138,139,140,141].

# 6. Conclusions

The general goal of this thesis was to investigate how supracellular cell and tissue mechanics contribute to colorectal cancer epithelia budding and dewetting. In the first part of the study, we studied the role played by mechanical and topological cues in the formation of budding structures in LS513 monolayers, while in the second part we focused on the mechanical characterization of 2D/3D malignant retraction (dewetting) of confined LS174 epithelia.

The conclusions of the first part of the thesis are the following:

- Our model, LS513 cells, emulates *in vitro* the budding process occurring *ex vivo* in patients' explants with CpG island methylator phenotype (CIMP) colorectal cancer. This *in vitro* platform allowed us to report evidence of different morphological steps of TSIPs/buds formation: the sprouting, the bulging, and the scission.

- We underlined the role of stroma stiffening in colorectal cancer progression; in particular, we highlighted that budding of LS513 epithelia is fostered on stiffer substrates, while it is hindered on soft hydrogels.

- We demonstrated that, in LS513 epithelia, budding occurs in monolayer regions displaying higher traction forces and higher vorticity.

- Bud formation is characterised by the emergence of a cloud-like pattern of +1/2 topological defects at the level of the monolayer. This pattern of comet-like defects, present both on stiff and soft substrates, is visible in the epithelium from the early stages of the process, until the formation of a mature bulging structure.

- Forced cellular alignment, obtained by plating LS513 cells on micro-structured hydrogels with squared ridges, causes budding impairment via vorticity and topological defects reduction.

- KRAS oncogene-mediated MAPK activation is a necessary condition for budding in LS513 epithelia; indeed, the use of MAPK pathway inhibitors dramatically hinders the formation of buds. Interestingly, we also discovered that MAPK inhibition causes dramatic topological defects reduction.

The conclusions of the second part of the thesis are the following:

- If confined via micro-patterning, LS174T cells are able to dewet spontaneously from the underlining soft substrate, forming a 3D spheroid-like structure. This occurs in a non-symmetric fashion and is accompanied by various morphological changes at the level of the monolayer. The asymmetry of this process is reflected by the differential traction profiles exerted during dewetting by the retracting edge, if compared to the other side of the pattern.

- Dewetted LS174T patterns present different normal and magnitude traction profiles, if compared to non-dewetted islands. These differences emerge when patterns are divided in subdomains: outer, middle and internal subregions. Indeed, in dewetted samples the outer region exerts higher forces magnitudes and higher normal tractions before the monolayer retraction, forces that rapidly drop once the dewetting phenomenon starts. On the other hand, normal tractions as well as forces magnitudes are steadier in the outer subdomain of non-dewetted patterns.

- In LS174T confined patterns, substrate adhesion is a key parameter in determining transition from cellular spreading to dewetting. Indeed, the percentage of dewetting in islands grown on hydrogels with lower ECM ligand density is higher in comparison to gels with higher Collagen type I coating. Moreover, monolayer retraction starts much earlier in islands with lower ECM ligand density, with respect to patterns with higher-density Collagen coating.

## 7. References


1. Carey, S. P., D'Alfonso, T. M., Shin, S. J. & Reinhart-King, C. A. Mechanobiology of tumor invasion: Engineering meets oncology. *Crit. Rev. Oncol. Hematol.* **83**, 170–183 (2012).

2. Chaudhuri, P. K., Low, B. C. & Lim, C. T. Mechanobiology of Tumor Growth. *Chem. Rev.* **118**, 6499–6515 (2018).

3. Ladoux, B. & Mège, R.-M. Mechanobiology of collective cell behaviours. *Nat. Rev. Mol. Cell Biol.* **18**, 743–757 (2017).

4. Baker, E. L., Lu, J., Yu, D., Bonnecaze, R. T. & Zaman, M. H. Cancer Cell Stiffness: Integrated Roles of Three-Dimensional Matrix Stiffness and Transforming Potential. *Biophys. J.* **99**, 2048–2057 (2010).

5. Baker, A.-M., Bird, D., Lang, G., Cox, T. R. & Erler, J. T. Lysyl oxidase enzymatic function increases stiffness to drive colorectal cancer progression through FAK. *Oncogene* **32**, 1863–1868 (2013).

6. Levental, K. R. *et al.* Matrix crosslinking forces tumor progression by enhancing integrin signaling. *Cell* **139**, 891–906 (2009).

7. Paszek, M. J. *et al.* Tensional homeostasis and the malignant phenotype. *Cancer Cell* **8**, 241–254 (2005).

8. Kostic, A., Lynch, C. D. & Sheetz, M. P. Differential matrix rigidity response in breast cancer cell lines correlates with the tissue tropism. *PloS One* **4**, e6361 (2009).

9. McGrail, D. J., Kieu, Q. M. N. & Dawson, M. R. The malignancy of metastatic ovarian cancer cells is increased on soft matrices through a mechanosensitive Rho-ROCK pathway. *J. Cell Sci.* **127**, 2621–2626 (2014).

10. Provenzano, P. P. *et al.* Collagen reorganization at the tumor-stromal interface facilitates local invasion. *BMC Med.* **4**, 38 (2006).

11. Kant Chaudhuri, P. Role of Topographic Cues on Cancer Cell Proliferation. *Biophys. J.* **110**, 621a (2016).

12. Chaudhuri, P. K., Pan, C. Q., Low, B. C. & Lim, C. T. Topography induces differential sensitivity on cancer cell proliferation via Rho-ROCK-Myosin contractility. *Sci. Rep.* **6**, 19672 (2016).

13. Drifka, C. R. *et al.* Highly aligned stromal collagen is a negative prognostic factor following pancreatic ductal adenocarcinoma resection. *Oncotarget* **7**, 76197–76213 (2016).

14. Kim, D.-H. *et al.* Biomechanical interplay between anisotropic re-organization of cells and the surrounding matrix underlies transition to invasive cancer spread. *Sci. Rep.* **8**, 14210 (2018).

15. Almagro, J., Messal, H. A., Elosegui-Artola, A., van Rheenen, J. & Behrens, A. Tissue architecture in tumor initiation and progression. *Trends Cancer* **8**, 494–505 (2022).

16. Mohammadi, H. & Sahai, E. Mechanisms and impact of altered tumour mechanics. *Nat. Cell Biol.* **20**, 766–774 (2018).

17. Fu, X. *et al.* Spatial patterns of tumour growth impact clonal diversification in a computational model and the TRACERx Renal study. *Nat. Ecol. Evol.* **6**, 88–102 (2022).

18. Messal, H. A. *et al.* Tissue curvature and apicobasal mechanical tension imbalance instruct cancer morphogenesis. *Nature* **566**, 126–130 (2019).

19. Leu, A. J., Berk, D. A., Lymboussaki, A., Alitalo, K. & Jain, R. K. Absence of functional lymphatics within a murine sarcoma: a molecular and functional evaluation. *Cancer Res.* **60**, 4324–4327 (2000).

20. Hofmann, M. *et al.* Lowering of tumor interstitial fluid pressure reduces tumor cell proliferation in a xenograft tumor model. *Neoplasia N. Y. N* **8**, 89–95 (2006).

21. Chang, S.-F. *et al.* Tumor cell cycle arrest induced by shear stress: Roles of integrins and Smad. *Proc. Natl. Acad. Sci. U. S. A.* **105**, 3927–3932 (2008).

22. Avvisato, C. L. *et al.* Mechanical force modulates global gene expression and beta-catenin signaling in colon cancer cells. *J. Cell Sci.* **120**, 2672–2682 (2007).

23. Barbazan, J. *et al. Cancer-associated fibroblasts actively compress cancer cells and modulate mechanotransduction*. http://biorxiv.org/lookup/doi/10.1101/2021.04.05.438443 (2021) doi:10.1101/2021.04.05.438443.

24. Zhang, J. & Reinhart-King, C. A. Targeting Tissue Stiffness in Metastasis: Mechanomedicine Improves Cancer Therapy. *Cancer Cell* **37**, 754–755 (2020).

25. Sanchez-Vega, F. *et al.* Oncogenic Signaling Pathways in The Cancer Genome Atlas. *Cell* **173**, 321-337.e10 (2018).

26. Zhang, B. *et al.* Focal Adhesion Kinase (FAK) Inhibition Synergizes with KRAS G12C Inhibitors in Treating Cancer through the Regulation of the FAK–YAP Signaling. *Adv. Sci.* **8**, 2100250 (2021).

27. Dawson, J. C., Serrels, A., Stupack, D. G., Schlaepfer, D. D. & Frame, M. C. Targeting FAK in anticancer combination therapies. *Nat. Rev. Cancer* **21**, 313–324 (2021).

28. Gimple, R. C. & Wang, X. RAS: Striking at the Core of the Oncogenic Circuitry. *Front. Oncol.* **9**, 965 (2019).

29. Lavoie, H., Gagnon, J. & Therrien, M. ERK signalling: a master regulator of cell behaviour, life and fate. *Nat. Rev. Mol. Cell Biol.* **21**, 607–632 (2020).

30. Krygowska, A. A. & Castellano, E. PI3K: A Crucial Piece in the RAS Signaling Puzzle. *Cold Spring Harb. Perspect. Med.* **8**, a031450 (2018).

31. Kinbara, K., Goldfinger, L. E., Hansen, M., Chou, F.-L. & Ginsberg, M. H. Ras GTPases: integrins' friends or foes? *Nat. Rev. Mol. Cell Biol.* **4**, 767–777 (2003).

32. Soriano, O., Alcón-Pérez, M., Vicente-Manzanares, M. & Castellano, E. The Crossroads between RAS and RHO Signaling Pathways in Cellular Transformation, Motility and Contraction. *Genes* **12**, 819 (2021).

33. Nyga, A., Ganguli, S., Matthews, H. K. & Baum, B. The role of RAS oncogenes in controlling epithelial mechanics. *Trends Cell Biol.* S0962892422002124 (2022) doi:10.1016/j.tcb.2022.09.002.

34. Fiore, V. F. *et al.* Mechanics of a multilayer epithelium instruct tumour architecture and function. *Nature* **585**, 433–439 (2020).

35. Baker, N. E. Emerging mechanisms of cell competition. *Nat. Rev. Genet.* **21**, 683–697 (2020).

36. Wagstaff, L. *et al.* Mechanical cell competition kills cells via induction of lethal p53 levels. *Nat. Commun.* **7**, 11373 (2016).

37. Tanimura, N. & Fujita, Y. Epithelial defense against cancer (EDAC). *Semin. Cancer Biol.* **63**, 44–48 (2020).

38. Li, R. *et al.* A body map of somatic mutagenesis in morphologically normal human tissues. *Nature* **597**, 398–403 (2021).

39. Nyga et al. Oncogenic RAS instructs morphological transformation of human epithelia via differential tissue mechanics. *Sci. Adv.* 15 (2021).

40. Möller, Y. *et al.* Oncogenic Ras triggers hyperproliferation and impairs polarized colonic morphogenesis by autocrine ErbB3 signaling. *Oncotarget* **7**, 53526–53539 (2016).

41. Moruzzi, M. *et al.* Generation of anisotropic strain dysregulates wild-type cell division at the interface between host and oncogenic tissue. *Curr. Biol.* **31**, 3409-3418.e6 (2021).

42. Guo, Y. *et al.* ERK/MAPK signalling pathway and tumorigenesis (Review). *Exp. Ther. Med.* (2020) doi:10.3892/etm.2020.8454.

43. Pino, M. S. & Chung, D. C. The chromosomal instability pathway in colon cancer. *Gastroenterology* **138**, 2059–2072 (2010).

44. Vogelstein, B. *et al.* Genetic alterations during colorectal-tumor development. *N. Engl. J. Med.* **319**, 525–532 (1988).

45. Guinney, J. *et al.* The consensus molecular subtypes of colorectal cancer. *Nat. Med.* **21**, 1350–1356 (2015).

46. Marisa, L. *et al.* Gene expression classification of colon cancer into molecular subtypes: characterization, validation, and prognostic value. *PLoS Med.* **10**, e1001453 (2013).

47. Juo, Y. Y. *et al.* Prognostic value of CpG island methylator phenotype among colorectal cancer patients: a systematic review and meta-analysis. *Ann. Oncol. Off. J. Eur. Soc. Med. Oncol.* **25**, 2314–2327 (2014).

48. Weisenberger, D. J. *et al.* CpG island methylator phenotype underlies sporadic microsatellite instability and is tightly associated with BRAF mutation in colorectal cancer. *Nat. Genet.* **38**, 787–793 (2006).

49. Ward, R. L. *et al.* Adverse prognostic effect of methylation in colorectal cancer is reversed by microsatellite instability. *J. Clin. Oncol. Off. J. Am. Soc. Clin. Oncol.* **21**, 3729–3736 (2003).

50. Bettington, M. *et al.* The serrated pathway to colorectal carcinoma: current concepts and challenges. *Histopathology* **62**, 367–386 (2013).

51. O'Brien, M. J., Zhao, Q. & Yang, S. Colorectal serrated pathway cancers and precursors. *Histopathology* **66**, 49–65 (2015).

52. van Gestel, Y. R. B. M. *et al.* Patterns of metachronous metastases after curative treatment of colorectal cancer. *Cancer Epidemiol.* **38**, 448–454 (2014).

53. Segelman, J. *et al.* Incidence, prevalence and risk factors for peritoneal carcinomatosis from colorectal cancer. *Br. J. Surg.* **99**, 699–705 (2012).

54. Sugarbaker, P. H. Peritoneal carcinomatosis: natural history and rational therapeutic interventions using intraperitoneal chemotherapy. *Cancer Treat. Res.* **81**, 149–168 (1996).

55. Brody, H. Colorectal cancer. *Nature* **521**, S1–S1 (2015).

56. Ciasca, G., Papi, M., Minelli, E., Palmieri, V. & Spirito, M. D. Changes in cellular mechanical properties during onset or progression of colorectal cancer. **22**, 13.

57. Tang, X. *et al.* A mechanically-induced colon cancer cell population shows increased metastatic potential. *Mol. Cancer* **13**, 131 (2014).

58. Shen, Y. *et al.* Reduction of Liver Metastasis Stiffness Improves Response to Bevacizumab in Metastatic Colorectal Cancer. *Cancer Cell* **37**, 800-817.e7 (2020).

59. Lampi, M. C. & Reinhart-King, C. A. Targeting extracellular matrix stiffness to attenuate disease: From molecular mechanisms to clinical trials. *Sci. Transl. Med.* **10**, eaao0475 (2018).

60. Gonzalez-Rodriguez, D., Guevorkian, K., Douezan, S. & Brochard-Wyart, F. Soft Matter Models of Developing Tissues and Tumors. *Science* **338**, 910–917 (2012).

61. Jülicher, F. & Eaton, S. Emergence of tissue shape changes from collective cell behaviours. *Semin. Cell Dev. Biol.* **67**, 103–112 (2017).

62. Good, M. & Trepat, X. Cell parts to complex processes, from the bottom up. *Nature* **563**, 188–189 (2018).

63. Friedl, P. & Gilmour, D. Collective cell migration in morphogenesis, regeneration and cancer. *Nat. Rev. Mol. Cell Biol.* **10**, 445–457 (2009).

64. Pérez-González, C. *et al.* Active wetting of epithelial tissues. *Nat. Phys.* **15**, 79–88 (2019).

65. Zajac, O. *et al.* Tumour spheres with inverted polarity drive the formation of peritoneal metastases in patients with hypermethylated colorectal carcinomas. *Nat. Cell Biol.* **20**, 296–306 (2018).

66. Lubarsky, B. & Krasnow, M. A. Tube morphogenesis: making and shaping biological tubes. *Cell* **112**, 19–28 (2003).

67. Metzger, R. J. & Krasnow, M. A. Genetic control of branching morphogenesis. *Science* **284**, 1635–1639 (1999).

68. Hogan, B. L. M. & Kolodziej, P. A. Organogenesis: molecular mechanisms of tubulogenesis. *Nat. Rev. Genet.* **3**, 513–523 (2002).

69. Chung, S. & Andrew, D. J. The formation of epithelial tubes. *J. Cell Sci.* **121**, 3501–3504 (2008).

70. Nelson, C. M. On Buckling Morphogenesis. *J. Biomech. Eng.* **138**, 021005 (2016).

71. Goodwin, K. *et al.* Smooth muscle differentiation shapes domain branches during mouse lung development. *Dev. Camb. Engl.* **146**, dev181172 (2019).

72. Kim, H. Y. *et al.* Localized Smooth Muscle Differentiation Is Essential for Epithelial Bifurcation during Branching Morphogenesis of the Mammalian Lung. *Dev. Cell* **34**, 719–726 (2015).

73. Young, R. E. *et al.* Smooth Muscle Differentiation Is Essential for Airway Size, Tracheal Cartilage Segmentation, but Dispensable for Epithelial Branching. *Dev. Cell* **53**, 73-85.e5 (2020).

74. Wang, S., Matsumoto, K., Lish, S. R., Cartagena-Rivera, A. X. & Yamada, K. M. Budding epithelial morphogenesis driven by cell-matrix versus cell-cell adhesion. *Cell* **184**, 3702-3716.e30 (2021).

75. Lugli, A. *et al.* Recommendations for reporting tumor budding in colorectal cancer based on the International Tumor Budding Consensus Conference (ITBCC) 2016. *Mod. Pathol. Off. J. U. S. Can. Acad. Pathol. Inc* **30**, 1299–1311 (2017).

76. Berg, K. B. & Schaeffer, D. F. Tumor budding as a standardized parameter in gastrointestinal carcinomas: more than just the colon. *Mod. Pathol. Off. J. U. S. Can. Acad. Pathol. Inc* **31**, 862–872 (2018).

77. De Smedt, L. *et al.* Expression profiling of budding cells in colorectal cancer reveals an EMT-like phenotype and molecular subtype switching. *Br. J. Cancer* **116**, 58–65 (2017).

78. Almangush, A., Karhunen, M., Hautaniemi, S., Salo, T. & Leivo, I. Prognostic value of tumour budding in oesophageal cancer: a meta-analysis. *Histopathology* **68**, 173–182 (2016).

79. Guo, Y.-X., Zhang, Z.-Z., Zhao, G. & Zhao, E.-H. Prognostic and pathological impact of tumor budding in gastric cancer: A systematic review and meta-analysis. *World J. Gastrointest. Oncol.* **11**, 898–908 (2019).

80. Karamitopoulou, E. *et al.* Tumour budding in pancreatic cancer revisited: validation of the ITBCC scoring system. *Histopathology* **73**, 137–146 (2018).

81. Kadota, K. *et al.* Tumor Budding Correlates With the Protumor Immune Microenvironment and Is an Independent Prognostic Factor for Recurrence of Stage I Lung Adenocarcinoma. *Chest* **148**, 711–721 (2015).

82. Neppl, C., Zlobec, I., Schmid, R. A. & Berezowska, S. Validation of the International Tumor Budding Consensus Conference (ITBCC) 2016 recommendation in squamous cell carcinoma of the lung-a single-center analysis of 354 cases. *Mod. Pathol. Off. J. U. S. Can. Acad. Pathol. Inc* **33**, 802–811 (2020).

83. Jesinghaus, M. *et al.* Introducing a novel highly prognostic grading scheme based on tumour budding and cell nest size for squamous cell carcinoma of the uterine cervix. *J. Pathol. Clin. Res.* **4**, 93–102 (2018).

84. Pease, J. C., Brewer, M. & Tirnauer, J. S. Spontaneous spheroid budding from monolayers: a potential contribution to ovarian cancer dissemination. *Biol. Open* **1**, 622–628 (2012).

85. Voutsadakis, I. A. Prognostic role of tumor budding in breast cancer. *World J. Exp. Med.* **8**, 12–17 (2018).

86. Li, X., Wei, B., Sonmez, C., Li, Z. & Peng, L. High tumor budding count is associated with adverse clinicopathologic features and poor prognosis in breast carcinoma. *Hum. Pathol.* **66**, 222–229 (2017).

87. Zlobec, I., Berger, M. D. & Lugli, A. Tumour budding and its clinical implications in gastrointestinal cancers. *Br. J. Cancer* **123**, 700–708 (2020).

88. Talmadge, J. E. & Fidler, I. J. AACR centennial series: the biology of cancer metastasis: historical perspective. *Cancer Res.* **70**, 5649–5669 (2010).

89. Zeidman, I. & Buss, J. M. Transpulmonary passage of tumor cell emboli. *Cancer Res.* **12**, 731–733 (1952).

90. Liotta, L. A., Saidel, M. G. & Kleinerman, J. The significance of hematogenous tumor cell clumps in the metastatic process. *Cancer Res.* **36**, 889–894 (1976).

91. Cheung, K. J. & Ewald, A. J. A collective route to metastasis: Seeding by tumor cell clusters. *Science* **352**, 167–169 (2016).

92. Rogers, A. C. *et al.* Systematic review and meta-analysis of the impact of tumour budding in colorectal cancer. *Br. J. Cancer* **115**, 831–840 (2016).

93. Ewald, A. J. Metastasis inside-out: dissemination of cancer cell clusters with inverted polarity. *EMBO J.* **37**, (2018).

94. Edwards, A. M. J., Ledesma-Aguilar, R., Newton, M. I., Brown, C. V. & McHale, G. Not spreading in reverse: The dewetting of a liquid film into a single drop. *Sci. Adv.* **2**, e1600183 (2016).

95. Glazier, J. A., Gross, S. P. & Stavans, J. Dynamics of two-dimensional soap froths. *Phys. Rev. A* **36**, 306–312 (1987).

96. Mertig, M., Thiele, U., Bradt, J., Klemm, D. & Pompe, W. Dewetting of thin collagenous precursor films. *Appl. Phys. Mater. Sci. Process.* **66**, S565–S568 (1998).

97. Scianna, M., Bell, C. G. & Preziosi, L. A review of mathematical models for the formation of vascular networks. *J. Theor. Biol.* **333**, 174–209 (2013).

98. Fornabaio, G. *et al.* Angiotropism and extravascular migratory metastasis in cutaneous and uveal melanoma progression in a zebrafish model. *Sci. Rep.* **8**, 10448 (2018).

99. Douezan, S. & Brochard-Wyart, F. Dewetting of cellular monolayers. *Eur. Phys. J. E Soft Matter* **35**, 34 (2012).

100. Douezan, S. *et al.* Spreading dynamics and wetting transition of cellular aggregates. *Proc. Natl. Acad. Sci.* **108**, 7315–7320 (2011).

101. Copenhagen, K., Alert, R., Wingreen, N. S. & Shaevitz, J. W. Topological defects promote layer formation in Myxococcus xanthus colonies. *Nat. Phys.* **17**, 211–215 (2021).

102. Guillamat, P., Blanch-Mercader, C., Pernollet, G., Kruse, K. & Roux, A. Integer topological defects organize stresses driving tissue morphogenesis. *Nat. Mater.* (2022) doi:10.1038/s41563-022-01194-5.

103. Fardin, M.-A. & Ladoux, B. Living proof of effective defects. *Nat. Phys.* **17**, 172–173 (2021).

104. Penrose, L. S. Dermatoglyphic Topology. *Nature* **205**, 544–546 (1965).

105. Thampi, S. P., Golestanian, R. & Yeomans, J. M. Instabilities and topological defects in active nematics. *EPL Europhys. Lett.* **105**, 18001 (2014).

106. Doostmohammadi, A., Ignés-Mullol, J., Yeomans, J. M. & Sagués, F. Active nematics. *Nat. Commun.* **9**, 3246 (2018).

107. Maroudas-Sacks, Y. *et al.* Topological defects in the nematic order of actin fibres as organization centres of Hydra morphogenesis. *Nat. Phys.* **17**, 251–259 (2021).

108. Duclos, G., Erlenkämper, C., Joanny, J.-F. & Silberzan, P. Topological defects in confined populations of spindle-shaped cells. *Nat. Phys.* **13**, 58–62 (2017).

109. Comelles, J. *et al.* Epithelial colonies in vitro elongate through collective effects. *eLife* **10**, e57730 (2021).

110. Vafa, F., Bowick, M. J., Shraiman, B. I. & Marchetti, M. C. Fluctuations can induce local nematic order and extensile stress in monolayers of motile cells. *Soft Matter* **17**, 3068–3073 (2021).

111. Okuda, S. & Fujimoto, K. A Mechanical Instability in Planar Epithelial Monolayers Leads to Cell Extrusion. *Biophys. J.* **118**, 2549–2560 (2020).

112. Saw, T. B. *et al.* Topological defects in epithelia govern cell death and extrusion. *Nature* **544**, 212–216 (2017).

113. Zhang, J., Yang, N., Kreeger, P. K. & Notbohm, J. Topological defects in the mesothelium suppress ovarian cancer cell clearance. *APL Bioeng.* **5**, 036103 (2021).

114. Suardet, L. *et al.* Responsiveness of three newly established human colorectal cancer cell lines to transforming growth factors beta 1 and beta 2. *Cancer Res.* **52**, 3705–3712 (1992).

115. Tom, B. H. *et al.* Human colonic adenocarcinoma cells: I. Establishment and description of a new line. *In Vitro* **12**, 180–191 (1976).

116. Morris, E. J. *et al.* Discovery of a Novel ERK Inhibitor with Activity in Models of Acquired Resistance to BRAF and MEK Inhibitors. *Cancer Discov.* **3**, 742–750 (2013).

117. Zeiser, R., Andrlová, H. & Meiss, F. Trametinib (GSK1120212). in *Small Molecules in Oncology* (ed. Martens, U. M.) vol. 211 91–100 (Springer International Publishing, 2018).

118. Serra-Picamal, X. *et al.* Mechanical waves during tissue expansion. *Nat. Phys.* **8**, 628–634 (2012).

119. Kandow, C. E., Georges, P. C., Janmey, P. A. & Beningo, K. A. Polyacrylamide Hydrogels for Cell Mechanics: Steps Toward Optimization and Alternative Uses. in *Methods in Cell Biology* vol. 83 29–46 (Elsevier, 2007).

120. Yeung, T. *et al.* Effects of substrate stiffness on cell morphology, cytoskeletal structure, and adhesion. *Cell Motil. Cytoskeleton* **60**, 24–34 (2005).

121. Comelles, J. *et al.* Microfabrication of poly(acrylamide) hydrogels with independently controlled topography and stiffness. *Biofabrication* **12**, 025023 (2020).

122. Serra-Picamal, X., Conte, V., Sunyer, R., Muñoz, J. J. & Trepat, X. Mapping forces and kinematics during collective cell migration. in *Methods in Cell Biology* vol. 125 309–330 (Elsevier, 2015).

123. Trepat, X. *et al.* Physical forces during collective cell migration. *Nat. Phys.* **5**, 426–430 (2009).

124. Thielicke, W. & Sonntag, R. Particle Image Velocimetry for MATLAB: Accuracy and enhanced algorithms in PIVlab. *J. Open Res. Softw.* **9**, 12 (2021).

125. Trainer, D. L. *et al.* Biological characterization and oncogene expression in human colorectal carcinoma cell lines. *Int. J. Cancer* **41**, 287–296 (1988).

126. Onochie, O. E., Zollinger, A., Rich, C. B., Smith, M. & Trinkaus-Randall, V. Epithelial cells exert differential traction stress in response to substrate stiffness. *Exp. Eye Res.* **181**, 25–37 (2019).

127. Saez, A. *et al.* Traction forces exerted by epithelial cell sheets. *J. Phys. Condens. Matter* **22**, 194119 (2010).

128. Rheinlaender, J., Wirbel, H. & Schäffer, T. E. Spatial correlation of cell stiffness and traction forces in cancer cells measured with combined SICM and TFM. *RSC Adv.* **11**, 13951–13956 (2021).

129. Blanch-Mercader, C., Guillamat, P., Roux, A. & Kruse, K. Integer topological defects of cell monolayers: Mechanics and flows. *Phys. Rev. E* **103**, 012405 (2021).

130. Tlili, S. *et al.* Migrating Epithelial Monolayer Flows Like a Maxwell Viscoelastic Liquid. *Phys. Rev. Lett.* **125**, 088102 (2020).

131. Mahmud, A. & Feely, J. Review: Arterial stiffness and the renin-angiotensin-aldosterone system. *J. Renin Angiotensin Aldosterone Syst.* **5**, 102–108 (2004).

132. Vennin, C. *et al.* Transient tissue priming via ROCK inhibition uncouples pancreatic cancer progression, sensitivity to chemotherapy, and metastasis. *Sci. Transl. Med.* **9**, eaai8504 (2017).

133. Ottaiano, A. *et al.* Study of Ras Mutations' Prognostic Value in Metastatic Colorectal Cancer: STORIA Analysis. *Cancers* **12**, 1919 (2020).

134. Bremnes, R. M. *et al.* The Role of Tumor Stroma in Cancer Progression and Prognosis: Emphasis on Carcinoma-Associated Fibroblasts and Non-small Cell Lung Cancer. *J. Thorac. Oncol.* **6**, 209–217 (2011).

135. Bonn, D., Eggers, J., Indekeu, J., Meunier, J. & Rolley, E. Wetting and spreading. *Rev. Mod. Phys.* **81**, 739–805 (2009).

136. de Gennes, P. G. Wetting: statics and dynamics. *Rev. Mod. Phys.* **57**, 827–863 (1985).

137. Deforet, M., Hakim, V., Yevick, H. G., Duclos, G. & Silberzan, P. Emergence of collective modes and tri-dimensional structures from epithelial confinement. *Nat. Commun.* **5**, 3747 (2014).

138. Paschos, K. A., Canovas, D. & Bird, N. C. The role of cell adhesion molecules in the progression of colorectal cancer and the development of liver metastasis. *Cell. Signal.* **21**, 665–674 (2009).

139. Clark, A. G. & Vignjevic, D. M. Modes of cancer cell invasion and the role of the microenvironment. *Curr. Opin. Cell Biol.* **36**, 13–22 (2015).

140. Paredes, J. *et al.* Epithelial E- and P-cadherins: Role and clinical significance in cancer. *Biochim. Biophys. Acta BBA - Rev. Cancer* **1826**, 297–311 (2012).

141. Lu, P., Weaver, V. M. & Werb, Z. The extracellular matrix: A dynamic niche in cancer progression. *J. Cell Biol.* **196**, 395–406 (2012).

# 8. Appendix

## 8.1 Supplementary figures and tables

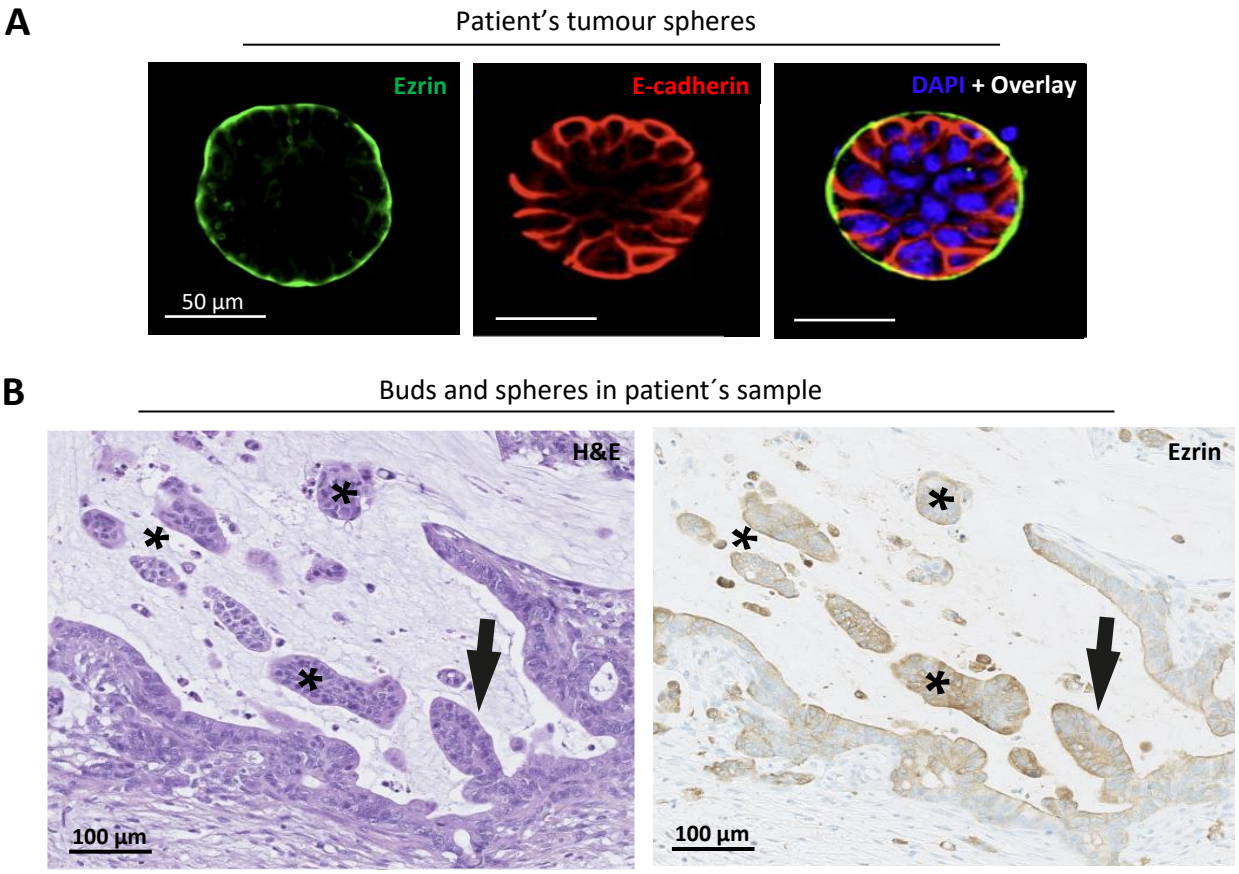


***Figure 8.1.1.*** *(A) Immunofluorescence staining of representative TSIPs from peritoneal effusions. Nuclei are labelled in blue, E-cadherin is labelled in red and Ezrin in green. Scale bars: 50 µm. (B) Histological section of CRC patient showing bulging structures (black arrow) and tumour spheres (black asterisks) in the colon. Samples were stained with Hematoxylin and Eosin (H&E) and for Ezrin.*

| TSIP (+) associated-tumour genetics | |
|---|---|
| Primary tumour stage T3 | 18% |
| Primary tumour stage T4 | 82% |
| KRAS Mutation | 62,50% |
| BRAF Mutation | 25% |
| WT | 12,50% |

***Table 8.1.1.*** *Table showing the genetic profile of human TSIPs-positive colorectal carcinomas. Table built using patients' data obtained at Gustave Roussy Hospital in Paris.*

| Cell line | CMS | KRAS | BRAF |
|---|---|---|---|
| LS513 | 3 | G12D | WT |

***Table 8.1.2.*** *Table showing the genetic profile of our colorectal cancer model. CMS: Consensus molecular subtype. G12D is the most prevalent and oncogenic KRAS mutant variant. KRAS residue Gly12 is substituted with an aspartic acid. Table built using ACCC information on LS513 cell line.*

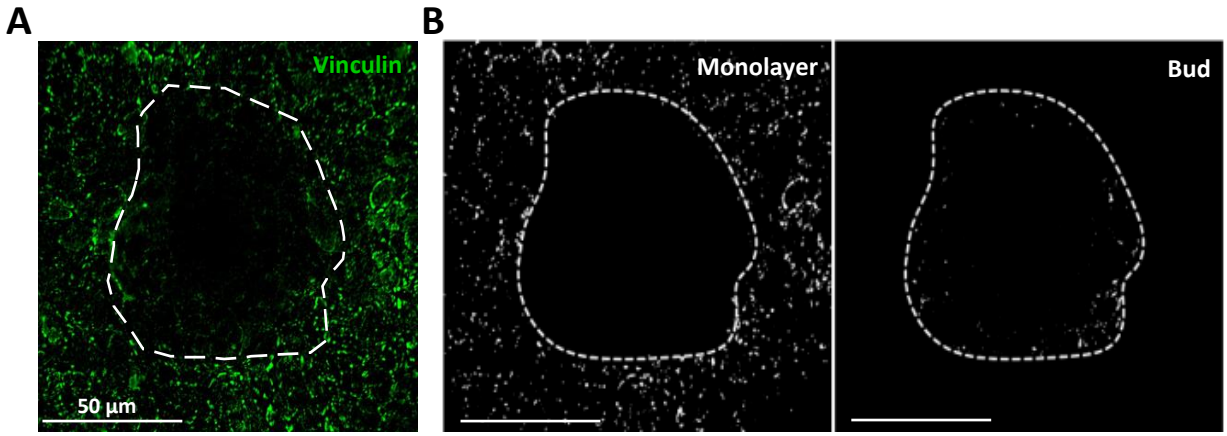


***Figure 8.1.2.*** *(A) Confocal microscopy image of representative max-projection of basal z-stacks, showing LS513 cells stained for Vinculin. The white dotted area frames a budding region. (B) Binary masks resulting from the pipeline explained in Methods section 3.7. and displaying focal adhesions in budding vs non-budding monolayer. The dotted lines delimit the budding area. Scale bars: 50 µm.*

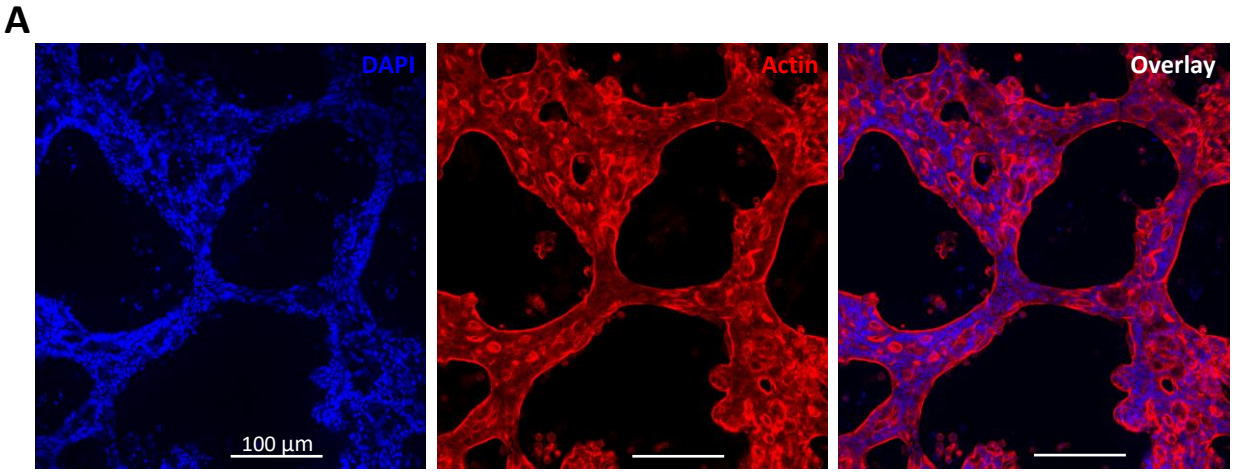


***Figure 8.1.3.*** *(A) Representative network-like structures formed by LS513 cells grown on 3 kPa gels for around two weeks. Scale bars: 100 µm. N= 2 experiments.*

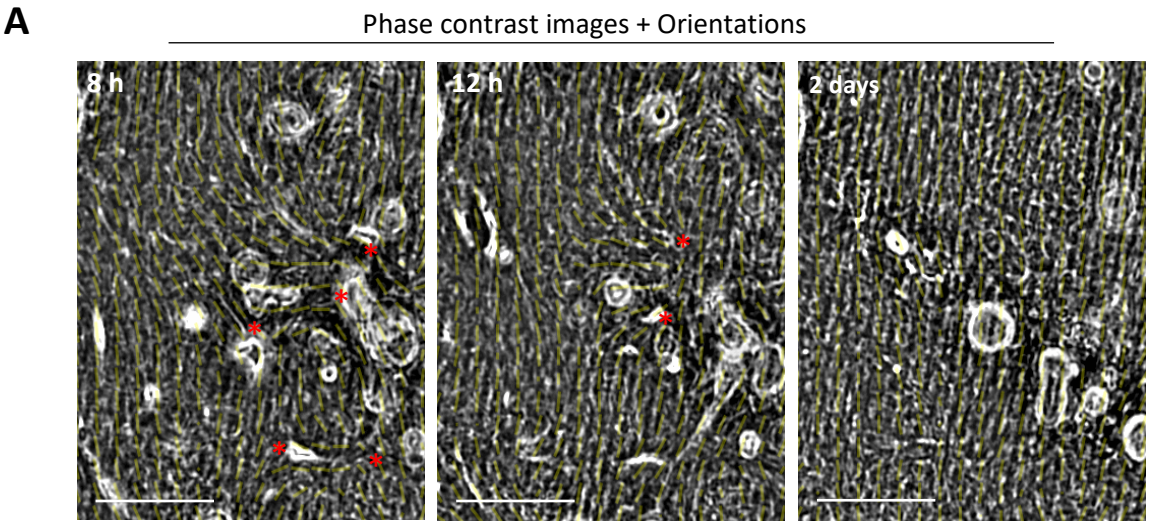


***Figure 8.1.4.*** *(A) Representative phase-contrast images and orientations (in yellow), showing progressive alignment of LS513 cells grown on 30 kPa grooved gels. Scale bars: 50 µm.*

## 8.2 Supplementary codes and macros

```
function [File] = cell_cropperANedit_GF2020_Monolayer(Settings,File);
% CELL_CROPPER crops all images i.e. gel fluorescence images (GFI),
% reference images (RI, after trypsinization) and phase contrast images (PC).

% Images are cropped so that the shift between the GFI and the corresponding
% RI is smaller than 0.5 pixels.

% Each GFI is cross-correlated with all RIs to determine the RI which focusing
% plane is closer to that of the GFI. Then the shift between GFI and RI is
% calculated and both images are cropped and stored in the folder CROPEDDATA.

% The program also allows to cross-correlate several ROIs of the RI and GFI
% to obtain a more accurate measurement of the shift and a better estimation
% of the optimal RI.
%
%   Xavier Trepat 05/02/2007
%   Raimon Sunyer 09/26/2006
%   Based on the code from Iva Marija Tolic-Norrelykke 'crop_onecell.m';
%   Agata Nyga 08/11/2018 - remove fixed beads
%   Giulia Fornabaio 22/07/2020- Added Buds and Actin
%
% Define the ROI. This contains the region with the cells of interest.

i1 = Settings.CenterRoiY - Settings.Size_ROIy/2+1;
i2 = Settings.CenterRoiY + Settings.Size_ROIy/2;
j1 = Settings.CenterRoiX - Settings.Size_ROIx/2+1;
j2 = Settings.CenterRoiX + Settings.Size_ROIx/2;
interv = Settings.Interval;

% Major loop that goes through each GFI of the experiment
for i=1:1:File.NFiles.Fluorescence;
    disp(['Processing ',File.Name(i).Fluorescence, ' of ',
num2str(File.NFiles.Fluorescence), ' images']);

    im2 = double(imread(File.Name(i).Fluorescence)); % Open the GFI
    k_min=1; k_max =  File.NFiles.Trypsin; % to correlate all RIs to find
the optimal one


    ti1 = Settings.BeadsROI.i1; % ti1, ti2, tj1 and tj2 define the ROI that
will be cross-correlated
    ti2 = Settings.BeadsROI.i2;
    tj1 = Settings.BeadsROI.j1;
    tj2 = Settings.BeadsROI.j2;
    for k = k_min:k_max,
        im1 = double(imread(File.Name(k).Trypsin));
        im1a = im1(ti1:ti2,tj1:tj2); % crop RI
        im2a = im2(ti1:ti2,tj1:tj2); % crop GFI
        [dumx, dumy, shx_temp(k), shy_temp(k), MaxCorr(k)] =
disp_on_blocks_fast( im1a, ... % reference image
            im2a, ... % measurement image
            size(im1a,1), ... % resolution of the PIV grid
            size(im1a,2), ... % resolution of the PIV grid
            0, ... % overlap between blocks
            0, ... % padding for the PIV, usually 0
```

```
            'cosn', ... % window for FFT calculation
            '2DCentroid', ... % method to compute max of cross-correlation
            0, ... % threshold of center of mass calculation
            3, ... % Size of the window
            9 ...
            ); % two second iteration
    end
    [OptimalTrypsinCorrelation, OptimalTrypsinIndex] = max(MaxCorr); % Find
the image with the largest correlation
    shx_subpix=shx_temp(OptimalTrypsinIndex); % find the shift for the best
trypsin image
    shy_subpix=shy_temp(OptimalTrypsinIndex);
    shx_subpix=median(shx_subpix(find(~isnan(shy_subpix)))); % compute the
median of all ROIs
    shy_subpix=median(shy_subpix(find(~isnan(shy_subpix))));
    shx=round(shx_subpix);
    shy=round(shy_subpix);
    OptimalTrypsinCorrelation=mean(OptimalTrypsinCorrelation); % compute
the mean correlation
    [x,n] = hist(OptimalTrypsinIndex,[min(OptimalTrypsinIndex)
:1:max(OptimalTrypsinIndex)]); [dum t] = max(x); % Optimal trypsin image
    OptimalTrypsinImage= n(t);

    File.Drift(i).shx = shx; % store the most relevant values in the
structure File
    File.Drift(i).shy = shy;
    File.Drift(i).shx_subpix = shx_subpix;
    File.Drift(i).shy_subpix = shy_subpix;
    File.Drift(i).OptimalTrypsinCorrelation = OptimalTrypsinCorrelation;
    File.Drift(i).OptimalTrypsinSmallBeads = OptimalTrypsinImage;
    File.Drift(i).shx_centroid = shx;
    File.Drift(i).shy_centroid = shy;
    File.Drift(i).shx_centroid_subpix = shx_subpix;
    File.Drift(i).shy_centroid_subpix = shy_subpix;
    File.Drift(i).pkh = OptimalTrypsinCorrelation;
    File.Drift(i).OptimalTrypsinImage =  OptimalTrypsinIndex;
    disp(['     ... current image displacement is
','(',num2str(File.Drift(i).shx_centroid),',',num2str(File.Drift(i).shy_cen
troid),') pixels... ', 'optimal trypsin image is ',
num2str(OptimalTrypsinIndex), ' and maximum correlation is ',
num2str(OptimalTrypsinCorrelation)]);

    %crop and save
    if
(File.Drift(i).OptimalTrypsinCorrelation>Settings.MinCorrelationTrheshold
&& File.Drift(i).pkh>Settings.MinCorrelationTrheshold), % if correlation is
smaller than this it means that something wrong happened to your image

        File.Mask(i).Crop=1; % This marks this file as good

        % crop the optimal trypsin image
        if(Settings.Do.SaveAllTrypsinInCropFolder)
            im1 =
double(imread(File.Name(File.Drift(i).OptimalTrypsinImage).Trypsin)); % the
optimal trypsin image
            im1b = im1(i1:i2,j1:j2);
            File.Name(i).OptimalTrypsin=[File.pathname 'Croppeddata',
'\crop','_', 'trypsin', '_', num2str(i),'.tif'];
```

```
imwrite(uint16(im1b),File.Name(i).OptimalTrypsin,'tif','compression','none'
);
        else % Save only the first image

im1=double(imread(File.Name(File.Drift(1).OptimalTrypsinImage).Trypsin)); %
the optimal trypsin image
            im1b = im1(i1:i2,j1:j2);
            File.Name(1).OptimalTrypsin=[File.pathname 'Croppeddata',
'\crop','_', 'trypsin', '_', num2str(i),'.tif'];

imwrite(uint16(im1b),File.Name(1).OptimalTrypsin,'tif','compression','none'
);
        end

        % crop the fluorescence image
        im2b = im2(max(1,i1+shy) : min(size(im2,1),i2+shy), max(1,j1+shx) :
min(size(im2,2),j2+shx));
        File.Name(i).CropFluorescence=[File.pathname 'Croppeddata',
'\crop','_', 'Fluorescence', '_', num2str(i),'.tif'];
        imwrite(uint16(im2b), File.Name(i).CropFluorescence,'tif',
'compression', 'none');

        % crop phase contrast image
        if exist(File.Name(i).PC)
            imPhase = double(imread(File.Name(i).PC));
            imPhase = imPhase(max(1,i1+shy) : min(size(imPhase,1),i2+shy),
max(1,j1+shx) : min(size(imPhase,2),j2+shx));
            File.Name(i).CropPC=[File.pathname 'Croppeddata', '\crop','_',
'PC', '_', num2str(i),'.tif'];
            imwrite(uint16(imPhase), File.Name(i).CropPC,'tif',
'compression', 'none');
        end

%         crop buds phase contrast image
         if exist(File.Name(i).Buds)
             imPhase = double(imread(File.Name(i).Buds));
             imPhase = imPhase(max(1,i1+shy) : min(size(imPhase,1),i2+shy),
max(1,j1+shx) : min(size(imPhase,2),j2+shx));
            File.Name(i).CropBuds=[File.pathname 'Croppeddata',
'\crop','_', 'Buds', '_', num2str(i),'.tif'];
            imwrite(uint16(imPhase), File.Name(i).CropBuds,'tif',
'compression', 'none');
         end
%
         % crop actin fluo image
         if exist(File.Name(i).Actin)
            imPhase = double(imread(File.Name(i).Actin));
            imPhase = imPhase(max(1,i1+shy) : min(size(imPhase,1),i2+shy),
max(1,j1+shx) : min(size(imPhase,2),j2+shx));
            File.Name(i).CropActin=[File.pathname 'Croppeddata',
'\crop','_', 'Actin', '_', num2str(i),'.tif'];
            imwrite(uint16(imPhase), File.Name(i).CropActin,'tif',
'compression', 'none');
        end
    else
        disp(' Correlation is too low. File discarded from further
analysis! ');
        File.Mask(i).Crop=0; % mark it as a wrong file and do not save it.
    end;
    save Settings Settings;
```

```
    save File File;
end %for i=1:File.NFiles.Fluorescence,

disp(' ');
disp('*** End image cropping ***');
```

***Code 8.2.1.*** *MATLAB code written to align and trim the phase contrast images and the fluorescent ones. Before being trimmed all the images are aligned to the corresponding reference images, which are obtained after trypsinization.*

```
input = "E:/Insert_name_InputFolder/";
output = "E:/Insert_name_OutputFolder/";
// set batch mode to run the orientation analysis on all the images
setBatchMode(true);
list = getFileList(input);
for (i = 1; i < Nfinal; i++){ //loop to analyse all the images in the exp

       // open the phase contrast (PC) images contained in the input folder
        open("E:/Insert_name_InputFolder/Croppeddata/crop_PC_"+i+".tif");
       // process the images for better visualizing cell borders
        run("Sharpen");
        run("Bandpass Filter...", "filter_large= ,filter_small=
,suppress=None ,tolerance= ,autoscale saturate");
        run("Sharpen");
        run("Sharpen");
        // save the processed images
        saveAs("Tiff",
"E:/Insert_name_OutputFolder/crop_PC_modified_"+i+".tif");
        // run the orientation analysis (change parameters according to
magnification used)
        run("OrientationJ Vector Field");
        // insert here the analysis parameters
        run("OrientationJ Vector Field", "tensor= ,gradient= ,radian=
,vectorgrid= ,vectorscale= ,vectortype= ,vectoroverlay=on ,vectortable=on
");
        // save the PC images + orientations as tif
        saveAs("Tiff",
"E:/Insert_name_OutputFolder/crop_PC_modified_vectors_"+i+".tif");
        close();
        selectWindow("OJ-Table-Vector-Field-");
        // save the analysis on orientation as csv
        saveAs("CSV", "E:/Insert_name_OutputFolder/OJ-Table-Vector-
Field_"+i+".csv");
        close("OJ-Table-Vector-Field_"+i+".csv");
}
setBatchMode(false);

///////sub-macro to save all the tif files as PNG
input = "E:/Insert_name_InputFolder/";
output = "E:/Insert_name_InputFolder/PNG_images/";
// set batch mode to save all the previous tif images as PNG
setBatchMode(true);
list = getFileList(input);
for (i = 1; i <251 ; i++){
        // open the phase contrast (PC) images + orientation vectors
contained in the input folder
```

```
open("E:/Insert_name_InputFolder/crop_PC_modified_vectors_"+i+".tif");
        // save the PC images + orientations as PNG
        saveAs("PNG",
"E:/Insert_name_InputFolder/PNG_images/crop_PC_modified_vectors_"+i+".png")
;
        close();
}
setBatchMode(false);
```

***Code 8.2.2.*** *ImageJ macro written to process the phase contrast images and analyse the orientation of LS513 cells (language used: IJ1, ImageJ Macro Language 1).*

```
function [File] = MaskingANindividual(Settings,File);


%%%to create mask of regions of interest%% %%Vito Conte, Agata Nyga%%%
%Create output folders
mkdir ./IndividualMasks/Masks/HighRes;%Create folder for high resolution
masks
mkdir ./IndividualMasks/Masks/LowRes;%Create folder for low resolution masks
mkdir ./IndividualMasks/Masks/RingMask; %Create folder for ring masks

path = File.pathname;
p=Settings.resolution;%size in image pixels of the Interrogation Window (ROI)
used in the cross-correlation analysis
q=Settings.Overlap;
h=round(p*q/2); %no-data frame: margin of the phase-contrast and fluorescent
images (in image pixels)
mps=(1-q)*p; %macropixel's size in terms of traction microscopy's resolution

hs1=Settings.Size_ROIx-mps;
hs2=Settings.Size_ROIy-mps;
interv = Settings.Interval;
%CROSS-CHECK high-res sizes and trimming
if hs1~=Settings.Size_ROIx-2*h||hs2~=Settings.Size_ROIy-2*h %check if high
resolution images have been properly trimmed of the no-data frame
    error('phase-contrast and fluo images have not been properly trimmed of
the no-data frame');
end

%%%%%%%%%%%%%%%%%%%%%%%%%%%%%%%%%%%%%%%%%%%%%%%%%%%%%%%%%%%%%%%%%%%%%%%%%%%%
%SETTING MASK
%%%%%%%%%%%%%%%%%%%%%%%%%%%%%%%%%%%%%%%%%%%%%%%%%%%%%%%%%%%%%%%%%%%%%%%%%%%%

for t=1:interv:File.NFiles.PC; %loop over time to create mask for each time
point
    imphase=imread([path    'Croppeddata',    '\crop','_',    'PC',    '_',
num2str(t),'.tif']);% load phase contrast images
    BW=roipoly(imphase);%HIGH RESOLUTION MASK - N.B. it includes the no-data
zone
    close

    hrmsk=BW(h+1:end-1,h+1:end-h);%get    rid    of    the    no-data    zone
msk=imresize(hrmsk,[File.TractionSize(1).ifinal,File.TractionSize(t).jfinal
]);%downscale highresmask to the resolution of mechanical quantification
    msk=logical(msk);% transform in logical values
    rmsk=RingMask(msk);
```

```
    dlmwrite([path
'IndividualMasks\Masks\HighRes\','HighResMask',num2str(t),'.dat'],hrmsk,'ne
wline','pc','delimiter',' ','precision','%.0f');
    dlmwrite([path
'IndividualMasks\Masks\LowRes\','LowResMask',num2str(t),'.dat'],msk,'newlin
e','pc','delimiter',' ','precision','%.0f');
    dlmwrite([path
'IndividualMasks\Masks\RingMask\','RingMask',num2str(t),'.dat'],rmsk,'newli
ne','pc','delimiter',' ','precision','%.0f');

end
```

***Code 8.2.3.*** *MATLAB code written to create high resolution, low resolution, and ring masks.*

## Summary in English

Living tissues are active materials with the ability to undergo drastic shape and dimension transitions. If properly controlled, these morphological changes allow various physiological phenomena such as embryonic development, regeneration, and wound healing. However, when regulation fails, aberrant morphological transitions could cause developmental defects and tumour formation. Among others, some examples of malignant morphological transformations are monolayer dewetting and cancer budding.

The general goal of this thesis was to investigate how supracellular cell and tissue mechanics contribute to colorectal cancer epithelia budding and dewetting. In the first part of the study, we studied the role played by mechanical and topological cues in the formation of budding structures in LS513 monolayers, while in the second part we focused on the mechanical characterization of 2D/3D malignant retraction (dewetting) of confined LS174 in epithelia.

Using a combination between cellular biology techniques and biophysical methods, we showed that budding in LS513 epithelia is a multi-step morphological phenomenon fostered by stroma stiffening. Moreover, we revealed that budding occurs in monolayer regions displaying higher traction forces and higher vorticity.

We also demonstrated that bud formation in LS513 epithelia is characterised by the emergence of a cloud-like pattern of +1/2 topological defects at the level of the monolayer. This pattern of defects is visible in the epithelium from the early stages of the process, until the formation of a mature bulging structure.

Finally, we showed that KRAS oncogene-mediated MAPK activation is a necessary condition for budding in LS513 epithelia; indeed, the use of MAPK pathway inhibitors dramatically hinders the formation of buds. Interestingly, we also discovered that MAPK inhibition causes dramatic topological defects reduction.

In the second part of the thesis, we showed that dewetting in confined LS174T epithelia occurs in a non-symmetric fashion and is accompanied by various morphological changes at the level of the monolayer. The asymmetry of this process is reflected by the differential traction profiles exerted during dewetting by the retracting edge, if compared to the non-retracting side of the pattern.

We also demonstrated that dewetted LS174T patterns present different normal and magnitude traction profiles, if compared to non-dewetted islands.
Finally, we showed that, in LS174T confined patterns, substrate adhesion is a key parameter in determining transition from cellular spreading to dewetting.

Overall, our results demonstrate the pivotal role played by mechanical and topological cues in the formation of budding structures in LS513 monolayers and in 2D/3D malignant retraction (dewetting) of confined LS174 epithelia.

## Resumen en castellano

Los tejidos vivos son materiales activos con la capacidad de sufrir drásticas transiciones de forma y dimensión. Si se controlan adecuadamente, estos cambios morfológicos permiten diversos fenómenos fisiológicos como el desarrollo embrionario, la regeneración y la cicatrización de heridas. Sin embargo, cuando la regulación falla, las transiciones morfológicas aberrantes podrían causar defectos de desarrollo y formación de tumores. Entre otros, algunos ejemplos de transformaciones morfológicas malignas son el monolayer *dewetting* y el *budding* (gemación) del cáncer.

El objetivo general de esta tesis fue investigar cómo la mecánica supracelular de células y tejidos contribuye al *budding* y al *dewetting* del epitelio del cáncer colorrectal. En la primera parte del estudio, estudiamos el papel desempeñado por las señales mecánicas y topológicas en la formación de *buds* en monocapas LS513, mientras que en la segunda parte nos centramos en la caracterización mecánica de la retracción maligna 2D/3D (*dewetting*) de epitelios LS174 confinados.

Usando una combinación entre técnicas de biología celular y métodos biofísicos, mostramos que la gemación en el epitelio LS513 es un fenómeno morfológico de varios pasos fomentado por el endurecimiento (*stiffening*) del estroma. Además, revelamos que la gemación ocurre en regiones monocapa que muestran mayores fuerzas de tracción y mayor vorticidad.

También demostramos que la formación de *buds* en el epitelio LS513 se caracteriza por la aparición de un patrón similar a una nube de +1/2 defectos topológicos a nivel de la monocapa. Este patrón de defectos es visible en el epitelio desde las primeras etapas del proceso, hasta la formación de una estructura 3D madura.

Finalmente, demostramos que la activación de MAPK mediada por el oncogén KRAS es una condición necesaria para la gemación en el epitelio LS513; de hecho, el uso de inhibidores de la vía MAPK dificulta dramáticamente la formación de *buds*. Curiosamente, también descubrimos que la inhibición de MAPK causa una reducción dramática de los defectos topológicos.

En la segunda parte de la tesis, mostramos que el dewetting en epitelios confinados de LS174T ocurre de manera no simétrica y se acompaña de diversos cambios morfológicos a nivel de la monocapa. La asimetría de este proceso se refleja en los perfiles de tracción diferencial

ejercidos durante el *dewetting* por el borde retráctil, si se compara con el lado no retráctil de la monocapa.

También demostramos que los patrones de LS174T que han hecho *dewetting* presentan diferentes perfiles de tracción normales y de magnitud, si se comparan con las islas que no se han retirado.

Finalmente, demostramos que, en los patrones confinados LS174T, la adhesión del sustrato es un parámetro clave para determinar la transición del *spreading* celular al *dewetting*.

En general, nuestros resultados demuestran el papel fundamental desempeñado por las señales mecánicas y topológicas en la formación de *buds* en monocapas LS513 y en la retracción maligna 2D/3D (*dewetting*) de epitelios confinados de LS174.

Tesi Doctoral

# Biomechanics of the progression of colorectal carcinomas

Giulia Fornabaio

UNIVERSITAT DE BARCELONA